UNIVERSITÁ DEGLI STUDI DI PADOVA

Sede Amministrativa: Universitá degli Studi di Padova
Dipartimento di Fisica

SCUOLA DI DOTTORATO DI RICERCA IN FISICA
XX CICLO

Experimental Measurements of Soft X-Ray Emissivity Distribution and Electron Temperature Profile in Reversed Field Pinch Plasmas

Direttore della scuola: Ch.mo Prof. Attilio Stella
Supervisori: Ch.mo Prof. Piero Martin
Dr. Paolo Franz

Dottoranda: Federica Bonomo

31 gennaio 2008

« I was just guessing at numbers and figures
Pulling the puzzles apart.
Questions of science, science and progress
Don’t speak as loud as my heart. »

(“The scientist” - Coldplay)

a Luca...

Contents

Abstract

This thesis reports the work performed during the three years of my Ph.D. course at the Physics Department of the University of Padova. Most of my research activity has been performed in Consorzio RFX[1] (Padova) where the RFX experiment is located. RFX (Reversed Field eXperiment) is the largest toroidal device to study magnetically confined plasmas of thermonuclear interest in the so-called reversed field pinch (RFP) configuration.

The RFP, together with the tokamak and the stellarator, is one of the main configurations used to confine plasmas in toroidal devices with the purpose of studying controlled thermonuclear fusion as an energy source. The energy production by fusion in magnetically confined plasmas is an ambitious and important goal, which could contribute to solve the problem of a sustainable energy source for mankind. To be an efficient energy source, a sufficiently dense and hot plasma must be confined for a sufficiently long time. In order to fulfill this goal, energy and particle losses need to be understood and eventually controlled.

In RFPs, transport is at present dominated by magnetic chaos, even if, under some circumstances that will be presented in this thesis, it can decrease to lower levels. The magnetic boundary quality, i.e. the deviations from axis symmetry and the inhomogeneity of the passive structures, has strong influences on the magnetic activity and eventually on transport. The RFX experiment has been modified in order to investigate in a controlled way these issues.

In order to obtain information on the effects of the boundary on the plasma core, my research activity has been focused on performing spatially resolved measurements of the plasma emissivity in the soft x-ray (SXR) energy range. In particular, I was involved in experimental and laboratory activities, in diagnostic operation and optimization, along with the design and realization of a new SXR diagnostic. I also analyzed SXR data, allowing a characterization of the plasma column and of the MHD plasma activity. The tomographic algorithms applied to the SXR signals

[1] http://www.igi.cnr.it

allow for the reconstruction of the SXR emissivity distribution [2], which reflects the plasma magnetic topology. Such information can be completed by the estimation of the electron temperature (T_e) profile, calculated with the two-foil technique [3].

My research activity on the RFX-mod experiment can be summarized as follows:
SXR tomography. My personal contribution mostly concerns the optimization of the SXR tomographic diagnostic, both experimentally and in the data analysis, in order to obtain reconstructions of the SXR plasma emissivity distribution. I collaborated with the team that designed and realized several improvements of the SXR diagnostic. At first, a new set of curved Be filters replaced the old flat ones, in order to remove a systematic error that significantly degraded the reconstruction capability of the tomographic diagnostic. Moreover, I was involved in the realization of a new UHV pumping system. All these diagnostic development activities occurred in parallel with data analysis aimed at characterizing SXR emissivities in different RFX-mod operational regimes. In particular, I performed detailed studies on SXR emissivity during QSH states.
SXR multichord diagnostic and on-axis spectrometer. I was involved in tests and installation of a new SXR multichord diagnostic, for the estimate of the electron temperature profiles in the low-field side of the RFX-mod plasma. This diagnostic allows for a high bandwidth spatially resolved measurement of the electron temperature, significantly improving the diagnostic that only measures at the plasma center. This older diagnostic was in any case useful to characterize the SXR spectrum and give information to optimize filter thicknesses for electron temperature estimate with the two-foil technique. I collaborated to the optimization of its electronic chain and of the geometry of the detection system.
New SXR manipulator. Part of my activity has been dedicated to the study and realization of a new SXR instrument that will significantly enhance the present tomographic system. This new manipulator will in fact allow for detecting the SXR emissivity in different energy ranges: that permits to increase the spatial resolution of the SXR tomography and to the T_e profile estimate with the two-foil technique.

During my Ph.D., I was also involved in the collaboration between RFX and the University of Wisconsin, Madison, where the Madison Symmetric Torus (MST) experiment is located. My activity has been part of the collaboration between RFP groups for experimental studies on MHD processes and was focused on operating the SXR tomographic diagnostic installed in MST and realized by the RFX group. Data analysis was aimed at obtaining 2D profiles of the plasma electron temperature. My personal contribution has concerned the optimization of the geometry of the detection system and the electronic system, as well as the diagnostic operation. Moreover, I was directly involved in dedicated experimental campaigns and in the

[2] P. Franz, L. Marrelli, A. Murari, G. Spizzo, and P. Martin, Nucl. Fusion **41**,695 (2001).
[3] P. Martin, A. Murari, and L. Marrelli, Plasma Phys. Contr. Fusion **38**, 1023 (1996).

data analysis.

This thesis describes the main results obtained by analyzing SXR data. In order to help the reader to better understand the context, the first three chapters give a brief overview of introduction information on the RFP and of SXR plasma emissivity. In particular, in *Chapter 1* the importance of SXR measurements in plasma physics for fusion research has been highlighted, focusing the attention on the x-ray radiation, how it has been exploited and developed historically from its discovery, and how it has been adopted in fusion plasmas at the end of the XX century.

Chapter 2 briefly describes the magnetically confined plasma configuration for fusion research. Attention is focused on RFPs, together with a concise summary of the RFP basic plasma physics. Two RFP experiments are introduced, with their main mechanical characteristics and operational regimes, the RFX-mod experiment and the MST device.

In *Chapter 3* the dependence of SXR plasma radiation on several main plasma parameters is reported. This strong dependence makes the SXR measurements necessary for understanding plasma physics. These motivations and the experimental diagnostics for this kind of measurements on the two RFP experiments are explained in detail. SXR emissivity distribution is tightly linked to magnetic field plasma topology, as well as the presence and location of impurities inside the plasma. In addition, the electron temperature can be derived from SXR measurements, providing information on plasma performances in different operational regimes.

The main results obtained with the SXR diagnostics in RFX-mod are reported in *Chapter 4*. The high spatial resolution and temporal accuracy of the SXR tomography allowed for identifying and characterizing the SXR localized and more emissive structures arising in the plasma core, in different operational regimes. These SXR structures have been identified with magnetic islands; attention has been focused on the structure emerging during the Oscillating Poloidal Current Drive (OPCD) operation. In particular, their temperature estimation and temporal evolution have been investigated and compared to those obtained with other diagnostics.

The high flexibility of the MST experiment and of its SXR tomography allowed for exploiting different measurement configurations: various energy range spectra have been investigated and the results are reported in *Chapter 5*. SXR measurements in different energy ranges allowed for determining also 2D maps of the plasma electron temperature T_e with the two-foil technique or by means of a SXR emissivity model.

Conclusions and results for both the RFP experiments are summarized in *Chap-*

ter 6. The importance of SXR studies for understanding RFP plasma physics is herein pointed out, in particular because they have allowed for obtaining reliable measurements on the features of QSH regimes.

All the results explained in the previous chapters have been the motivations for designing and realizing a new SXR diagnostic to be implemented into the SXR tomography in the RFX-mod device. The design of this new diagnostic is reported in *Chapter 7*. This new instrument will upgrade the present SXR tomography, along with the possibility of simultaneously measuring different SXR energy ranges. The new manipulator will increase the tomographic diagnostic spatial resolution, but it will also permit to investigate the plasma emissivity in different energy spectra, allowing for the estimation of the plasma electron temperature profile.

Prefazione

In questa tesi vengono riassunte le attivitá scientifiche svolte nei tre anni della Scuola di Dottorato in Fisica, presso il Dipartimento di Fisica dell'Universitá degli Studi di Padova. La mia attivitá si é svolta principalmente presso il Consorzio RFX[4] (Padova), dove ha sede il piú grande esperimento toroidale per lo studio dei plasmi confinati magneticamente nella cosiddetta configurazione "reversed field pinch" (RFP).

La configurazione RFP, insieme con i tokamak e gli stellarator, risulta una delle maggiori configurazioni per confinare i plasmi in esperimenti toroidali, con lo scopo di studiare la fusione termonucleare come sorgente di energia. La produzione di energia attraverso la fusione in plasmi confinati magneticamente é un ambizioso e importante obiettivo, che potrebbe contribuire a risolvere il probema di una sorgente sostenibile di energia per tutta l'umanitá. Per essere una sorgente di energia efficiente, un plasma sufficientemente denso e caldo deve essere confinato per un tempo sufficientemente lungo. A questo scopo, la perdita di energia e di particelle deve esser capita ed, eventualmente, controllata.

Negli esperimenti di tipo RFP, il trasporto é al momento dominato dal caos magnetico, anche se in particolari circostanze che verranno presentate in questa tesi, puó diminuire a piú bassi valori. La qualitá delle condizioni al contorno magnetiche, quali le deviazioni dalla simmetria dell'asse magnetico e le disomogeneitá della struttura passiva, influenza grandemente l'attivitá magnetica ed eventualmente il trasporto.

Al fine di ottenere informazioni sugli effetti delle condizioni al contorno sul centro del plasma, la mia attivitá di ricerca é stata focalizzata sulle misure ad alta risoluzione spaziale dell'emissivitá del plasma nell'intervallo energetico dei raggi X soffici (SXR). In particolare, sono stata coinvolta in esperimenti ed attivitá di laboratorio, nell'operazione e ottimizzazione delle diagnostiche SXR, oltre che nella progettazione e realizzazione di un nuovo strumento SXR. Mi sono inoltre dedicata

[4] http://www.igi.cnr.it

all'analisi dei dati raccolti con questi strumenti, che mi hanno consentito di caratterizzare la colonna di plasma, e di fornire informazioni sulla sua attivitá MHD. Gli algoritmi tomografici applicati ai segnali SXR permettono la ricostruzione della distribuzione di emissivitá[5] che riflette la topologia magnetica del plasma stesso. Questa informazione puó essere completata da informazioni sui profili della temperatura elettronica (T_e) di plasma, calcolati con la tecnica del doppio-filtro[6].

La mia attivitá di ricerca svolta sull'esperimento RFX-mod puó essere riassunta come segue:
Tomografia SXR. Il mio personale contributo riguarda essenzialmente l'ottimizzazione della diagnostica tomografica SXR, sia dal punto di vista sperimentale sia degli algoritmi di analisi dati, al fine di ottenere delle ricostruzioni dell'emissivitá SXR del plasma. Ho collaborato con il gruppo che ha disegnato e realizzato alcuni miglioramenti della diagnostica SXR. In primo luogo, nuovi supporti curvi per i filtri di Berillio hanno sostituito i precedenti, che erano piatti, al fine di rimuovere degli errori sistematici che degradavano significativamente le ricostruzioni tomografiche. Inoltre, ho preso parte alla realizzazione di un nuovo impianto UHV per la tomografia SXR. Tutte queste esperienze sperimentali si sono ben integrate con l'attivitá di analisi dati, al fine di caratterizzare l'emissivitá SXR in diversi regimi operativi di RFX-mod. In particolare, mi sono dedicata allo studio dell'emissivitá SXR durante gli stati QSH.
Diagnostica SXR multicorde e spettrometro multifiltro. Mi sono occupata dei test e dell'installazione della nuova diagnostica SXR multicorde per la stima dei profili di temperatura elettronica (T_e) nella regione "low-field side" del plasma. Questo strumento consente di ottenere misure temporalmente e spazialmente risolte della temperatura elettronica, migliorando significativamente la diagnostica che misura la temperatura del plasma solo in asse. Questa vecchia diagnostica é stata molto utile in ogni caso per caratterizzare lo spettro SXR e fornire informazioni per ottimizzare gli spessori dei filtri di Berillio per la stima della temperatura elettronica con la tecnica del doppio-filtro. Ho collaborato all'ottimizzazione della catena elettronica e della geometria del sistema di rivelazione.
Nuovo manipolatore SXR. Parte della mia attivitá é stata dedicata allo studio e alla realizzazione di un nuovo strumento di rivelazione SXR, che significativamente migliorerà l'attuale diagnostica tomografica. Questo nuovo manipolatore consentirá infatti una misura simultanea dell'emissivitá di plasma in diversi intervalli energetici: questo permette di aumentare la risoluzione spaziale della tomografia e di fornire una misura del profilo di T_e con la tecnica del doppio-filtro.

Durante il corso di dottorato, ho preso parte alla collaborazione tra il gruppo di RFX e l'Universitá del Wisconsin, Madison (USA), dove ha sede l'esperimento Madison Symmetric Torus (MST). La mia attivitá di ricerca rientra in un piú am-

[5] P. Franz, L. Marrelli, A. Murari, G. Spizzo, and P. Martin, Nucl. Fusion **41**,695 (2001).
[6] P. Martin, A. Murari, and L. Marrelli, Plasma Phys. Contr. Fusion **38**, 1023 (1996).

pio progetto tra i gruppi RFP sugli studi sperimentali dei processi MHD, ed é stata incentrata sulla diagnostica tomografica SXR installata nell'esperimento MST e realizzata dal gruppo RFX. Le analisi dei dati sono state mirate ad ottenere profili 2D della temperatura elettronica del plasma. Il mio contributo personale ha riguardato l'ottimizzazione della geometria del sistema di rivelazione e della catena elettronica; ho preso parte alle campagne sperimentali, alcune delle quali dedicate alle misure SXR.

Questa tesi descrive i migliori risultati ottenuti analizzando misure SXR. Al fine di aiutare il lettore a meglio comprendere il contesto, i primi tre capitoli forniscono una breve descrizione introduttiva sugli esperimenti di tipo RFP e sulla emissivitá del plasma. In particolare, nel *Capitolo 1* viene sottolineata l'importanza delle misure SXR nei plasmi da fusione, focalizzando l'attenzione sulla radiazione X e su come sia stata scoperta storicamente, utilizzata e sfruttata nel corso della storia, e adottata alla fine del XX secolo per i plasmi di interesse termonucleare.

Il *Capitolo 2* descrive brevemente la configurazione per il confinamento magnetico dei plasmi da fusione. L'attenzione é stata focalizzata sulla configurazione RFP, insieme ad una breve descrizione della fisica dei plasmi. I due esperimenti RFP trattati nella tesi sono qui introdotti e descritti nelle loro caratteristiche meccaniche e funzionali, nonché dei diversi regimi operazionali: l'esperimento RFX-mod e l'esperimento MST.

Nel *Capitolo 3* viene descritta la dipendenza della radiazione SXR da alcuni importanti parametri di plasma. Tale forte dipendenza rende le misure SXR necessarie per la conoscenza della fisica del plasma. Queste motivazioni e le diagnostiche sperimentali per questa tipologia di misure sono presentate in entrambi gli esperimenti, RFX-mod e MST. La distribuzione spaziale di emissivitá é strettamente collegata alla configurazione topologica delle linee di campo magnetico, nonché alla presenza di impurezze nel plasma. In aggiunta, é possibile ottenere informazioni sulla temperatura elettronica del plasma, fornendo ulteriori elementi sulle prestazioni del plasma in diversi regimi operativi.

I principali risultati ottenuti con le diagnostiche SXR nell'esperimento RFX-mod sono riportate nel *Capitolo 4*. L'elevata risoluzione spaziale e temporale della tomografia SXR ha consentito di identificare e caratterizzare strutture SXR localizzate che emergono nel centro del plasma, in diversi regimi operativi. Queste strutture SXR sono state identificate con le isole magnetiche; l'attenzione é stata focalizzata in particolare sulle strutture che emergono durante l'applicazione dell'Oscillating Poloidal Current Drive (OPCD). In particolare, sono state studiate la temperatura e la sua evoluzione temporale, e comparate a quelle ottenute con altre diagnostiche.

L'elevata flessibilitá dell'esperimento MST e della sua diagnostica tomografica SXR ha consentito di esplorare diverse configurazioni di misura: diversi intervalli energetici sono stati studiati e i risultati sono riportati nel *Capitolo 5*. Misure SXR nei diversi intervalli energetici hanno consentito inoltre di determinare la mappa 2D della temperatura elettronica con la tecnica del doppio-filtro, e con un modello SXR. Ció ha confermato le elevate prestazioni del plasma durante l'applicazione del Pulse Poloidal Current Drive (PPCD) in MST.

Le conclusioni e i risultati per entrambi gli esperimenti considerati nella tesi sono infine riassunti nel *Capitolo 6*. L'importanza degli studi SXR per conoscere la fisica dei plasmi di tipo RFP viene sottolineata, in particolare queste misure consentono di ottenere informazioni affidabili sulle caratteristiche degli stati QSH.

Tutti i risultati e le considerazioni precedenti hanno infine motivato la progettazione e realizzazione di una nuova diagnostica SXR che affiancherá la tomografia nell'esperimento RFX-mod. Il progetto viene descritto nel *Capitolo 7*. Questo nuovo strumento migliorerá le misure tomografiche, permettendo anche la misura simultanea in diversi intervalli energetici SXR. Tale strumento aumenterá la risoluzione spaziale della diagnostica tomografica, permettendo anche la stima del profilo di temperatura elettronica.

CHAPTER 1

X-ray radiation: from discovery to plasma physics application

1.1 X-rays: the mistake that changed the world

X-rays are a form of electromagnetic radiation with a wavelength in the range from 0.01 to 10 nanometers. They were discovered by mistake in a small German laboratory but soon they were used all over the world with an important impact on humanity. Many commercial entertainment ventures were launched that capitalized on the initial craze. From these ventures grew legitimate medical applications and practices, along with a new x-ray industry. Hospitals and private clinics became the center for one of the first functional, widespread medical advancements in years. Their unknown effects were revealed only years later, freezing the initial infatuation: the early scientific pioneers were disfigured, cancer-ridden, and in constant pain. But explanations were not yet available, until the discovery of radium answered the riddle of the x-ray: radioactivity was found to be the dangerous side-effect causing the many ailments.

X-ray discovery affected not only the medical industry: its influence was felt throughout society, culture, and the military. In fact, it presented a new potential danger to conservative Victorian society because it exposed women's bodies and created a possible outlet for females to break from constraining societal norms; the discovery allowed women to enter the workforce by becoming x-ray technicians. The x-ray was embraced also in literature (literary science fiction developed out with many titles centering around the concept of x-rays and invisibility), art (artists such as Frida Kahlo, Pablo Picasso, and Francis Picabia incorporated many x-ray influenced elements into their paintings), and the emerging television and motion

picture industries. In military field, they were adopted by the American government for a pre-induction health record of all recruits to the world war I, so they could not be forced to pay for the care of veterans who inaccurately claimed they had contracted tuberculosis while in service. Moreover, once the world war II began, the USA were prepared with a large stock of new Picker Company designed portable equipment.

Today, the x-ray has helped to create entire specialized fields within the medical industry. Almost everyone has been touched by the x-rays in some way; whether it is the middle-aged woman having her yearly mammogram or the experienced business man having his luggage inspected before his flight. The frequency of today's scientific developments along with the increasingly pervasive world of computer technology creates an optimistic, almost limitless future for the use of the mistakenly discovered ray.

1.1.1 Motivations for practical diagnosis

Before the advent of the x-ray, medical diagnosis was very primitive. No scientific methods of investigation for any pain or broken bones were available, except for the sense of touch of the physician. Difficult diagnosis and unappropriate treatments were very common, and lots of lives were lost. When President James Garfield was shot in 1881, his doctor promptly probed the entrance wound with his index finger and estimated that the bullet was lodged somewhere. After being transported back to the White House, at least six doctors crowded around his bed attempting to locate the bullet to no avail. Garfield died eighty days after his attack simply because the bullet could not be located using appropriate technology [1].

The medical motivation for a more practical diagnosis tool was not the only predecessor of the x-ray. The Victorian world of the late 19th century was obsessed with photography following recent technological advancements which allowed its introduction to the public at large. The world was visually prepared for the x-ray revolution that would soon overtake it; all that was left was the scientific advancement that would make it possible.

1.1.2 The antecedents to x-ray discovery

The most crucial antecedent to the x-ray was the Crookes tube. In the late 1800s, the English physicist Sir William Crookes created a vacuum tube for his own studies of gas. The glass tube contained negative and positive electrodes and an induction coil, through which high-voltage electrical currents could be passed [2, 3]. A battery setup was also required to produce the electrical charge. Crookes primarily worked with the conductivity of gases, confined into the glass tube. Following this creation, German scientists Heinrich Hertz and Philipp Lenard discovered the cathode ray while experimenting with the Crookes tube [4]. Lenard also redesigned the tube with a thin aluminum window that the cathode rays could pass through to the outside. During one of his experiments, the fluorescence of a dissi-

pated ray created a few pieces of barium platinocyanide compound soaked paper on a nearby paper to glow. Lenard had unknowingly discovered the first evidence of the existence of x-rays, but failed to investigate the strange phenomenon further, thus allowing Professor Wilhelm Conrad Röntgen to recreate the experiment a few months later.

1.1.3 X-ray discovery and investigation

Wilhelm Conrad Röntgen was not the typical physicist: he never received his high school diploma and lived most of his life in seclusion. On November 8th, 1895, the fifty-year old Röntgen was working late in his lab investigating the properties of cathode rays. Of the many tubes he was using, he was primarily concerned with his colleague Philipp Lenard's variation of the Crookes tube [1]. He decided to repeat some of Lenard's and Hertz's experiments hypothesizing that the rays had always penetrated the glass tube, but were previously undetected. In order to test this, he covered the tube with black cardboard in a darkened room and supplied the electric current [4]. He had forgotten to put a screen directly in front of the tube. Nonetheless, a greenish yellow glow appeared on a cardboard screen that was lying on a chair several feet away from the tube. Röntgen was surprised to see that not only the screen was glowing far away from the tube, but glowing in the shape of the letter "A", which a student had written on the cardboard in liquid barium platinocyanide [1].

Amazed, Röntgen placed the screen several tenths of centimeters in front of the tube and tested it again. Once again, the screen began to glow. He then placed a deck of cards and a large book between the tube and the screen. He discovered the ray could penetrate through these materials. A small wooden box containing metal weights was also used but he found that the ray also did not go through the entire box; it only cast the shadow of the weights upon the screen [2]. For the next month Röntgen dedicated every free moment to investigating the phenomenon. On reflection, he stated, *«I didn't think, I investigated.»* [1]. In December, another huge discovery was made; while holding up a lead pipe to the ray, the bones of his fingers were shadowed on the screen [2]. Unable to believe his eyes, Röntgen decided to show his wife what had occupied his time, resulting in the x-ray image of her hand (see Fig.1.1). She exclaimed, *«Oh my God...It makes me somehow feel that I'm looking at my own death!»* [2].

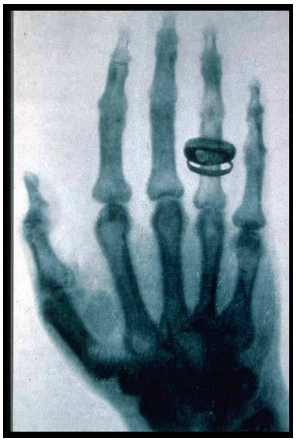

Figure 1.1: *Röntgen's wife hand.*

During this entire period of his experiments, Röntgen worked in secrecy because he realized that every other physicist had Crookes tubes and could discover

the phenomenon for themselves [2]. The professor wanted to publish his results in the Physical-Medical Society of Wuerzburg's December journal and worked relentlessly on his preliminary report, which was finished on December. He submitted his paper only a week before publication but the publishers agreed that it needed to be published immediately [2]. A copy of his findings, *On a New Kind of Rays*, along with copies of the x-ray of his wife's hand, were also sent to six of the most important physicists in Europe on New Year's Day. In this paper, Röntgen referring to the rays called them ***x-rays*** because their source was unknown at that time. However, the name stuck and even today we refer to his mystery rays as x-rays [1]. In few days, the story was reported by the *German Die Presse* and within days Röntgen was an instant celebrity.

1.2 X-rays and first applications

The most obvious use of x-rays was in the world of medicine: they were used to locate kidney stones, reset dislocations, and to check the size and condition of the heart and lungs [3]. The legal system also quickly incorporated the discovery; less than a year after the x-ray's introduction, a judge allowed x-ray evidence into court proceedings [4]. The most surprising use of the x-ray was in the realm of the spiritual; because of the spiritualist movement sweeping America in the late 19th century, the x-ray was considered to be a possible link to the fourth dimension and the *"other side"*. Advertisers of the newly created x-ray industry were unsure of who their audience was so they emphasized the simplicity and quick results their machines afforded. How-to manuals were printed for the amateur and slogans such as *«So easy a child can do it»* created a mass market for the adoption of the x-ray. However, the so-called miracle x-ray would soon show its darker side to the world.

After the public's initial infatuation with the x-ray died down, the medical world began to carefully examine the potential uses of this invention. The availability of the equipment was widespread, thus making such investigations possible. In the meantime, many physicians were referring their patients to physics labs to get x-rays before every medical procedure. This overload of patients helped create new home and office practices to help ease the burden of the science labs. Unfortunately, these new x-ray centers were hot, crowded with wires and machines, and dangerous. It was soon realized that hospitals needed to take control of the x-ray industry: Boston Hospital was one of the first to create an x-ray room.

As the number of clinics and hospital departments grew, doctors and technicians were discovering the curative effects of x-rays upon people with cancer, tuberculosis, and skin disorders. In Chicago, a widely publicized case of an electrotherapist successfully irradiating a woman with breast cancer led to the widespread of *x-ray therapy* for all kinds of disorders. X-rays were used to supposedly cure everything from ringworm to wrinkles. By 1900, it was clear that the future of the x-ray belonged to the medical world. Adoption was speeded along by the immediate availability of the apparatus and the immense public and professional

fascination with the discovery.

1.3 X-rays and Tomography

Since their discovery, x-rays have been exploited in medical fields to take pictures by impressing upon plates the internal components of human beings. But in this way only the projection of the absorption coefficients of the examined body was obtained, and no complete reconstructions of the object itself were achieved. From the 20's of the last century, improvement in the realization of the plates and the techniques allowed for obtaining clearer images in radiography, but the correct interpretation of radiographs was let on the art of the radiographer: more quantitative information based on real measurements were needed.

A fundamental input for the development of more quantitative measurements was given by A.M. Cormack and G.H. Hounsfield, awarded of the Nobel Prize in medicine in 1979. They noteworthy contributed to the development and realization of the first ***tomographic*** algorithms and diagnostic for medical application. The patient was positioned between an x-ray (or gamma ray) source and detectors, rotating rigidly together, so that the beam intersected the patient along different lines of observation. All the data were therefore stored and processed so that an image of the internal parts of the patient was obtained by means of mathematical algorithms. The first application in the '60s was called *Computerized Tomography* (CT) or *Computerized Assisted Tomography* (CAT). Computerized refers to the fact it is based on numerical calculation. This application has been extensively exploited for diagnosis not only in medicine, but also in many other different fields of application. In fact, the problem of the reconstruction of the internal characteristics of an object is essentially a mathematical problem of inversion, commonly present in the physics world. In the following, a brief description of the development of the tomographic technique and of the problems intrinsic to this method are reported. More accurate details can be found in [5, 6].

1.3.1 X-rays: line integrals and the problem of inversion

At the mid of the XX century, the exponential attenuation of a parallel beam of x-ray passing through homogeneous materials was known and used for long time in radiology. But the problem of quantitative determination of the variable absorption coefficient in inhomogeneous media (like the human being actually is) had received little or no attention at that time. A.M. Cormack was the first to investigate this problem, when he was a lecturer in Physics at the University of Cape Town [5, 6, 7]. He brought the problem back to a mathematical problem: let D be a finite two-dimensional domain in which there is absorbing material characterized by a linear absorption coefficient g, varying from point to point in D, while it is zero outside D. If a parallel and indefinitely thin beam of monoenergetic x-rays (or gamma rays) traverses D along a straight line L (called *line of sight*) as displayed in Fig.1.2, and

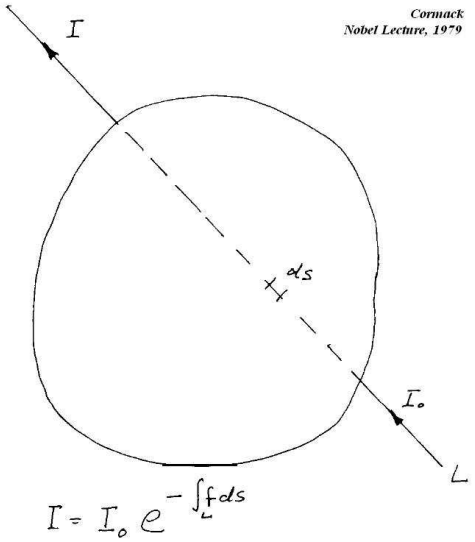

Figure 1.2: *Schematic view of the absorption coefficient problem (A.M. Cormack, Nobel Lecture 1979 [7]).*

the intensity of the incident beam is I_0, the intensity of the emerging beam I from D is given by:

$$I = I_0 \exp\left[-\int_L g(s)\, ds\right] \tag{1.1}$$

where the L denotes the line of propagation of the x-rays, and s is a measure of distance along L. If the experimental measurement is $f_L = \ln(I_0/I)$, then

$$f_L = \int_L g(s)\, \mathrm{ds}. \tag{1.2}$$

The experimental signal is therefore the integral of the local contributions of the absorption parameters along the line of sight. The problem in Eq.(1.2), which is a conversion from the 2-dimensional function g (in the plane of the measurements) to the set of its line integrals f_L intersecting the domain D, is the *Radon Transform*. Thus, the problem of image reconstruction is reduced to the determination of the inverse of the Radon Transform. The transform owes its name to the German mathematician Radon who first proved that a unique solution exists. The proof was not constructive, so there was no algorithm available to obtain the solution. Moreover, the limited sampling seemed also to be difficult to overcome. Years later, in its original paper [5], Cormack illustrated the difficulties with the following example. One could think that a suitable way of finding g (as suggested by taking two radiographs in directions at right angles to each other) would be of measuring f_L along two sets of parallel lines at right angles to each other. But this is not the case. Let us consider the domain D as a square, divided into n^2 equal

smaller squares, and consider the directions L along which the line integrals are calculated, be parallel to the side of the square. If in each small square g assumes the average value inside that square, the line integral as calculated in Eq.(1.2) may be approximated by the sum of the average values of g in the rows and columns of smaller squares. This leads to $2n$ values of f_L, and Eq.(1.2) is reduced to a set of $2n$ equations in the n^2 average values of g in the smaller squares. Moreover, the sum of n values of f_L parallel to a side must be equal to the sum of the n values parallel to the other side, so that only $2n-1$ equations are independent. The problem is therefore indeterminate, except for the trivial case $n = 1$. If $n = 2$, there are three independent equations in four unknowns. In this case, for example, if $g = -1$ in the diagonally opposite squares of the matrix D and $g = 1$ in the other two squares, the line integrals are equal to zero even in case of a swap of the g values. Extending these considerations at $n > 2$, a solution can be found if the f_L along all the lines intersecting D are considered, and then an approximate solution may be found by considering only a finite number of f_L.

1.3.2 Cormack: a constructive solution

The paradox suggests that, no matter how many independent measurements performed, the absorption function g is always undetermined. Cormack derived a solution that constructively quantifies the indetermination: the higher the number of measurements, the lower the indetermination. This raises the issue of the link between the spatial resolution and the number of lines of sight.

However not all the lines of sight are suitable! If they intersect those parts of an object the radiographer is not interested in, the obtained data are affected by those useless information. For example, if you are interested to find the absorption coefficient in an annulus, you need data only from lines not intersecting the hole in the annulus (the so-called *Hole Theorem*) [7, 8], otherwise you will have only redundant information about the annulus but not new ones. So, lines of sight intersecting those regions outside the part of interested have to be limited to avoid useless data. However this is unavoidable, and those pointless information, entering the measurements, turn out to be badly amplified. Cormack needed a solution containing the Hole theorem for which the external "noise" did not propagate into the measurements of the internal part of the object. In this way, lot of advantages were achieved. First of all, the dose administered to a patient by not passing x-rays through a region of no interest (i.e. "the hole") could be reduced. Second, the theorem could be used to avoid regions in which sharp changes in absorption coefficient occur. These sharp changes necessarily produce overshoots which blur the final image. For example, in an extreme case consider a patient who by accident or by some medical procedure has in his body a piece of metal: it could distorts a CT scan of a plane containing the metal beyond recognition. Less extremely, an interface between bone and soft tissue introduces overshoots which distort the image of the soft tissue: the Hole Theorem could be used to avoid the bone and the distortion, too.

By taking into account these considerations, Cormack proposed a solution based on the decomposition of the g and f_L functions over Fourier series and radial harmonics, founding the 1-1 correspondence between the harmonics of the f_L measurements and those of the g function. A limited number of the lines of sight relapses in a limited number of the f_L harmonics available, and therefore to the harmonics of the g function which can be reconstructed: only a truncated approximation on the first harmonics of g is obtainable. Details on the Cormack algorithms can be found in Apx.A.

1.3.3 Tomography for medical application

In medicine, where it was first applied and developed, tomography was widely exploited and had the larger diffusion, in treatment and diagnosis of cancer [9, 10]. The patient is positioned between an x-ray (or gamma ray or proton) source and detectors (it is referred to as *tomography in absorption*), so that the beam intersects the patient along a large number of different lines of observation and the detectors reveal the fraction of the beam not absorbed by the human body.

Two were the possible geometrical setting of the lines of sight developed and realized originally for medical application [7]. One of them was realized by Hounsfield in the first CT commercial system. It was based on a set of parallel lines of sight, equally spaced, requiring a unique source of radiation and only one detector, rigidly rotating around the body itself [11]. The drawback of such arrangement is that the time required to perform the measurements is long.

A different configuration is based on a source moving around the body, while a fixed array of detectors are capturing the radiation passing throughout the body. The movement of the source with respect to the body sets a large number of measurements of the radiation absorption coefficient in a large variety of different lines of observation. Thus a high spatial resolution is obtained with the same time resolution as the single detector arrangement. The relative movement between source and detectors requires for a fast response of the detectors to the intensity variation of the radiation impinging them.

But the number of measurements is anyway very important, because it determines the spatial accuracy of the reconstruction itself. A very large number of them intersecting the body in different directions are needed for a faithful reconstruction. The required spatial resolution is in fact of about 1mm: that needs for 2000-3000 lines of sight. The temporal resolution of the scan is not an issue, since the objects of interest (bones, lags, etc.) are not moving. Only exceptions are for the heart or the lungs, where the temporal resolution required is of about one second.

1.4 X-ray applications in plasma physics for fusion research

Due to its non-invasive nature, tomography has been used outside the medical field. A lot of applications can be found in geology, seismology, or in studying the atmosphere or ionosphere and in astrophysics [12]. In all these cases, the cardinal point remains the solution of the Eq.(1.2).

Among its many different applications, tomography found a prolific field in plasma physics for fusion devices. *Plasma* is a state of matter made up of a quasi-neutral ensemble of ions and electrons [13]. In the fusion research framework, isotopes of hydrogen are ionized inside vacuum chambers (vessels), in order to exploit the reaction of fusion between two light nuclei together into a new heavier one, releasing reaction products. This is a widespread phenomenon in nature: fusion reactions provide a huge source of energy to stars and other astrophysical settings. In fusion plasmas, the light nuclei can fuse together only if they are brought sufficiently close together for the short-range attractive nuclear force to overcome by quantum tunneling the Coulomb repulsion among them. This is possible if the two reactants collide with high enough kinetic energy. For a significant fraction of fusion reactions to occur, matter has thus to be brought to sufficiently high density ($\approx 10^{20}\mathrm{m}^{-3}$) and temperature ($\approx$ 20keV) for a sufficiently long time. Being composed of charge particles, the thermonuclear plasmas are confined inside vessels by means of appropriate magnetic fields (see Ch.2).

Tomographic techniques are used to reconstruct the radiation spontaneously emitted by the plasma. Plasma behaves in fact as a radiation source, mainly emitting in different ranges of wavelength, from visible light up to x-rays. In particular, plasma does not absorb the emitted x-ray radiation, so that tomography allows for the imaging of the plasma emissivity distribution (the emitted power per unit volume). In this thesis, only plasma radiation in the soft x-ray (SXR) range will be considered, with wavelength between 0.1 and 10nm (energies of 10eV-20keV).

1.4.1 Plasma information from SXR measurements

SXR emissivity depends on important plasma parameters, such as the electron temperature and density, and impurities inside the plasma. Therefore maps of SXR emission allow for investigating the shape of the plasma column with high resolution.

Magnetic flux surfaces can be in fact identified with X iso-emissive surfaces (see for details §3.1): therefore the SXR plasma emissivity distribution over a cross-section (poloidal) of the toroidal vessel allows a visualization of the internal structure of the plasma. Information both of the equilibrium (i.e. displacement of the plasma column) and perturbations (i.e. development of localized structures with helical topology) can be obtained with magnetic measurements performed outside the plasma.

The SXR range of the plasma emitted radiation is selected by appropriate foils

(usually Beryllium foils), acting as energy selectors, in relation to their thickness. An adequate choice in the filter thickness allows for reducing or completely avoiding radiation contribution due to plasma impurities (line radiation or recombination step), contaminating the SXR measurements. Usually, the thicker the Be filters are, the better it is: impurity contribution to SXR radiation is in this case reduced and only bremsstrahlung radiation of free electrons moving in the electric field generated by ions is detected. Emissivity studies in different SXR energy ranges can be easily performed by using different thicknesses in the Be filters, and that can be used even to understand indirectly the presence of impurities and their radial location in the plasma column, in absence of specialized diagnostic tools (see Ch.5).

SXR plasma radiation is detected, line-integrated measurements f_L (called *brightness*) are processed and, after performing the reconstruction (see §3.3.1 and Apx.A for details), transformed in images. Though Cormack solution was developed for medical tomography, it was never applied to medicine. The large number of experimental measurements f_L in medicine requires a numerical solution. In the case of thermonuclear plasmas, the SXR emissivity maps can be usually represented with a limited number of angular harmonics. Therefore, a truncated version of the analytical solution proposed by Cormack can be directly applied.

A further important information which can be derived from SXR measurements is the value of the electron temperature (T_e). The ratio of two SXR brightness using different Be foil thickness but looking at the same plasma region is a strong function of T_e provided that the emission does not include line radiation or recombination steps. For details on this technique, see §3.4. Actually, in plasma physics for fusion research there are various diagnostics for T_e estimation. The Thomson Scattering (TS) [14] allows for determining T_e profiles: this diagnostic can have a high spatial resolution, but on the contrary the temporal accuracy is quite low (for examples, in RFX-mod, the TS diagnostic time resolution is linked to the repetition rate - 25Hz - of the Ruby laser, while the spatial resolution is of about 0.7cm). The ECE diagnostic [14] is very powerful in spatial and temporal resolution, but cannot be applied to the RFP because of the weak and rapidly varying toroidal field. This motivated the development of a T_e diagnostic exploiting the two-filter technique and tomographic algorithms: the so-called “two-color” tomography, that will be described in Ch.5.

1.4.2 First SXR tomography diagnostics in plasma physics

Prior to 1974, instabilities in high temperature fusion plasmas were detected solely with arrays of Mirnov coils located outside plasma; no information on the internal structure of the magnetic perturbations was therefore available. In 1974, a breakthrough was made by Von Goeler, Stodiek and Sauthoff [15], who installed a collimated surface barrier diode (SBD) on the ST tokamak (*tokamak* is a toroidal magnetic configuration for plasma confinement) to look at the central soft x-ray emission, revolutionizing the study of magnetic instabilities. SXR oscillations were correlated to magnetic instabilities, indicating that the magnetic activity was

occurring also in the plasma core. Within a couple of years, an array of these kind of detectors became a common fusion diagnostic for studying these phenomena in magnetically confined plasmas. An example of magnetic activity measured on ORMAK in the mid of 1970's is shown in Fig.1.3.

With a non-circular symmetric source and only a single array of detectors, the amount of information that can be obtained on local emission is quite limited. In an effort to determine the detailed structure of the magnetic perturbations, but lacking multiple arrays, many researchers took advantage of the apparent rotation of these perturbations to generate 2-dimensional images [16, 17, 18, 19]. However, this emissivity modeling is practical only if the rotation is rigid, which rules out plasmas with large displacements inside the vessel or with non-circular cross-sections. In addition, this technique is not valid if the emissivity changes during a rotation period. In addition, some of the most interesting magnetic instabilities occur on short timescale, so that a more powerful way of determining the 2D x-ray emissivity was necessary.

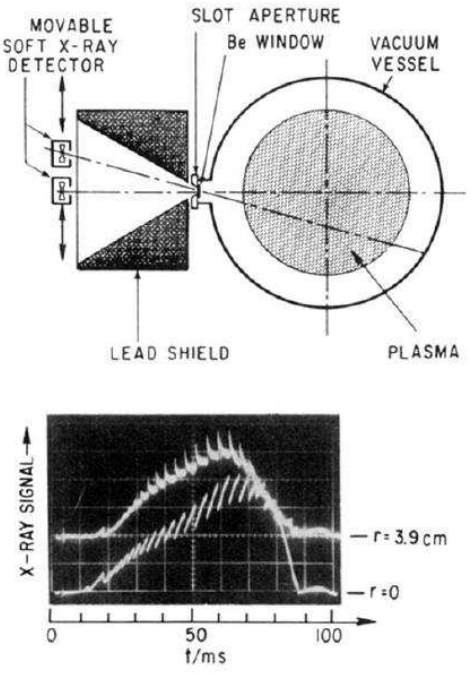

Figure 1.3: *Experimental arrangements of x-ray detectors. The x-ray traces exhibit internal disruptions. [15].*

During 1970s, while x-ray arrays were beginning to proliferate on tokamaks and other magnetic confinement fusion devices, the CT-scanner based on computerized tomographic reconstruction of x-ray images was becoming commercially available. The 1mm resolution achieved with CT using several hundred thousand chord measurements, with a time resolution of few seconds, was out of question for fusion device. However, several people investigated on the possibility to adapt tomographic algorithms to plasma devices [20, 21].

In the rotation modeling, the authors utilized Cormack inversion algorithms, rather than the more commonly used finite element methods; these algorithms happen to be particularly well-suited to application in tokamak x-ray imaging.

At the beginning of 1982, R. Granetz began searching for alternative detectors [22]. On Alcator C tokamak [23], new diodes (solid states diodes, sensitive to the light, with p-n junction, PIN) were used to measure visible emission from the pla-

sma: they were small and commercially available at low cost. These detectors were designed for measuring visible light, not SXR, but direct experiments showed that x-ray sensitivity and time resolution were comparable to the older SBD detectors. Given the low cost and the small sizes, it was possible to design a tomographic diagnostic with a relatively high number of channels. PIN diodes are now routinely used in SXR tomographic diagnostics in fusion devices.

1.4.3 Tomography and RFPs

In 1996 a SXR tomographic system was installed in a RFP (Reversed Field Pinch) experiment for the first time [24]. RFP devices are magnetic configuration experiments for plasma confinement, alternative to the tokamak (for details, see §2.3). As reported in the name itself, in the RFP the toroidal component of the magnetic field is reversed at the edge with respect to the plasma core. This magnetic configuration is characterized by a magnetic field with poloidal and toroidal components of comparable magnitude, mainly generated by currents within the plasma itself. This configuration is prone to the presence of a large number of magnetic instabilities which can grow in the plasma core and produce magnetic islands. In correspondence to these islands, SXR more emissive localized regions are identified. Imaging of these SXR structures was allowed by the application of the Fourier-Bessel expansion of the Cormack solution, as proposed by Nagayama [25]. The algorithm gives a good image reconstruction with few harmonics. If the amplitude of the many magnetic instabilities is approximatively the same (the so-called Multiple Helicity state, MH), the reconstructed SXR emissivity is symmetric, as displayed in Fig.1.4(a); in presence of an instability with an amplitude dominating the other ones, a magnetic island is present and an asymmetric emis-

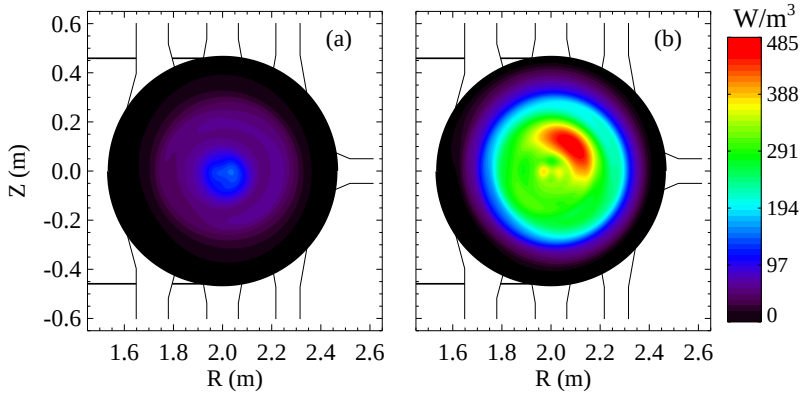

Figure 1.4: *Contour plot of the reconstructed SXR emissivity for (a) a standard multiple helicity (MH) discharge, and (b) for a quasi-single helicity (QSH) plasma in the RFX device; the color bar is in* W/m^3.

sivity profile with a localized more emissive region is detected (this state is called Quasi Single Helicity, QSH; see. Fig.1.4(b)). For details on MH and QSH states, see §.2.3.3. In the currently operating RFP experiments, the time scale of these instabilities is of the order of few ms. This sets a requirement on the bandwidth of the measurements up to several hundreds of kHz.

1.5 Thesis outline

This thesis focuses on the main results obtained by SXR measurements in the RFP RFX-mod and MST devices.

In *Chapter 2*, a brief description of a magnetically confined plasma for fusion research is reported. Attention is focused on the RFP magnetic configuration, together with a concise summary of the RFP basic plasma physics. Two RFP experiments are introduced, with their main mechanical characteristics and operational regimes: the RFX-mod experiment (§2.4.1) and the MST device (§2.4.2).

The dependence of SXR plasma radiation on plasma parameters together with the diagnostic implications are explained in detailed in *Chapter 3*.

In RFX-mod, the high spatial resolution and temporal accuracy of the SXR tomography allowed for identifying and characterizing the shape and temporal evolution of SXR localized and more emissive structures arising in the plasma core, in different operational schemes. In *Chapter 4*, the identification of these SXR structures with magnetic and thermal islands will be reported, in particular during the Oscillating Poloidal Current Drive (OPCD), which is a particular operation in which current is externally driven by an oscillating toroidal magnetic field. In particular, the T_e estimations obtained with SXR measurements are compared to independent diagnostics.

The high flexibility of the MST experiment and of its SXR tomography diagnostic allowed for exploiting different measurement configurations: various energy range spectra have been investigated and reported in *Chapter 5*. The interpretation of the experiments was performed by simulating the measurements with a SXR emissivity model, described in Apx.C. SXR measurements in different energy ranges has allowed for determining also the plasma electron temperature T_e with the two-foil technique. That permitted to confirm the high plasma performances of the Pulse Poloidal Current Drive (PPCD) operations in this device.

Conclusions and results for both the RFP experiments are summarized in *Chapter 6*. The importance of SXR studies for understanding RFP plasma physics is here pointed out, in particular because they have allowed for obtaining reliable measurements on the features of QSH regimes.

All the results explained in the thesis have been the motivations for designing and realizing a new SXR diagnostic that will upgrade the RFX-mod SXR tomography capability. The design of this new diagnostic is reported on *Chapter 7*. This new instrument not only will increase the spatial resolution, but it will allow also a simultaneous determination of the electron temperature profile.

CHAPTER 2

Magnetically confined fusion plasmas

2.1 Fusion: a possible solution to the energetic problem

The research of a clean and safe energy source is a worldwide problem affecting the entire humanity. This research is linked to the more worrying question of limited energy resources in a more and more energy demanding world. Among the various possibilities for power production, thermonuclear fusion seems to be the most promising solution, since it is CO_2-free and resources are potentially inexhaustible. In recent years, important breakthroughs in fusion plasma physics and technologies allowed for the design of the large International Thermonuclear Experimental Reactor (ITER), whose construction is about to start [26, 27] at the time of working this thesis. ITER will answer to many scientific and technological issues regarding the future fusion reactor.

In nuclear fusion, two light nuclei fuse into a heavier one, releasing energy in the form of kinetic energy of the reaction products. This phenomenon is common in nature (for example, in the stars) and has been investigated by scientists in the second half of the 20th century in order to realize controlled fusion reactions on earth for peaceful purposes. Two light nuclei fuse only if they get close enough for the short-range attractive nuclear force to overcome by quantum tunneling the Coulomb repulsion. This is achieved if the two reactants collide with high enough kinetic energy; a significant number of fusion reactions therefore occurs if matter is brought to sufficiently high density and temperature for a sufficiently long time. In this condition, matter is in the so-called ***plasma*** state, which is a quasi-neutral ensemble of ions and electrons [13].

Promising methods to realize fusion conditions in laboratory are the magnetic and inertial confinement (the latter topic is not matter of interest of this thesis). In magnetic confinement experiments [28], magnetic fields allow for confining matter in plasma state: in fact, charged particles perform a Larmor motion along the field lines, and therefore motion in the direction perpendicular to magnetic field is limited to the Larmor radius $\rho = mv_{\perp}/EeB$. This allows particles to be confined for a sufficient time to be heated and achieve the critical condition for the fusion reaction.

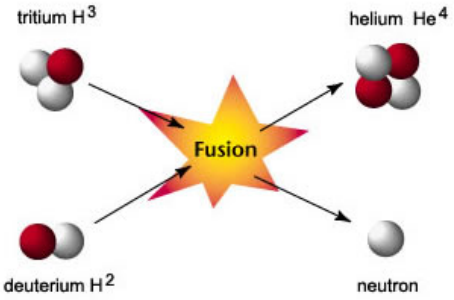

Figure 2.1: *Fusion reaction cartoon.*

Many fusion reactions can occur; the easiest to realize involves Deuterium (D) and Tritium (T) (see Fig. 2.1):

$$ {}^{2}_{1}D + {}^{3}_{1}T \longrightarrow {}^{4}_{2}He(3.56\text{MeV}) + {}^{1}_{0}n(14.03\text{MeV}). \tag{2.1} $$

For this reaction the cross-section peaks at the relatively low ion temperature of $\sim$ 100keV. Deuterium (D) resources are practically endless on earth (about 2mg of D are contained in 50 liters of sea water). Tritium (T) is radioactive, with a 12.3 year life time, but it can be produced in a fusion device by exposing a Lithium mantle to fusion neutrons. Lithium resources are practically endless too, since they can be derived from earth rocks.

In a fusion reactor, the energy produced by fusion reactions must exceed the energy required for creating and sustaining the plasma. If n is the plasma density, T its temperature and τ_E the energy confinement time, the *Lawson's criterion* [29] for the sustainment of a plasma fusion reaction leads to the following condition for the *triple product*:

$$ nT\tau_E \geq 3 \cdot 10^{21} \text{m}^{-3} s\ keV. \tag{2.2} $$

The density and temperature values achievable in laboratory experiments are of the order of $n \approx 10^{20}\text{m}^{-3}$ and $T \approx 20$keV, requiring an energy confinement time $\tau_E \gtrsim 1$s.

2.2 Magnetic confined fusion device

A magnetic confinement fusion device exploits the charged particle Larmor motion along the magnetic field: the field lines must therefore close on themselves to allow for good confinement. The simplest close configuration is a torus (see Fig.2.2). In fact the highest confinement time has been obtained in a toroidal device.

Simple considerations on particle orbit drifts in a toroidal field show that magnetic field lines cannot be simple circles around the torus, but need to be helical. In other words, the confining field must have both a toroidal and a poloidal component. The poloidal component is generated by an externally driven toroidal current I while the toroidal one is produced by currents flowing in external windings. The toroidal field can be increased or decreased according to the magnetic response of the plasma. The pitch of the magnetic field lines is tightly linked to the *safety factor* q, which describes quantitatively the stability boundaries of the machine, and is defined, in cylindrical approximation, as a function of radius as follows:

$$q(r) = \frac{r\, B_\phi(r)}{R_0\, B_\theta(r)}, \qquad (2.3)$$

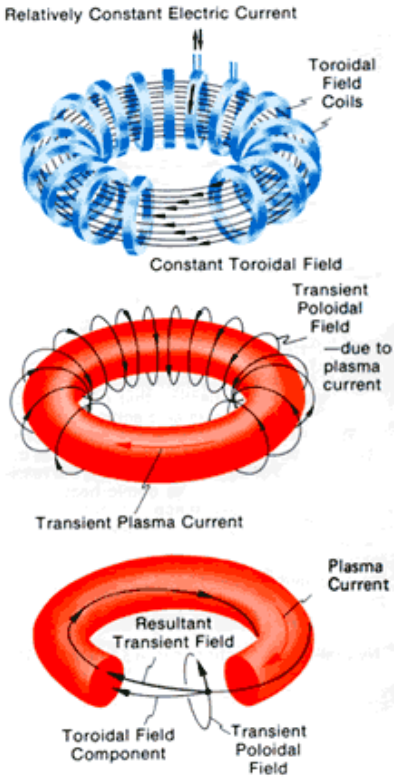

Figure 2.2: *Toroidal magnetic confinement for fusion device: scheme of the magnetic field lines.*

where r is the radial coordinate; θ and ϕ are the poloidal and toroidal angles respectively; R_0 represents the major radius of the torus (while a usually indicates the minor radius).

There are three types of toroidal devices for magnetic confinement, based on different q profiles: the Tokamak, the Stellarator and the Reversed Field Pinch (RFP). The latter is the one studied in this thesis, and will be described in more detail in §2.3.

2.2.1 MHD equilibrium and instabilities in toroidal plasmas

Depending on the spatial and time scale of interest, the plasma behavior can be described by different models. The MHD model [13, 28, 30] considers the plasma as an incompressible fluid under the action of electromagnetic forces. MHD equations result from the coupling of Navier-Stokes and Maxwell equations. They can be derived from first-principle single particle motion in the fluid limit [31]. In stationary conditions, the MHD equations are quite simple, giving a single vector equation as follows:

$$\nabla p = \mathbf{j} \times \mathbf{B}\,. \qquad (2.4)$$

Eq.(2.4) describes the balance between the confining magnetic forces and the thermal expansion of the plasma (being ∇p the gradient pressure, **j** the plasma current density and **B** the magnetic field).

Like any natural system, plasma is subject to perturbations of the equilibrium expressed in Eq.(2.4). In a MHD description, these perturbations can affect quantities like density, fluid velocity or magnetic field. If these perturbations grow in time, the plasma is defined *"unstable"*. Unstable perturbations, or instabilities [32], often called *modes*, are very important in determining the dynamics of many natural and laboratory plasmas; in fusion devices their presence can deeply affect the confinement properties of the device, and even induce fast and potentially dangerous terminations of the discharge called "disruptions". In general, an important task in fusion plasmas is therefore to determine the stability properties of the configuration. An equilibrium is defined *"stable"* if any perturbation does not grow in time, but it is either suppressed or kept to a constant value (the so-called "saturated" state).

Magnetic perturbations can also be considered as waves with wave vector **k** $= (r, \theta, \phi)$. Any perturbation of the toroidal equilibrium can be expressed in terms of Fourier components in the poloidal and toroidal angles. The poloidal (m) and toroidal (n) wavenumbers can be introduced:

$$\mathbf{B} = \mathrm{B}_0 + \mathbf{b} = \mathrm{B}_0 + \sum_{j=r,\theta,\phi} \sum_{m,n} b^j_{m,n} \, \exp\left(i(m\theta + n\phi + \phi_{m,n})\right) \, e_j \qquad (2.5)$$

where B_0 represents the equilibrium magnetic field and **b** the perturbation. It can be shown that the wave vector of the most unstable perturbation is aligned to the magnetic field $\mathbf{k}\cdot\mathbf{B} = 0$; this translates in a resonant condition for the safety vector:

$$q(r_{res}) = \frac{r_{res}}{R_0} \frac{B_\phi(r_{res})}{B_\theta(r_{res})} = -\frac{m}{n}. \qquad (2.6)$$

with r_{res} the radial positions (called *resonant surfaces*) where q assumes rational values.

On fast time scales, when the plasma resistivity can be neglected, MHD equilibrium simplifies (**ideal** MHD) and magnetic energy is conserved exactly. The stability of an equilibrium is determined by analyzing how the potential energy of the system δW changes for any allowed displacement ξ away from the equilibrium. In this case, both ∇p and $j_{||}$ (that is the current density component, parallel to the magnetic field line) can be the sources for an instability to grow. In tokamak configuration, the combination of a monotonically growing q profile together with the value of safety factor on axis $q(0) > 1$ stabilizes the configuration. Even if a configuration is stable in the ideal limit, other instabilities, characterized by a slower growth rate, occur. In this case (**resistive** MHD equations), magnetic field lines tear and reconnect during their evolution: the radial magnetic component varies in space due to a current profile with a gradient localized where the poloidal component of the magnetic field changes its sign. When this gradient is sufficiently high,

a tearing instability is triggered, which causes the magnetic field lines to bend and reconnect. The resultant magnetic configuration is characterized by the presence of *magnetic islands*.

2.3 The RFP configuration

The Reversed Field Pinch (RFP) is a plasma confinement device where the two components of magnetic field (poloidal B_θ generated by toroidal plasma current and toroidal B_ϕ arising from both plasma current and external coils) are of comparable magnitude.

2.3.1 Magnetic equilibrium

The main characteristic of the RFP, which gives the configuration its name, is the fact that the toroidal field in the external region of the plasma has opposite direction with respect to the center, as shown in Fig.2.3. This means that there is a radial position where the toroidal field vanishes; this is called *reversal surface* and plays an important role in RFP physics, since it is the resonant surface for $m = 0$ modes, as it is evident using Eq.(2.6) for $B_\phi(r) = 0$.

Two dimensionless parameters are used to describe the RFP equilibrium. The *pinch parameter* Θ is defined as:

$$\Theta = \frac{B_\theta(a)}{\langle B_\phi \rangle} \tag{2.7}$$

and measures how much plasma and magnetic field are "pinched" inside the torus;

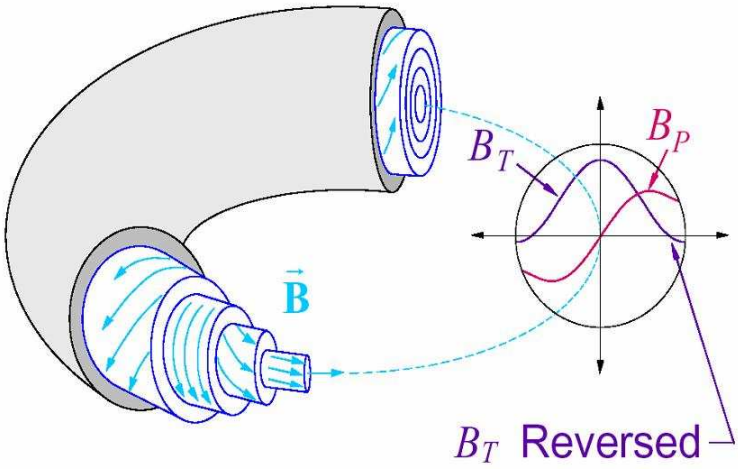

Figure 2.3: *RFP magnetic field configuration.*

the *reversal parameter* is:

$$\mathrm{F} = \frac{B_\phi(a)}{\langle B_\phi \rangle} \tag{2.8}$$

and quantifies how much the toroidal field is reversed at the edge. In Eqs.(2.7) and (2.8), $\langle ... \rangle$ indicates an average over a poloidal section.

The simplest model to compute the RFP equilibrium is the one-dimensional $\mu\&p$ model, in which the MHD equilibrium equation $\nabla p = \mathbf{j} \times \mathbf{B}$ is solved using cylindrical coordinates together with a parametric description of current and pressure profiles [33].

A more accurate model considers the toroidal geometry that results in an outward radial displacement of magnetic flux surfaces, and hence a separation (called *Grad-Shafranov shift*) between the geometrical and the magnetic axis [30]. In this representation, RFP turns out to be an axisymmetric equilibrium. But a 3D equilibrium dependent on all toroidal coordinates (r, θ, ϕ) is also possible, in which magnetic flux surfaces are deformed helically. This helical RFP state (also called **Single Helicity** (SH) state [34]) can be described in terms of a helical Grad-Shafranov equation [35, 36], which represents the full 3D solution to the MHD equilibrium equation.

2.3.2 The need of Dynamo for RFP sustainment

The q profile controls the stability in a toroidal configuration. In §2.2.1 it has been shown that resonant instabilities at radial positions where $q = -m/n$ can grow. This means that the (m,n) mode can be unstable if a radial position r_{res} into the plasma exists, such that $q(r_{res}) = -m/n$ condition is met. As the q profile crosses zero inside the plasma, resonant surfaces inevitably pack together towards the reversal surface. Numerical simulations have shown that dominant instabilities are $m = 1$ and $m = 0$. Therefore, the RFP configuration can be characterized by a spectrum of many n's perturbations. These perturbations are resistive tearing modes. If many modes are simultaneously present, the magnetic islands may overlap leading to magnetic chaos and increased radial transport. If the resistivity of the conducting wall surrounding the RFP is high (i.e. the decay time of the image currents is comparable to the discharge duration) the non resonant instabilities can occur. The growth rate of these instabilities is comparable to the wall time. These are the Resistive Wall Modes (RWM). These instabilities can be actively stabilized by means of an external coil system.

In a RFP system, where plasma resistivity is not vanishing, there is the need for a mechanism to maintain the equilibrium magnetic configuration in time [33], otherwise diffusivity would flatten the toroidal magnetic field on the *resistive diffusion time* τ_R: in a time scale of order τ_R, magnetic energy is dissipated and the RFP configuration is lost. However, experimentally the RFP configuration is maintained for times longer than τ_R [37]. This is a spontaneous mechanism of regeneration of the dissipated magnetic toroidal flux, called *dynamo* in analogy with similar phenomena in astrophysical and geophysical plasmas (see e.g. [38]). The dynamo

mechanism is responsible for the generation of an electric field E_D which sums up to the externally applied electric field and contributes to drive a current density **j**. The dynamo electric field is provided by a self-organization of plasma velocity flows, through the $\tilde{\mathbf{v}} \times \mathbf{b}$ term in the Ohm's law:

$$\mathbf{E}_D = \tilde{\mathbf{v}} \times \mathbf{b} = \sum_n \tilde{\mathbf{v}}_{1,n} \times \mathbf{b}_{1,n} \ . \tag{2.9}$$

The poloidal component of **j** is then responsible for the regeneration of toroidal field in the core and for the sustainment of its reversal at the edge. It is worth noting that in Eq.(2.9) there is no need of having many $(m = 1, n)$ terms, and the whole mechanism can be brought about by a single perturbation [39].

2.3.3 MHD fluctuations in the RFP

The RFP is externally driven by an applied toroidal electric field E_ϕ. The dissipation of power through the plasma electric resistance (often referred to as *Ohmic heating*), heats the plasma and produces peaked electron temperature profiles. Given the inverse dependence of the plasma resistivity η on electron temperature ($\eta \propto T_e^{-3/2}$, [13]), a local increase in electron temperature brings to a decrease in resistivity, and hence to a further peaking of the current density profile (at constant electric field **E**) and related Ohmic deposition. In this way, steep spatial gradients of the normalized current density profile $j_{||}/B$ tend to form, which have enough free-energy to drive unstable a broad spectrum of tearing modes with $(m = 1, |n| \geq 2R_0/a)$. The non-linear interaction of the $(m = 1, n)$ modes has been proved both by theory and experiment to generate $(m = 0, n \geq 1)$ modes, which are resonant at the reversal surface [33]. This high magnetic activity translates into a well populated spectrum of $m = 0$ and $m = 1$ modes. An example of broad $m = 0$ and $m = 1$ spectrum is shown in Fig.2.4(a) and (b). Because of the many n modes present in the spectrum, this RFP regime is also called ***Multiple Helicity*** (MH).

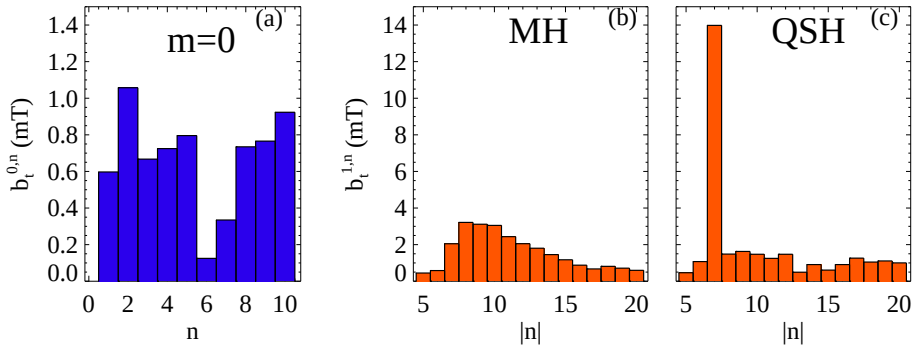

Figure 2.4: *Typical toroidal mode number spectra of* $(m = 0, n)$ *(a) and* $(m = 1, n)$ *(b-c) modes in a VS RFX-mod discharge. In frames (b) and (c) are shown examples of MH and QSH spectra respectively.*

Such a spectrum of tearing modes plays an important role in the MH dynamo, as it will be better shown in the following. Anyhow it is worth noting that the MH regime, even if it is the experimental condition historically explored first (and for a long time thought the only possible one for the RFP), it is not the unique solution to the dynamo mechanism. In fact, spontaneous helically symmetric states called ***Quasi-Single Helicity*** (QSH), in which a single mode is dominant in the $m = 1$ spectrum, have been measured in all existing RFP machines [40]; an example of QSH spectrum is shown in Fig.2.4(c). The QSH state is considered as an experimental evidence supporting the theoretical possibility for a helical ***Single Helicity*** (SH) RFP state in which only one $m = 1$ mode is present making the plasma column assume a helical MHD equilibrium [41]. QSH is different from SH, since there exists a residual fluctuation of modes with $m = 1, |n| > n_0$ (with n_0 the dominant mode): these modes are dubbed "secondary" modes.

RFP is usually found experimentally in a quasi-stationary state, where a significant magnetic activity is present. Experimentally, the theoretical SH state is not fully achieved. A residual level of secondary modes are always present together with the dominant one.

In all RFP experiments, discharges characterized by a dominant mode with amplitude $5 \div 10$ times larger than secondary modes have been observed and studied. SXR tomography reconstructions performed during QSH states reveal a highly localized bean-shaped poloidal asymmetry. This asymmetry corresponds to a sec-

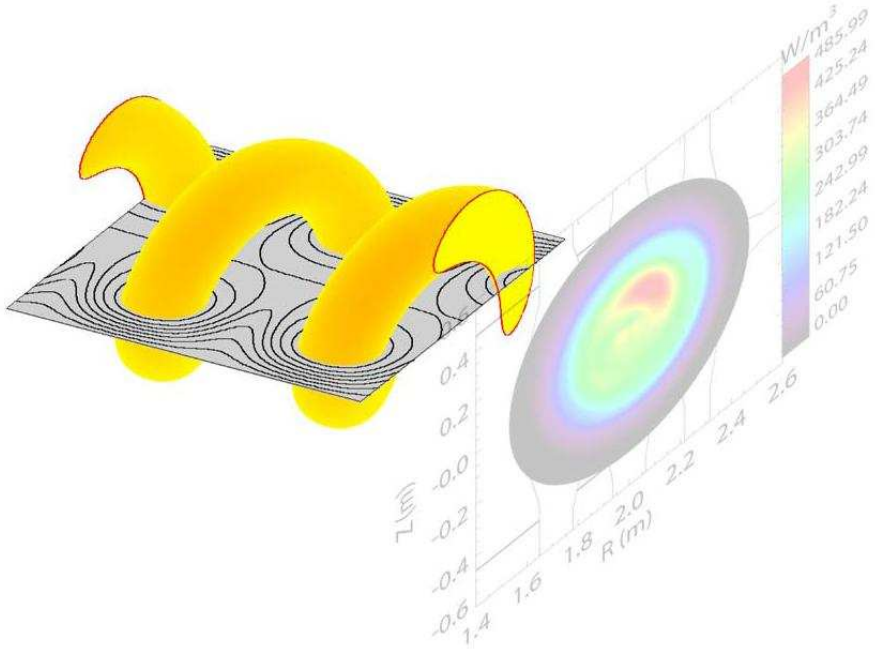

Figure 2.5: *Helical pattern of the plasma column in a QSH regimes and as it is seen as a localized bean-shaped poloidal structure by the SXR tomography.*

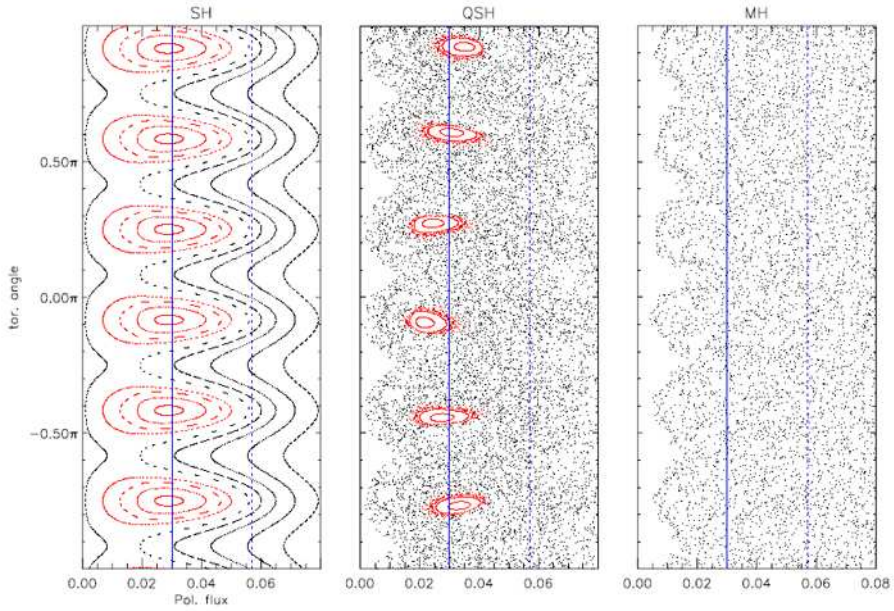

Figure 2.6: *Poincaré plots of the magnetic field lines obtained with the code ORBIT with (a) SH, (b) QSH and (c) MH magnetic mode spectra.*

tion of an helical structure with the same pitch as the dominant instability (see Fig.2.5). During MH periods, no poloidal asymmetries are observed, except transiently during low perturbation experiments where multiple structures have been detected [42].

The experimental QSH state is characterized by a low level of magnetic chaos. Chaos due to the overlapping of islands in the core vanishes and close helical flux surfaces appear, leaving an external zone still chaotic. A picture of such phenomena, in which a comparison between SH, QSH and MH is shown, can be observed in Fig.2.6 [43] where the structure of the magnetic field lines is simulated by the Hamiltonian guiding-center code ORBIT [44]. Closed helical flux surfaces are visible in the pure helical SH states, while the finite low level of secondary modes produces residual magnetic chaos around the $m = 1$ island in QSH; no conserved flux structures are present in the core of plasma in the MH state[1].

In the various dynamical regimes, equilibrium RFP fields are similar. The main difference between MH and SH (or QSH) regimes is that in the MH case, the dynamo field is produced by many modes. Their superimposition produces the average dynamo electric field necessary to sustain in time the magnetic configuration. The phenomenon can be seen as a sum of SH contributions: as underlined in Eq.(2.9) each mode induces independently a helical electrostatic potential, and hence contributes to the generation of a velocity flux pattern. The overall effect is

[1]This is true concerning plasma core; conserved magnetic structures with $m = 0$ symmetry exist at the edge, even in MH

the *turbulent dynamo*, in which the coexistence of several modes is essential for the toroidal flux sustainment. The MH state may therefore be considered as the result of a cooperation of several tearing modes, which add their axial localized helical deformation over the whole plasma volume. Anyway, there is up to now no evidence that the dynamo should be provided by many modes instead of one single mode. On the contrary, a Single Helicity equilibrium is preferable from the point of view of plasma confinement.

2.3.4 Phase and wall locking

An important feature of $m = 1$ and $m = 0$ modes in the RFP is that they tend to align their phase in order to minimize the total magnetic torque. The corresponding feature in real space is called *slinky* or *locked mode* [45]; if the slinky is also stationary in the laboratory frame of reference, modes are *wall locked*. We define as locking angle Φ_{LOCK}, the toroidal position of the maximum perturbation. The slinky has a great importance for the characteristic of the RFP plasmas, since it determines a strong plasma-wall interaction. In particular, in the RFX-mod experiment, with a careful tuning of the active coil system, it has been possible to move the slinky position during the discharge, thus reducing the localized heat and particle flux to the wall.

2.4 Two RFP experiments: RFX-mod and MST

The analysis and results reported in this thesis have been performed on SXR measurements coming from two RFP devices: the Reversed Field eXperiment (RFX) and the Madison Symmetric Torus (MST). RFX is located in Padova, Italy, while MST is at the University of Wisconsin-Madison. These two laboratories are involved in a long standing collaboration project, developed within the framework of the IEA implementing agreement on reversed field pinches. This activity is part of the collaboration between RFP groups for experimental studies on MHD processes and magnetic self-organization in the RFP configuration, which are very important issues for the understanding of the RFP confinement and dynamics.

2.4.1 The Reversed Field Pinch eXperiment

The *Reversed Field eXperiment* [46], with $R_0 = 2$m and $a = 0.459$m for an aspect ratio $R_0/a \approx 4$, had been operated by the Consorzio RFX in the framework of the Euratom-ENEA Association up to 1999 in Padova (Italy), when experimental activities were interrupted due to a major accident. On that occasion, the passive Al shell (65mm thickness with 450ms vertical field penetration time) used for plasma stabilization and essential for RFX operation, has been replaced with a Cu thinner shell (3mm thickness and 50ms vertical field penetration time), thus the name **RFX-mod**. This replacement is in the framework to approach RFPs and their operations to the studies relevant for the realization of a fusion reactor, based on the

Figure 2.7: *Picture of the RFX-mod RFP device, operating at Consorzio RFX in Padova, Italy (http://www.igi.cnr.it).*

Tokamak configuration which is lacking of the passive shell. In absence of this passive structure, RFP equilibrium and stability have to be guaranteed in another way. In RFX-mod, this is ensured by a set of 192 (4 poloidally $\times$ 48 toroidally) feedback controlled saddle coils with independent power supplies [47]. They allow for mimicking an ideally conducting wall by locally opposing the radial field (*Virtual Shell*, VS) or actively controlling individual magneto-hydro-dynamic modes. A picture of RFX-mod is displayed in Fig.2.7.

The coils surround the thin copper shell, and under each of them a radial field sensor of the same area is mounted on the internal part of the shell, so that the flux at the sensor can be exactly balanced by a suitable current in the active coil. Each coil is individually fed with a maximum current of 400A, with a maximum static radial field generated at the plasma edge of 50mT (3.5mT at 100Hz). They can generate magnetic field harmonics with $m = 0, n = 1 \div 24$ and $m = 1, n = -23 \div 24$. A digital feedback system controls toroidal and poloidal circuits, toroidal equilibrium and saddle coils. For MHD control, it performs two-dimensional FFT of B_r and B_ϕ measurements, compares it with the reference values and computes via inverse FFT the required references. This permits to control the MHD modes selectively and has been used for several control schemes.

The toroidal field winding system consists of 48 coils evenly distributed around the torus. The maximum toroidal bias magnetic field produced is $B_\phi \approx 0.7$T at the beginning of the discharge, and a reversed field at the wall of $B_\phi(a)$ up to 0.44T during the current flat top. The poloidal flux, which causes the plasma current rise through Faraday's law, is provided in RFX-mod by the so called magnetizing winding. The plasma can be thought as the single turn secondary circuit of a transformer: a flux variation in the primary circuit produces an electromotive force in the plasma, which ionizes the neutral gas and drives the toroidal current. No iron

core was adopted in order to reduce magnetic ripple and to improve the accessibility. The first wall is composed of 2016 trapezoidal graphite tiles, covering the entire inner surface of the vacuum vessel. Graphite was chosen because it is resistant to high temperature ($\sim 3000^{\circ}$K) and it is a low Z material, in order to keep the plasma Z_{eff} value low.

With these new features and thanks to its capability of operating at high current (up to 2MA), RFX-mod mission is to investigate the physics of RFP configuration in high current regimes. To this aim, a large set of new plasma diagnostic has been developed to better characterize the plasma discharge. Beneficial effects of the MHD active coil system resulted in a increase of the pulse duration up to ≈ 0.5s, with about 0.2s of flat top (to compare with about 100ms of pulse duration in RFX). The maximum plasma current achieved at the time of writing this thesis is ~ 1.5MA: an example of the plasma current I_p discharge and several main plasma parameters like F, Θ, electron density n_e, on-axis electron temperature T_e, and the temporal evolution of instabilities $m = 1, n = -7 \div -11$ are illustrated in Fig.2.8.

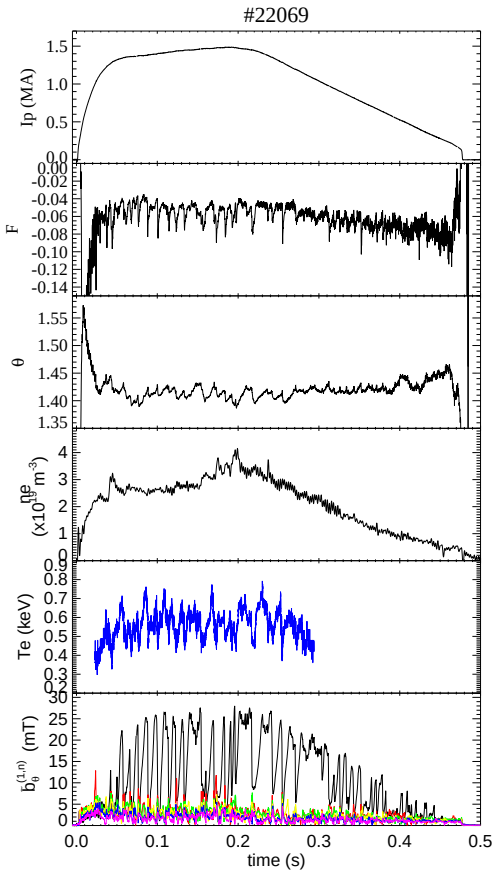

Figure 2.8: *RFX-mod discharge: example of the highest value of plasma current achieved, together with several main plasma parameters.*

By means of the saddle coil system, various operational schemes can be performed (here, only few of them are briefly described):

VS operation. A feedback scheme is set up in order to minimize the radial component of the field at the sensors for each helicity (excluding the equilibrium field $m = 1$, $n = 0$) [48]. Sometimes, only selected modes are kept low with different feedback, while other ones remain uncontrolled. This latter case is called Selective Virtual Shell (SVS): the radial field of each harmonic resolved by the sensor coils can in fact be independently controlled.

VS operation + rotating perturbation. A finite amplitude (static or rotating) ref-

erence is added to a selection of modes. This is used for mode rotation or for studying the controlled growth of some modes [49].

VS + complex gain. This scheme applies the regulators to the modes rather than to the individual sensors: a *complex gain* can be pre-set to each mode, i.e. the feedback system applies an out-of-phase cancelation of the mode, realizing an alternative algorithm for mode rotation [49].

Clean Mode Control. This operational condition has been developed to overcome an intrinsic problem in the VS coil system, due to the aliasing in the measurements of the high n harmonics produced by the saddle coil system [50, 51]. This configuration has allowed for overcoming 1MA (now, 1.5MA has been achieved with this operation), mitigating the problem of the localized heat deposition over the first wall.

Pulse Parallel Current Drive (PPCD). This technique, applied at first in the MST experiment [52, 53], aims at producing a poloidal electric field, driven inductively at the plasma edge by pulsing the toroidal field. It transiently replaces the plasma dynamo, resulting in a strong reduction of magnetic perturbation and in a simultaneous energy confinement improvement. PPCD is intrinsically transient in nature. In fact, in order to inductively drive a poloidal electric field in the plasma, one has to ramp the external toroidal field towards more negative values. After a few ms the toroidal field reversal is so deep that the magnetic configuration becomes prone to spontaneous large relaxation events and the PPCD has to be stopped anyway. Further details on this technique in RFX can be found in [54].

Oscillating Poloidal Current Drive (OPCD). In this scheme, the beneficial effects of PPCD during its initial phase are extended, by applying an external oscillation of $B_\phi(a)$ (several cycles of oscillation during the plasma current flat top as a sequence of PPCD pulses). In general, this operation allows for high plasma performances (high T_e and high duration of QSH states) [55, 56].

Self Similar Current Decay (SSCD). The aim of this operation is to reduce the RFP dynamo by imposing suitable decaying boundary conditions by acting on the toroidal voltage at the plasma edge. This operational mode, called self-similar current decay (SSCD), is attractive when the resistive diffusion time is high enough to allow a slow decay rate [57]. This regime shows a decrease in mode amplitudes and magnetic chaos when the magnetic field is forced to decay at a suitable rate in a fixed radial profile. In these shots, plasma current reaches a maximum value, followed by a linear decay with a rate depending on the resistive time constant. The toroidal flux follows the current decay without the need for an additional significant control on the poloidal voltage. With this operation, plasma is believed to pass through

self-similar states, in which the equilibrium profiles remain approximately constant during the decay.

2.4.2 The Madison Symmetric Torus

The Madison Symmetric Torus (MST) is a RFP device located at the Department of Physics at the University of Wisconsin, Madison (USA) [58]. A picture of the MST device is shown in Fig.2.9. The aspect ratio of the MST machine is $R_0/a = 1.5m/0.52m \approx 3$. The plasma current can reach values up to $I_p \approx 0.6$MA, with density of the D filling gas of order $1 \times 10^{19}\mathrm{m}^{-3}$. MST is characterized by a close fitting aluminum conducting shell, 5cm thick. The shell acts both as a vacuum chamber, magnetic flux conserver and single turn toroidal field winding. Current is driven in the shell through a transformer and a capacitor bank power supply. Toroidal and poloidal fluxes are applied through a toroidal and a poloidal gap respectively. The mechanical structure of the MST shell simplifies the diagnostic access and also reduces the magnetic field inhomogeneity. Another important characteristic of this experiment is the presence of a single ring-shaped iron core winded by conducting coils, forming the so-called primary circuit.

During the discharge, the RFP magnetic configuration is sustained by both discrete dynamo events, called sawteeth, and a continuous dynamo between these events. Discrete dynamo events produce a large toroidal flux regeneration, and are associated with bursts of magnetic fluctuations (mainly $m = 0$).

The MST experiment is characterized by a high operational flexibility and simple diagnostic access. A variety of plasma scenarios can be investigated in this device, and the experimental control parameters can be varied rather independently in a wide range. In the following, a summary of the most used discharge types is

Figure 2.9: *Picture of the MST RFP device, operating at the Department of physics at the University of Madison, Wisconsin.*

presented.

Sustained discharge. Both the plasma current and the electron density waveforms are maintained almost constant during the flat-top phase of the discharge, from 5 to 40ms. Typically, quasi-periodic discrete dynamo events (sawteeth) are present in these discharges. The reversal parameter F and the pinch parameter Θ show a sawtooth-like temporal dynamic, which represents the rearrangement of the magnetic profiles during relaxation events. During the slow phase of the sawtooth cycle ($\triangle t \sim 5$ms), the externally provided poloidal flux increases up to a point when a discrete dynamo event is triggered. This rapidly ($\triangle t \sim 100\mu$s) converts the poloidal flux into toroidal flux, which is represented by a fast decrease in the value of Θ and a deepening of the toroidal field reversal. This strong dynamo activity is associated with an increased level of magnetic fluctuations, which produces high thermal transport and a fast relaxation of the temperature profile.

Decaying discharge. The current waveform is not sustained in time, and can also be forced to decay with different slopes. The electron density is kept almost constant. Sawtooth events are almost suppressed during the current decay, due to the fact that the need for dynamo is reduced. This produces a period in which the magnetic fluctuations, even though not strongly suppressed, do not exhibit the strong activity typical of sawtooth crashes. These discharges are thus more suitable for the application of PPCD, because the strong $m = 0$ activity associated with sawtooth crashes does not interfere with its action. This type of operation is similar to SSCD in RFX-mod.

PPCD discharge. The PPCD strongly increases the pinch effect and the toroidal magnetic field reversal. This transient modification of the magnetic field and current density profiles reduces the magnetic fluctuations, and has a strong effect on the confinement properties of the plasma [53]. A decaying discharge is the typical shot in which PPCD is applied, as this is the situation where this control technique has given the best performances up to now. Nevertheless, PPCD can be applied rather flexibly also in other types of discharges.

All of the discharges presented above can be produced starting from values of the plasma parameters in the following typical ranges: plasma current $I_p < 0.6$MA; electron density $0.5 \times 10^{19} < n_e < 3.0 \times 10^{19}$ m^{-3}; and reversal parameter $-0.5 <$ F ≤ 0.

In particular, the density can be increased in MST by pellet injection. In this thesis attention has been given to high current PPCD shots ($I_p \approx 500 - 550$kA), since high SXR fluxes, low fluctuations and high T_e are associated to these operational regimes. An example of high current PPCD shot is illustrated in Fig.2.10: the plasma current I_p, the F parameter (reaching deep values of about -1.5), Θ, the electron density n_e (which is lower than in a typical RFX-mod experiment), the

temporal evolution of one experimental signal from the SXR tomography and of the magnetic instabilities $m = 1, n = 6 \div 12$, are displayed.

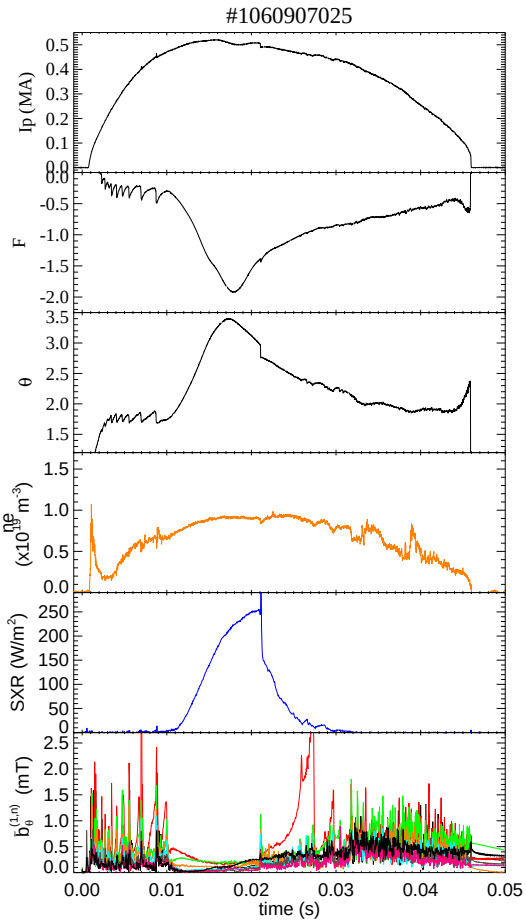

Figure 2.10: *High current PPCD discharge in the MST device.*

CHAPTER 3

Soft X-ray radiation in magnetic confined plasmas

3.1 Soft X-ray radiation in fusion devices

Thermonuclear plasmas emit a rich spectrum of electromagnetic radiation. These plasmas are complex media: they are composed by different kind of charged particles, in particular ions may be partially ionized; electric and magnetic fields are partially produced by particle motions. Radiation can be produced both by classical and quantum-mechanical effects. Finally, the mixture of particle, photons and external fields is usually far from thermodynamical equilibrium. At temperatures and densities relevant for fusion, most of the power is radiated between the visible and the x-ray regions. Moreover, reabsorption of such radiation is almost negligible, therefore the spectrum of radiation contains information about the plasma that emitted it. This limit is due to different generation mechanisms. The most important contributions to plasma radiation are:

Bremsstrahlung. Continuum of radiation, due to the free-free interaction of electrons in the electrostatic field of ions.

Line radiation. Line radiation is due to transitions of the electrons in different bounds in partially ionized ions. This contribution is strictly linked to the presence of impurities in the plasma, coming from the vacuum vessel or other components installed inside the vessel and in contact with the plasma.

Recombination. Continuum of radiation due to electrons which are captured by ions.

In a typical magnetically confined fusion plasma, the temperature of about 1keV leads to a maximum in the plasma radiation emissivity in the energy range of soft X rays (SXR). For low Z (atomic number) impurities, the maximum power radiation is at low temperatures (like for Oxygen or Carbon), and as soon as the temperature increases electrons are removed from ions until obtaining fully stripped ions (and in this case, only continuum contribution is thus present). In a reactor plasma (with temperature of about 20keV), the maximum will be obtained for impurities with high Z number. In actual devices for fusion research, bremsstrahlung is the most important contribution to the SXR radiation.

SXR radiation is a strong function of the electron temperature (T_e) and the electron density (n_e): if line radiation is negligible, SXR plasma emissivity is proportional to $n_e^2\sqrt{T_e}$. The kinetic pressure p in the gas theory is proportional to the product $n_e \cdot T_e$. Moreover, the MHD theory shows that $p = (n_e T_e + n_i T_i)$, which is the sum of the kinetic pressure for electrons (e) and ions (i), and it is constant among the magnetic surfaces. Thus, the isobaric surfaces are therefore also magnetic flux surfaces. The parallel thermal conductivity (parallel to the magnetic field lines) is higher than the perpendicular one, so the thermal equilibrium along the magnetic field lines is achieved rapidly. If the presence of impurities is negligible, $n_e = n_i$, and therefore $p = n_e\ (T_e + T_i)$. Both electron temperature and density are constant throughout the surface: this implies that SXR emissivity is also constant. SXR images are therefore a useful tool to investigate the topology of magnetic surfaces.

Emissivity maps of SXR radiation cannot be directly measured. Detectors need to be located outside the plasma and therefore radiation coming from different region is collected. If the collection region is properly designed, the measurement is proportional to the line-integral of radiation along a line of sight (see §3.2.1) and therefore tomographic techniques can be applied (§3.3). Moreover, direct estimates of electron temperature can be performed (§3.4).

3.2 SXR measurements in plasma devices

The containment of plasmas, RFP in particular, requires a complex boundary that absorbs the radiation emitted by the plasma. Moreover, SXR radiation is rapidly absorbed in air; therefore detectors need to be placed in vacuum: the containment structures need to be modified in order to allow for mounting manipulators that bring detectors sufficiently close to the plasma. The number of these diagnostic accesses is limited, because they locally degrade the quality of the magnetic configuration. Finally, high level of electromagnetic noise is emitted both by the plasma and by the confinement winding around it: detection of weak signals therefore requires careful design. Let us also note that SXR diagnosis in burning plasmas is still an open issue, because of the presence of fast neutrons that quickly destroy the detection capabilities of silicon photodiodes. At present RFP neutrons are mostly absent, therefore PIN diodes are used.

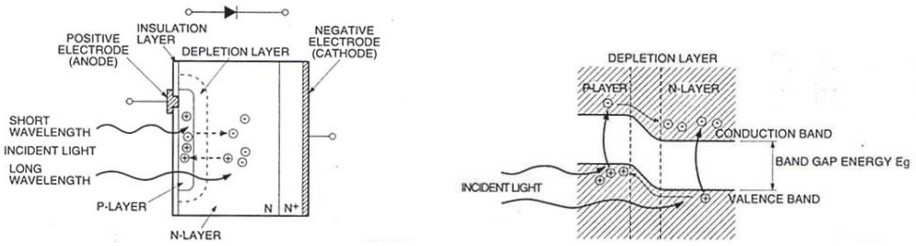

Figure 3.1: *Scheme of a photodiode.*

All the diagnostics considered here for SXR radiation detection in RFPs use PIN photodiodes (n-p junction for most of the cases) mounted on ceramic (insulated) supports, acting as radiation-current converters: a photon impinging on the diode volume produces a number of electron-hole couples proportional to the photon energy, giving rise to current I_{diode} mostly proportional [14] to the impinging power P_{in}, $I_{diode} = k \cdot P_{in}$, where $k = (1/3.6) = 0.278\text{A/W}$.

A schematic photodiode view is displayed in Fig.3.1. If "A" indicates the p-layer, "B" the depletion layer and "C" the region not taking part in the current production, the power absorbed by the photodiode is a function of the energy E as in the following:

$$A(E) = T_C(E)\ ((1-T_A)\ (1-T_B)) \tag{3.1}$$

$$= \mathrm{e}^{-\mu_C(E)t_C}\ \left((1-\mathrm{e}^{\mu_A(E)t_A}) + (1-\mathrm{e}^{-\mu_B(E)t_B})\right) \tag{3.2}$$

where T_A, T_B and T_D are the transmission functions of the three regions; t_A, t_B and t_C are the thicknesses and μ the absorption coefficients of the three regions. These kind of detectors are characterized by a high sensitivity to the impinging radiation,

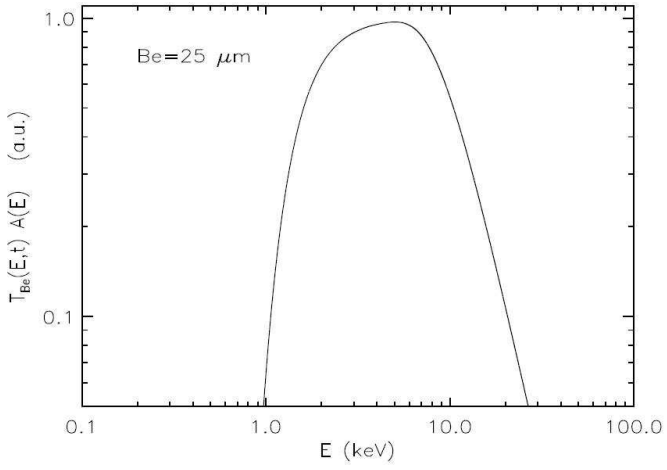

Figure 3.2: *Pass-bandwidth function of "Be filter+photodiode" system, as function of the energy impinging onto a detector.*

a fast response time and good mechanical characteristics. Detection energy range is wide, from the visible to the x-rays. In order to restrict the detection to SXR, which is dominated by bremsstrahlung and recombination radiation, Be filters of appropriate thickness are used. These Be foils act as high-pass filters, with a lower cut-off energy depending on their material thickness. On the contrary, the thickness of the photodiode acts as a low-pass filter: the sandwich system "Be foil + detector" acts as an energy limited band-pass system, centered in the SXR range (see Fig.3.2). The Be filter should be thick enough so that line radiation is not detected.

The Be filter transmission function can be expressed as in the following:

$$T(Be,E,t) = \mathrm{e}^{-\mu_{Be}(E)t} \tag{3.3}$$

where t is the foil thickness, and μ_{Be} the Beryllium absorbing coefficient. This is an approximation [59] valid in the energy range of interest.

3.2.1 Geometry of the lines of sight

Detectors look at the plasma throughout a pinhole, which limits and defines the region of observation. The finite sizes of detector and pinhole define a cone of observation, whose axis is called ***line of sight***. The radiation impinging on the photodiode comes from plasma inside this volume. The perpendicular size of the cone of observation needs to be sufficiently small, so that the emissivity in the direction perpendicular to the line of sight can be considered constant. Under this approximation, the measurement can be identified as a line-integrated measurement along the line of sight, where the "volume" contribution is included in a geometrical factor f_g,

$$f_g = \frac{A_{dect}\, A_{ph}}{4\pi\, d^2}\, cos^4(\alpha). \tag{3.4}$$

Here, A_{dect} and A_{ph} are the areas of the photodiode and of the pinhole, respectively; d is the distance between the detector and the pinhole, while α is the angle between the line of sight and the normal to the pinhole. This case is referred to as *line approximation*.

Usually, a large number of single photodiodes lying in the same plane is positioned inside one of the vessel portholes and uses a unique pinhole, in order to obtain a fan of lines of sight emanating from the same pinhole. This line arrangement leads to a systematic error if the Be filter is flat: as each line of sight crosses the filter at a different angle, each detector measures radiation through a different effective Be thickness. An approximated correction algorithm was developed, as the effect on the signal is not simply a geometrical constant, but it depends also on the temperature [24]. During the working-out of this thesis, pinhole filters of the tomographic diagnostic installed in RFX-mod have been modified, in order to avoid this error; in MST the SXR tomography has been designed with curved filters.

3.3 SXR tomography: algorithms and diagnostics

3.3.1 Tomographic algorithms for plasma emissivity reconstruction

Simultaneous SXR measurements of the same plasma cross-section (usually the poloidal cross-section) with a large number of lines of sight spatially uniformly distributed and covering the entire section allow for the reconstruction of the plasma SXR emissivity distribution by means of tomographic algorithms. Each line of sight is uniquely identified by means of the impact parameter p (that is the distance of the lines of sight from the vessel geometrical center) and the ϕ parameter (the angle between the equatorial plane and the normal to the chord itself). Eq.(1.2) is expressed in this notation as:

$$f(p,\phi) = \int_{L(p,\phi)} g(r,\theta)\ \mathrm{d}l \tag{3.5}$$

and plasma emissivity reconstruction corresponds to find out a solution of the problem of inversion for this equation. The constructive solution proposed by Cormack is well suited for fusion plasma application as the emissivity is very well approximated by a few angular harmonics. The Fourier series expansions of the experimental brightness f and the emissivity g,

$$g(r,\theta) = \sum_{m=0}^{M} \left(g_m^c(r)\cos(m\theta) + g_m^s(r,\theta)\sin(m\theta)\right) \tag{3.6}$$

$$f(p,\phi) = \sum_{m=0}^{M} \left(f_m^c(p)\cos(m\phi) + f_m^s(p,\phi)\sin(m\phi)\right) \tag{3.7}$$

lead to a 1:1 correspondence for the m-harmonic of the experimental measurements f_m and of the unknown emissive distribution g_m,

$$g_m^{c,s}(r) = -\frac{1}{\pi}\frac{\mathrm{d}}{\mathrm{d}r}\int_r^1 \frac{f_m(p)\ T_m(p/r)\ p\ \mathrm{d}p}{\sqrt{p^2-r^2}}. \tag{3.8}$$

At first, each Fourier component $g_m^{c,s}(r)$ was expanded over a truncated set of Zernicke polynomials $Z_{ml}(r)$:

$$g_m^{c,s}(r) = \sum_{l=0}^{L} a_{ml} Z_{ml}(r). \tag{3.9}$$

But this decomposition generates artifacts (i.e. spikes) at the edge of the 2-dimensional surface $g(r,\theta)$ [60], due to the fact that $Z_{ml}(1) = 1$ and to the inevitable truncation of the finite sum. This constraint has been overcome by expanding the components over Bessel polynomials [25]:

$$g_m^l(r) = J_m(\lambda_m^{l-1} r), \tag{3.10}$$

where $\lambda_m^{l-1} r$ is the lth zero of the mth order Bessel function $J_m(z)$. The advantage of this basis is that $J_m(\lambda_m^{l-1} r)$ is zero at boundary, with zeros uniformly far from each other in the range [0,1] (normalized units).

Thus, the integral equation Eq.(3.8) becomes an algebraic system:

$$\mathbf{f} = \mathbf{W} \cdot \mathbf{g} \tag{3.11}$$

where the unknowns are the components of the emissivity vector **g**, while **W** is a known matrix based on the geometry of the detection system. The system can be solved by linear algebraic techniques, i.e. the inversion problem is reduced to the inversion of the **W** matrix. As the matrix is not squared, Pseudo-inversion techniques need to be applied. Approximated solutions are found by minimizing the residual, defined as [61]:

$$||\mathbf{r}||_2 = ||\mathbf{W} \cdot \mathbf{g} - \mathbf{f}||_2 = \sqrt{\sum_i (\mathbf{W} \cdot \mathbf{g} - \mathbf{f}_i)} \tag{3.12}$$

The solution can be determined by means of the Singular Value Decomposition (SVD). Details on SVD decomposition can be found in [61]. For further details on the tomographic algorithms, see Apx.A.

3.3.2 SXR tomography in RFX-mod

The SXR tomographic diagnostic was developed and realized for the RFX experiment [24, 62] in 1990s, with standards compatible with the requirements of large fusion experiments. In particular, the most severe constraints which had to be considered were:

a) The highest temperature (300°C) at which the first wall was kept during operation or baking (in RFX-mod, the highest temperature is of about 150°C).

b) The ultra-high vacuum conditions of the vessel (base pressure of 10^{-9}mbar).

c) The need for full remote control of the diagnostic and for the capability of decoupling it from the machine without breaking the RFX main vacuum.

d) The fast timescale (down to fractions of milliseconds) which characterizes the configuration setup and the evolution of some important physical phenomena.

e) The relatively high level of electromagnetic noise.

The diagnostic is composed of four units, each one divided into several parts [62]: the insertion and detection unit, the supporting structure, the signal processing electronic unit, the data acquisition unit, the head temperature conditioning circuit, the control and safety systems, the detectors and the in situ electronic calibration system.

The insertion subsystem includes a bellow drive manipulator which brings the photocamera to its operating position with a positioning error of ± 0.1mm. The manipulator is supported by independent mechanical structures, anchored to the floor to decouple the diagnostic from machine vibrations. The vacuum vessel and plasma motions and vibrations relative to the mechanical support structures are very small. Each head can be kept at a selected steady temperature in the range $8 \div 90^{\circ}$C by means of a water cooling circuit.

The SXR pinhole photocamera of each unit has a cylindrical shape, with a diameter of 83 or 89mm and use silicon photodiodes as detectors. The four SXR cameras, named VDE, VDC, VDI and HOR, house a total of 78 detectors, each viewing the plasma through a different line of sight at the same poloidal cross-section. The arrangement of the photocameras and of the chords is shown in Fig.3.3. Different material foils can be interposed between the pinhole and all the detectors of each photocamera by means of a five position filter wheel; only one filter at a time can be used for each head. For the measurements described in this article four of the foils are made of beryllium, with thicknesses of 25, 75, 150 and 225μm; the $1/e$ energy cut-offs for these material filters are 1.4, 2.0, 2.6 and 3.0keV, respectively. The fifth foil was blocked by a thick plate of stainless steel.

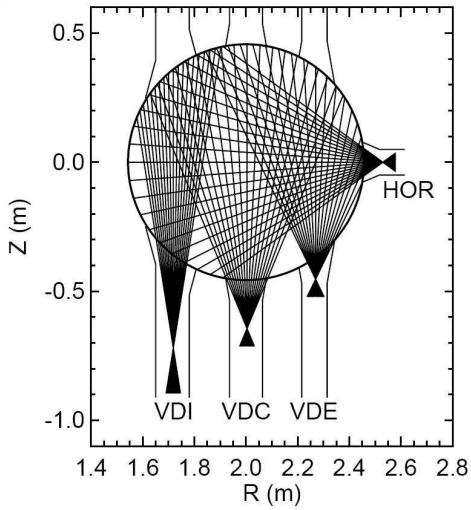

Figure 3.3: *Lines of sight of the RFX-mod SXR tomography.*

The current generated in the detectors (of the order of nanoamperes) is received and processed by analog electronics, located in cubicles close to the machine. Amplified signals are digitized in the same board with a 1 MHz sampling rate and 12 bit resolution. The signals are then optically converted and, along optic fiber, transmitted via TAXI link to the VME units, located in a different room. The SXR amplifiers provide a fully differential conversion to voltage of the photocurrent produced by the detectors, the subtraction of the offset and dark current, amplification, and hardware filtering of the voltage signal. They also supply the bias voltage needed to polarize the detectors. Five selectable values of the transimpedance ($10^5, 10^6, 10^7, 10^8,$ and10^9 V/A) and four values for the voltage gain (1, 2, 5 and 10) have been implemented, for a maximum overall gain of 10×10^9V/A. The overall bandwidth of the SXR electronics is controlled by an eight-pole Bessel filter with six selectable cutoff frequencies, from 2 to 250kHz. All the amplifiers settings can be remotely controlled from the control room. Moreover, with specially developed

calibrator circuits the gain of SXR amplifiers can be absolutely calibrated with an accuracy of 1%.

Curved Be filters for SXR tomography

The original supports of the Beryllium foils, both in the pinhole and in the filter wheel, housed flat Be filters [24]. That implies for most of the detectors and the pinholes not to be perpendicular to the lines of sight: if α is the angle between a line of sight and the perpendicular to the foils, the effective thicknesses of the filter crossed by this chord is increased by a factor $1/cos\alpha$. Therefore, in an individual camera, each detector crosses a filter of different thickness. The consequence of the non-normal incidence and of the differences in filter thickness is that the vertical brightness profile is generally discontinuous, corresponding to the superimposition of the VDE-VDC and VDC-VDI line of sight fans, and the profiles are "bent down" at the edge. An example of such brightness profile is illustrated in Fig.3.4(a). The difference between chords with similar impact factor p (i.e. for lines of sight observing approximately the same region of plasma) is of the order of 20%, which is more than the unavoidable experimental uncertainty of the signal. If these data are directly used in the inversion algorithms a clearly not physical artefact is obtained. To avoid this problem, a correction algorithm based on a SXR emissivity distribution model has been developed [24], so that the vertical brightness profile results homogeneous, and no discontinuities are present any longer. Recently (summer 2007) this source of systematic error has been removed. New curved supports have been installed in the pinhole, with a curvature centered in the pinhole itself. New "sandwich" curved supports have been developed and mounted also in the filter wheel, always centered in the pinhole. In this way, all the effective Be filter thicknesses are the same for all the detectors. Thus, the homogeneous measurements give rise to a "continuous"vertical profile, with no discontinuity, as

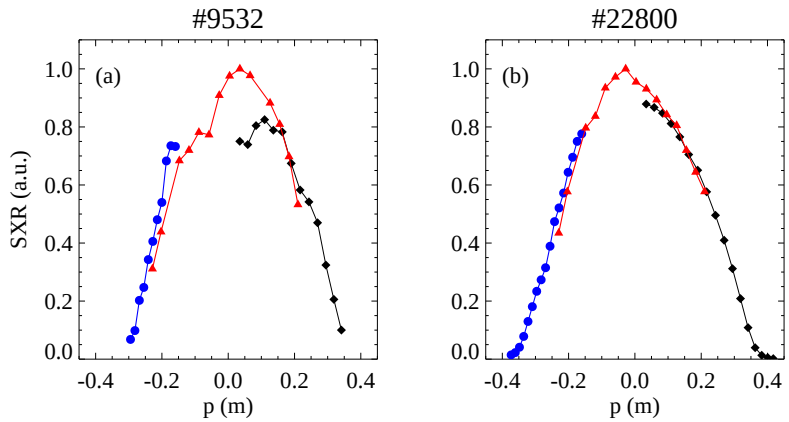

Figure 3.4: *Vertical SXR brightness profiles (normalized units) with the original flat support for Be foils (a) and with the new curved supports (b).*

illustrated in Fig.3.4(b): the measurements from the three different vertical cameras are matching very well, and no algorithm correction is thus needed.

3.3.3 The MST tomographic diagnostic

The SXR tomographic diagnostic installed in the MST device has been developed and realized by the RFX group in the framework of the IEA implementing agreement on reversed field pinches.

The diagnostic is composed of four units, labeled from SXR1 to SXR4 [63]; see Fig.3.5 for a layout of the diagnostic. All the probes are installed on 1.5 inches portholes of the MST vacuum vessel, in the same toroidal location. SXR1, SXR2

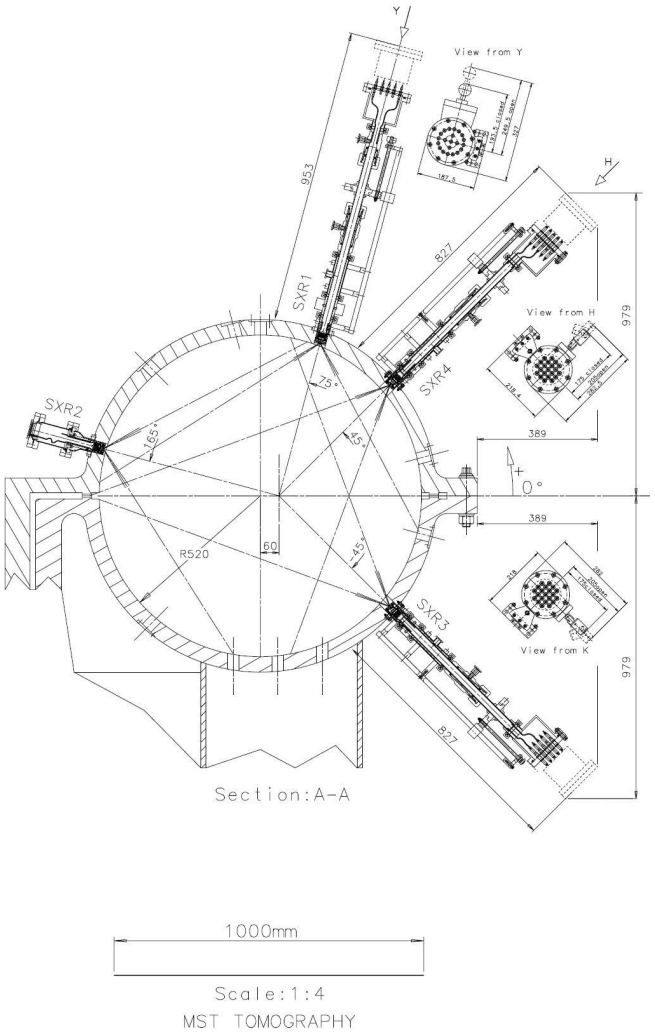

Figure 3.5: *Layout of the MST tomographic diagnostic: view of the four probes in the poloidal section.*

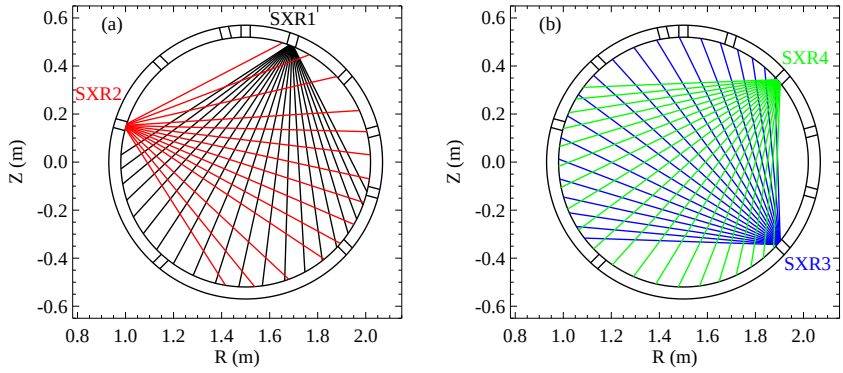

Figure 3.6: *Lines of sight for (a) the probes SXR1-SXR2 and (b) SXR3-SXR4.*

and SXR3 probes (located respectively at 75, 315 and 45 poloidal degrees) are mounted on manipulators. The SXR2 (at 165 poloidal degrees) is more compact and was placed in a fixed position. Recently this limitation has been removed and also SXR2 is now mounted on a manipulator. A scheme of the 34 lines of sight for probes SXR1 and SXR2 is illustrated in Fig.3.6(a), while the 40 chords of SXR3 and SXR4 are showed in Fig.3.6(b).

All the instruments can be divided in two subsystems: the photocamera, which contains the detectors, and the mechanical support, used to place the SXR photocamera at its operating position.

The photocamera is a 35mm-diameter aluminum cylinder, closed by an aluminum disk on one side (which is the part exposed to the plasma) and attached to a metal tube on the other. An array of 20 silicon photodiodes, mounted on a teflon socket, is installed inside the camera. The array used in all the photocameras is the AXUV-20ELM 20 diodes array manufactured by International Radiation Detectors, Inc., [1] (the "M" stands for a modified version of the array chip with smoothed corners, ordered for compatibility with the photocamera dimensions). The diodes (in a common anode configuration) have an active area of 0.7534mm^2, with an active thickness of 35mm, and are used without bias voltage (absorption of photons is up to $6 \div 7$keV).

The front aluminum disk contains a small slit (pinhole) and a curved beryllium foil. The pinhole ($1 \times 4\text{mm}^2$ for all cameras) is used to define the geometry of the lines of sight (see Fig.3.6 for their displacement into MST vessel): four fans of lines of sight are defined, for a total number of 74 chords. Several rings can be inserted to modify the distance between photodiodes and the corresponding pinholes, thus reducing the angular aperture of the set of the lines of sight.

A thin beryllium foil is placed on the frontal disk, between the pinhole and photodiodes, and acts as high pass energy filter to select only the SXR radiation and

[1] I.R.D., 2575 West, 237th Street Unit C, Torrance, CA 90505-5243, http://www.ird-inc.com

to stop the visible light. The thicknesses of the foils have been manually selected in order to be as homogeneous as possible (a tolerance of 1μm in the thickness measurement is accepted). The photocameras are all equipped with curved Be foils, included in an arc frame, and all of the lines of sight (displayed in Fig.3.6) are perpendicular to the surface of the absorber.

The common anode configuration of the photodiode array has been carefully studied and finally the optimal grounding layout has been designed. In this case the circuit has been grounded directly on the array socket, through small wires connected to the metal housing and to the MST vessel. The detectors can be, in fact, very sensitive to pickup noise but it has been found that this configuration significantly reduces this noise. The output currents of the diodes (in the range of 20nA to 10mA) are processed through current-to-voltage amplifiers. Both commercial and custom made transimpedance linear amplifiers are used, with bandwidth ranging between 10kHz (edge chords) and a few hundreds kHz (for the lines of sight looking at the core of the plasma). The signals are then digitized in CAMAC-type digitizers (16 channels per unit, 12 bit resolution) with a sampling rate of 500kHz. To further reduce noise, isolated variable amplifier stages (gains of $1\times$, $2\times$ and $5\times$) have been installed between the output of the amplifiers and the inputs of the digitizer.

3.4 From SXR brightness to *Te* estimation

While for one single particle in an appropriate toroidal device the confinement is perfect, collisions, drifts and MHD turbulence in a plasma lead to a radial transport of particle and energy, which determines crucial parameters of plasma such the global energy and particle confinement time. In particular, the latter is strictly linked to the determination of the electron temperature T_e [13], which is a fundamental parameter for understanding plasma physics behavior in view of a fusion reactor.

The strong dependence of the SXR brightness on the plasma electron temperature T_e can be exploited in order to obtain an estimate of this important plasma parameter with high temporal resolution. This technique, called ***two-foil technique*** [59, 64, 65], is based on the ratio between two experimental SXR signals using Be foils which are different in thickness but looking at the same plasma region. This is valid under the assumption that plasma particles have a Maxwellian distribution function and that therefore the bremsstrahlung formula is a good approximation of the plasma emission in the SXR range. An adequate choice of Be thicknesses in order to avoid line radiation affecting the measurements makes the resulting ratio R be a function of T_e only.

Let us consider a plasma emissivity as in the SXR model described in Apx.C. Two bremsstrahlung measurements (SXR_1 and SXR_2) calculated with Eq.(C.1) and looking at the same plasma region (e.g. with two overlapping lines of sight, L_1 and L_2) through two different Be foil thicknesses, t_1 and t_2, can provide a measure of

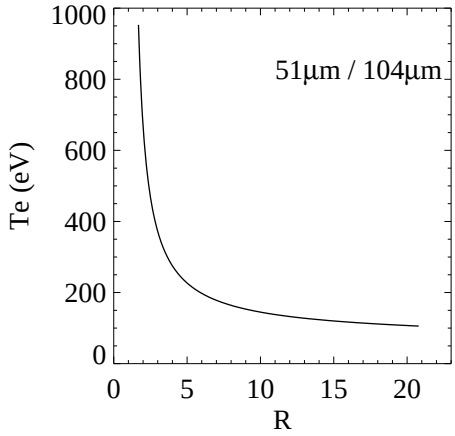

Figure 3.7: *The fitting curve representing the function relation between the ratio R and the temperature T_e computed for two diodes of the multichord diagnostic installed in the RFX-mod device (see §3.4.1), having with Be filters of 51 and 104μm.*

the highest temperature along the line of sight considered [59]:

$$R(T_e) = \frac{SXR_1(t_1)}{SXR_2(t_2)}. \tag{3.13}$$

For practical purposes, the numerically determined $T_e(R)$ function is fitted by the following analytical formula:

$$T_e(R) = \mathrm{e}^{a_0 + a_1 \ln R + a_2 \ln^2 R + a_3 \ln^3 R}. \tag{3.14}$$

This approach is weakly sensitive to the radial profiles of density n_e and temperature. Therefore, an estimate of the T_e uncertainty is obtained by comparing the $T_e(R)$ determination with widely different n_e and T_e profiles assumptions: in the SXR model, extremely peaked or very flat profiles are assumed in order to determine the extreme fitted curves for $T_e(R)$. The estimated errors are of about 10% for the Be filters mounted in the MST and RFX-mod diagnostic for the typical temperature achieved in these experiments ($\approx 0.5 - 2$keV). An example of the $T_e(R)$ function for the multichord diagnostic installed in RFX-mod (see the following paragraph §3.4.1) is illustrated in Fig.3.7. The fitted curve corresponds to Be foil thickness of $t_1 = 51\mu$m and $t_2 = 104\mu$m.

T_e tomography

The "usual" two-foil technique based on the ratio of SXR brightness leads to systematic errors in the T_e calculation due to the uncertainties in the electron density and temperature profiles assumed for computing the $T_e(R)$ relation. This

error disappears if the ratio of two SXR emissivity distributions ε is considered. In this case, R can be calculated as $R(T_e) = \varepsilon(t_1)/\varepsilon(t_2)$. The corresponding $T_e(R)$ function can be always calculated with the model in Apx.C. It is easy to show that in order to increase the resolution in the T_e estimates one of the two foils should be at least two or three times thicker than the other one.

This modified version of two-foil technique allows for determining the 2D profile of the plasma electron temperature. If the SXR emissivity distribution is known in two different energy ranges (it could be either computed by a SXR model as in Apx.C or obtained by tomographic reconstructions), 2D information of T_e are obtainable and eventually localized thermal structures emerging in the plasma core can be detected. That is the first method which permits to have a map of this important plasma parameter over the whole plasma column, and not only a radial profile.

In this framework, the SXR tomography installed in the MST device played a fundamental role for the development of this technique (see §3.4.2).

3.4.1 RFX-mod diagnostics for T_e measurements

Two T_e diagnostics have been realized and installed in the RFX-mod device: an on-axis multifilter spectrometer and a multichord diagnostic.

The ***multifilter spectrometer*** [66] is composed of four different channels, each one with a different Be foil, so that the electron temperature can be determined directly by considering only two channels, or by a fit of all the available SXR signals [66]. The simultaneous availability of several filter thicknesses allowed to directly verify the assumption that particles have a Maxwellian distribution, so that the two-filter technique can be applied. In Fig.3.8 the amplitude of the four available signals is plotted on a logarithmic scale versus the cut-off energy of the filters: the data are well described by an exponential law (a straight line in semi-log scale). A schematic view of the diagnostic is displayed in Fig.3.9(a), together with the cross

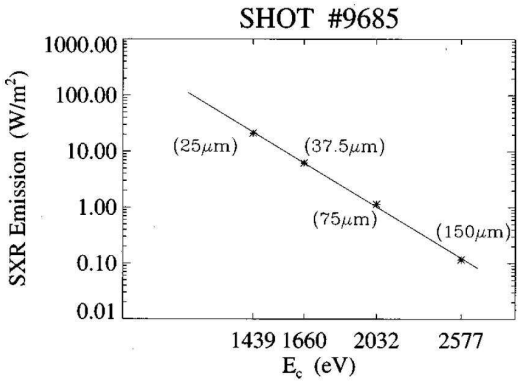

Figure 3.8: *Logarithmic plot of the four signals of the SXR spectrometer vs the cut-off energy of the beryllium filters [66].*

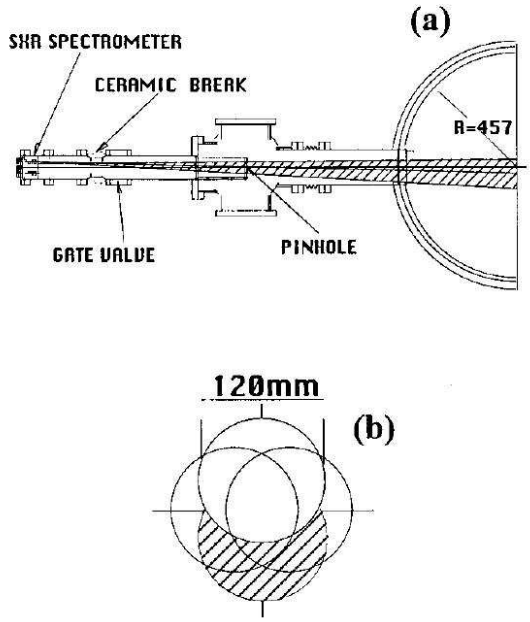

Figure 3.9: *(a) Experimental setup of the SXR spectrometer and (b) cross section of the viewing cones at the plasma center ($r = 0$) [66].*

section (b) of the viewing cones at the plasma center ($r = 0$). A suitable diaphragm serving as pinhole prevents the target emission from the porthole entrance to reach the detectors. The present version of the camera houses four ion implanted silicon diodes, which are covered with four beryllium absorbers (nowadays, the used thickness are 43, 78, 102 and 146μm). The basic reasons behind this choice were the typical values of the electron temperature (about 500eV at 1MA of I_p), and the first wall material, graphite, which makes carbon and oxygen the main impurities affecting the plasma [67]. The current generated by the diodes is amplified using transimpedances of $10^7, 10^8$ and 10^9 V/A. All the detectors collect radiation from the central region of the plasma, as shown in Fig.3.9(b) together with the sections of the viewing cones at the center of the vacuum vessel. The four channels do not overlap exactly: this leads to a systematic error when poloidally localized region of higher temperatures are present, such in QSH states. In this case, different couples of filters lead to significantly different estimates of the maximum electron temperature. In this case, the best T_e estimation is the one obtained using the two signals whose area of observation in Fig.3.9(b) lies in the equatorial plane, so that poloidal SXR asymmetries can be detected mostly in the same way, and the brightness ratio R is not affected by geometrical systematic errors.

The main causes of systematic error in this version of the instrumentation are the uncertainties in the thickness of the active volume of the diodes and of the Be filters, and the error in the determination of the gain of the amplifiers. Careful analysis led to a total assessment of T_e with an error which is less than 8% for T_e

of about 400eV [66].

The ***multichord diagnostic*** [68] is installed in a fixed position on a 100mm external-upper vertical porthole, directly connected to RFX-mod main vacuum through an UHV flange. The camera is composed by a cylindrical, 90mm-diameter stainless steel head, equipped with silicon detectors. A cooling system inside the head has been implemented: water can flow in a special circuit to assure to the head a controlled steady temperature, selectable in the range of $8 \div 90°C$. A graphite shield is mounted on the frontal plate of the head in order to protect the detectors from interactions with plasma. The photodiodes are custom made ion-implanted silicon detectors, mounted on ceramic carriers, with an active area of $5 \times 2.6mm^2$. The active thickness of $300\mu m$ can be fully exploited when detectors are used in total depletion mode with a bias of 28V. The geometrical constraints of the access did not allow for installing more than 20 diodes, mounted into two different rows. A picture illustrating the internal head is displayed in Fig.3.10: the two rows are marked by colored arrows, A and B. In each row, the diodes are gathered in two groups, for a total of four groups of five detectors. Each group looks at the plasma through a $1 \times 1mm^2$ pinhole. A representation of the geometry of the detection system is displayed in Fig.3.11(a): each line actually corresponds to the superposition of two lines of sight associated with two closest diodes belonging to the two different rows. An example of the projection on the poloidal section of the cone of observation is shadowed in Fig.3.11(a), while the blue chord is the corresponding line of sight. The cones of neighboring detectors do not overlap in the poloidal direction. In Fig.3.11(b), the toroidal view associated with the line of sight (blue line in Fig.3.11(a)) is displayed: the two diodes and pinholes lying in the two rows define two cones overlapping toroidally for about 70% of the total volume (the highlighted grey region). This assures that each pair of detectors covers the same plasma region.

Figure 3.10: *Picture of the SXR multichord photocamera. The 20 silicon diodes are gathered into four groups, and lie in two different rows, marked by the A and B colored arrows.*

To select only the plasma emissivity in a specific spectral range, beryllium filters are mounted between the plasma and the detectors, in the pinholes. Five diodes of row A look at the plasma through a flat Be filter of $47\mu m$, while the corresponding detectors of row B are equipped with Be foil of $96\mu m$: these five pairs of photodiodes define the five central chords displayed in Fig.3.11(a). Similarly,

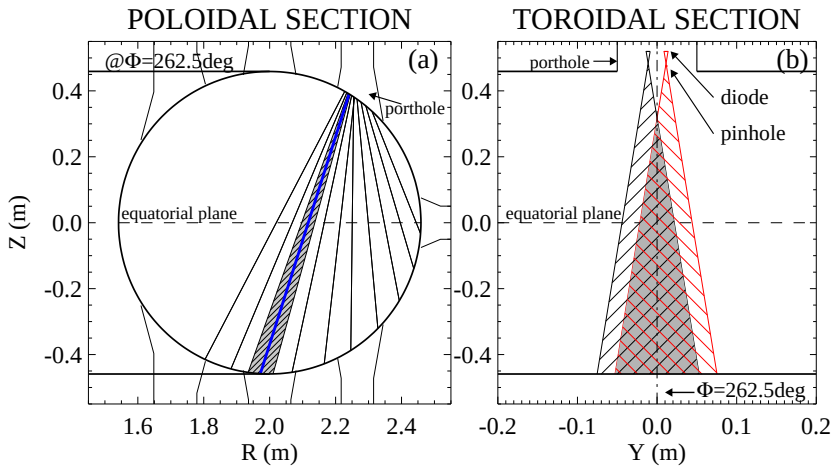

Figure 3.11: *(a) Geometric features of the ten pairs of lines of sight in the poloidal section: the grey region corresponds to the projection on this poloidal section of the cone of sight corresponding to the blue chord. (b) An overview in the toroidal section of the two overlapping cones of sight coupled together for the estimation of T_e, corresponding to the blue line of sight in (a).*

the remaining five diodes of row A have a 36μm filter, and the corresponding five detectors belonging to row B look at the plasma through a 72μm Be foil: these five pairs of lines of sight identify the five external chords (towards the low field side) illustrated in Fig.3.11(a). The two different pairs of filters allow for detecting SXR fluxes not only in the plasma core but also in the edge region, characterized by lower emissivity and higher T_e gradients. The cutoff energies corresponding to the installed foil thickness are between 1 and 1.8keV. The current generated in the detectors (of the order of nanoamperes) is received and processed by analog electronic, located in a cubicle close to the machine. The electronic system is similar to the one used in the SXR tomographic diagnostic (see §3.3.2 for details).

There are several sources of errors affecting these measurements [68], even if the uncertainties in the Be foil thickness remain the main cause of systematic error. The filters have been measured experimentally with an error of $\pm 1\mu$m; this causes a relative error on the estimated temperature less than about 10%.

3.4.2 MST SXR tomography for T_e estimation

The high flexibility of the MST SXR tomographic diagnostic (Sect.§3.3.3) and the possibility of easily removing the probes allow for using it in various configuration settings. The most common and exploited one is the so-called *normal* configuration: all the Be foils mounted on the four probes have the same thin thickness ($\approx 15\mu$m), permitting to apply the tomographic algorithms for the plasma SXR emissivity reconstructions, with a temporal resolution dictated by the bandwidth of the electronic system [69].

In order to estimate the electron temperature T_e, different configurations have been used. In temporal sequence, the first was the one based on mounting Be foils with different thickness simultaneously on the four probes, to provide information on the SXR emissivity distribution in different energy ranges. This is what we call "***multicolor***" configuration. If appropriate thicknesses are selected, the contribution of impurity radiation lines is greatly reduced, and only bremsstrahlung is considered. Since the tomographic algorithms cannot be applied in this configuration, a SXR emissivity model (Apx.C) can be used to reproduce the experimental SXR data. In this way, the density and electron temperature profiles have to be inserted in the SXR brightness calculation, so that the T_e profile can be derived indirectly. Analyses and results obtained with this configuration are reported in Ch.5.

A further configuration for the plasma temperature estimate has been exploited: the "***two-color configuration***", based on the two-foil technique. In this case, the two-foil algorithms have not been applied to SXR brightnesses, but directly to the SXR plasma emissivity obtained from tomographic reconstructions. That is achieved by using two pairs of Be foil thicknesses: a thinner thickness installed in the probes SXR1 and SXR2 (303μm) allows for plasma emissivity reconstructions in a SXR energy range wider than the one obtained with thicker Be foils which are installed in SXR3 and SXR4 (761μm). Thus the ratio between the two reconstructed emissivities provides a map of T_e, with the temporal accuracy typical of the SXR measurements (up to tenths of kHz). Further details are reported in Ch.5.

CHAPTER 4

SXR measurements of QSH states in RFX-mod

QSH is considered a key experimental finding [70] that suggests the possibility of obtaining the theoretically predicted single helicity (SH) in RFP devices. In QSH, magnetic chaos is in fact reduced, retaining all the positive features of the RFP configuration without the problems connected with the magnetic turbulence typical of the MH scenario. Experimentally, a residual level of secondary magnetic $m = 1$ modes is present, preventing at the moment the achievement of pure SH spectra and of the global high performance predicted for SH. SXR measurements and results presented in this chapter provide a wide description of QSH regimes in RFX-mod. The analysis reported here is not exhaustive of QSH regime, as this is currently work in progress. The purpose of this chapter is to show how SXR diagnostics allowed to better understand the QSH regime.

This chapter is organized in three main sections:

- In the first section, the QSH regime as it appears in various RFX-mod operations and how it is detected by SXR measurements is reported (§4.1).

- The SXR characterization of QSH structures is illustrated in the central section (§4.2). Attention has been focused on OPCD plasmas, because in this operation the best plasma results have been obtained.

- A QSH thermal characterization and the attempts of interpretation in high current OPCD plasmas have been reported in §4.4.

4.1 QSH states in RFX-mod

In experimental QSH states, a magnetic coherent helical structure is present in the plasma core, corresponding to the dominant magnetic mode [71]. This structure is composed by closed flux surfaces, so that pressure and confinement within the island are higher than in the plasma nearby. The Hamiltonian guiding center code, ORBIT [43], allowed for a comparison of the transport properties of SH and QSH states with those of MH states, predicting a reduction of particle diffusion in SH by two orders of magnitude with respect to MH. In QSH, a strong improvement of the particle confinement is found only within the helical structure, in agreement with the experimental observation of good flux surfaces present within the helical domain only. Experimental and numerical data both indicate that QSH states are associated with a local improvement of core plasma confinement; furthermore the results presented in this chapter suggest also a global improvement as the QSH is optimized. Residual magnetic chaos produced by the secondary modes limits the chaos reduction only in the interior of the helical structure, which corresponds to 10% of the plasma volume in present experiments. Even if the transition process to SH is presently not complete, it represents nonetheless an indication of the existence of a spontaneous positive self-organization in the path towards monochromatic SH states. More and more efforts aiming at producing stationary SH RFP plasmas are being performed in order to investigate the possibility of using the RFP configuration for the realization of an economic fusion energy source.

Two are the main guidelines followed: the possibility to drive plasma towards a QSH state by means of external circuits controlling, creating or reducing edge radial magnetic fields, and the control of the current density profile. The former aims at producing dynamo in QSH state in magnetic chaos-free environment, thanks to the active control system [48, 51] on the RFX-mod device. The latter is based on an oscillation in the toroidal external applied field that induces an electric field replacing the dynamo field. This is the so-called *Oscillating Poloidal Current Drive* operation (OPCD) [55, 56], which leads to a reduction of the tearing mode amplitudes.

4.1.1 Magnetic and SXR evidences of QSH states

Non-Virtual Shell and Virtual Shell operation

The RFX-mod device has been equipped with an electromagnetic front-end, plus magnetic coil diagnostics (Sect.§2.4.1 for details).

The main application of the active coil system has been the so-called *Virtual Shell* (VS) scenario [72]: the coils react to edge magnetic perturbations in order to cancel the edge radial magnetic field, so as to mimic the effect of a perfectly conducting shell. With VS, the expected strong reduction of b_r (the radial magnetic field measured at the plasma edge) has been observed with respect to the case without VS [72]. In Fig.4.1 the radial magnetic field components for a VS discharge

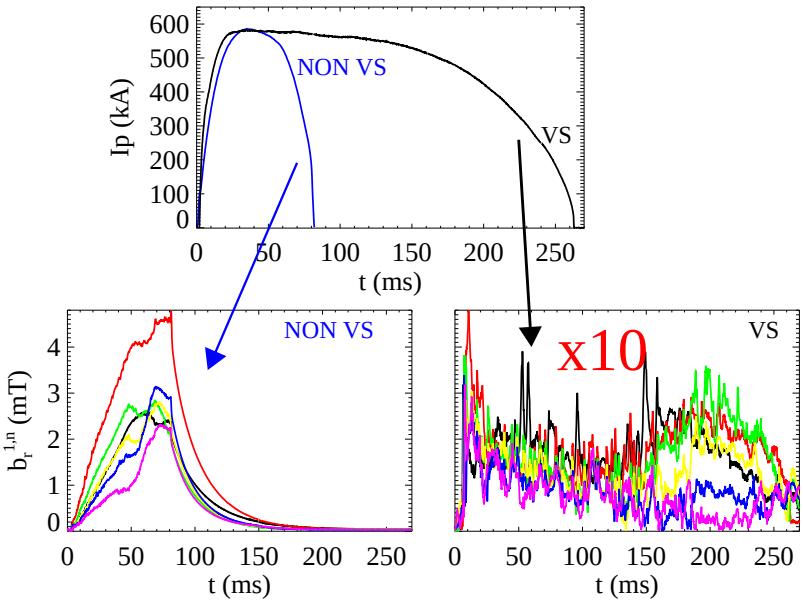

Figure 4.1: *Plasma current I_p and the radial magnetic fluctuation b_r measured at the plasma edge for a NON-VS and a VS discharges.*

and non-VS are displayed: the amplitude values b_r are greatly decreased in the VS operations than in the non-VS ones. But this is not the only beneficial effect: also the plasma bulging, which is produced by the phase and wall-locking of the dynamo modes, decreases. Consequently, the outcome of the VS is a much smoother magnetic boundary, which leads to reduced heat and particle flux on the first wall. Thus, in VS the discharge can be sustained for longer time.

In the non-VS discharges, magnetic QSH are present with the $m = 1, n = -8$ tearing mode mostly dominating the spectrum (Fig.4.1), even if sometimes $n = -7$ or $n = -9$ could appear. Corresponding to such magnetic spectrum, SXR emissivity shows the presence of a localized more emissive structure, intermittently appearing in the plasma core, in the radial and poloidal position

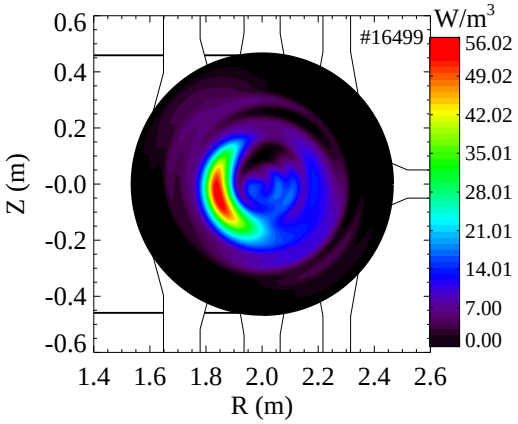

Figure 4.2: *SXR emissivity reconstruction of a QSH state in a NON-VS plasma (#16499, $t = 71.01$ms).*

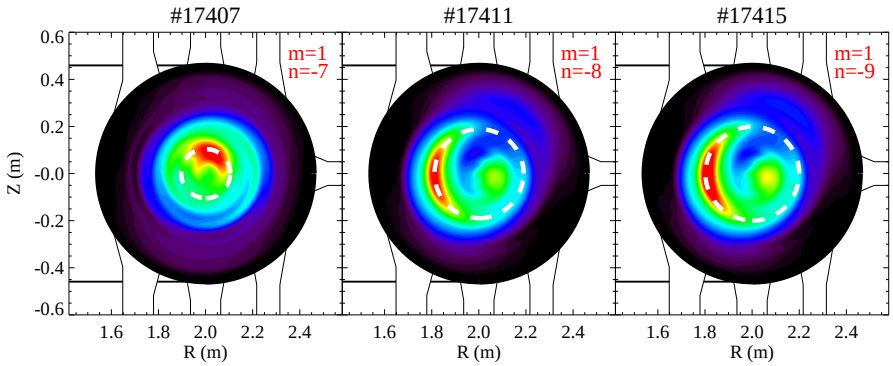

Figure 4.3: *SXR reconstructions of a $m = 1$ structure naturally evolving in the plasma core during VS operation for (a) $n_0 = -7$, (b) $n_0 = -8$ and (c) $n_0 = -9$, respectively. Each corresponding resonant surface is superimposed with a white dashed circle.*

corresponding to the magnetic island (Fig.4.2). These structures were also detected in RFX [71]. In VS operation, QSH spectra are present too, but the increased shell proximity of RFX-mod and the external saddle coil system make the edge radial field amplitudes of the secondary modes lower than in non-VS.

It has been found that modifying the VS feedback laws in order to let a single $m = 1$ mode free to evolve, QSH spectra are obtained more often, but with shorter pulse duration. In correspondence of these induced QSH magnetic spectra, a SXR structure appears and evolves in the plasma column. Different $m = 1, n_0$ instabilities can be left uncontrolled: the $n_0 = -7$ (which is the innermost resonant mode in the RFX-mod magnetic configuration), the $n_0 = -8$ and $n_0 = -9$ give evidences of more emissive SXR structures in the reconstructed emissivity distribution. Also the growth of higher n modes can be allowed by the coil system, but no evidences of SXR structures have been found, as their resonance surfaces are radially too close to the reversal surface, where the SXR emissivity is very low and the magnetic islands are too close each other. The SXR structures revealed for $-9 \leq n_0 \leq -7$ in QSH states are located (radially and poloidally) at the position of their corresponding magnetic island. In Fig.4.3 three examples of SXR structures naturally evolved in the plasma column are illustrated, for $n_0 = -7$, $n_0 = -8$ and $n_0 = -9$, respectively. The white dashed circles superimposed to the reconstructions represent the position of the resonance surface for that island calculated with the $\mu\&p$ model [33].

QSH in VS: intermittency and stationarity

QSH time evolutions in VS operation can be grouped in two main categories: intermittent and quasi-stationary QSH. *Intermittent* QSH states are a new feature of the RFX-mod device: they are characterized by quasi-periodic phases where

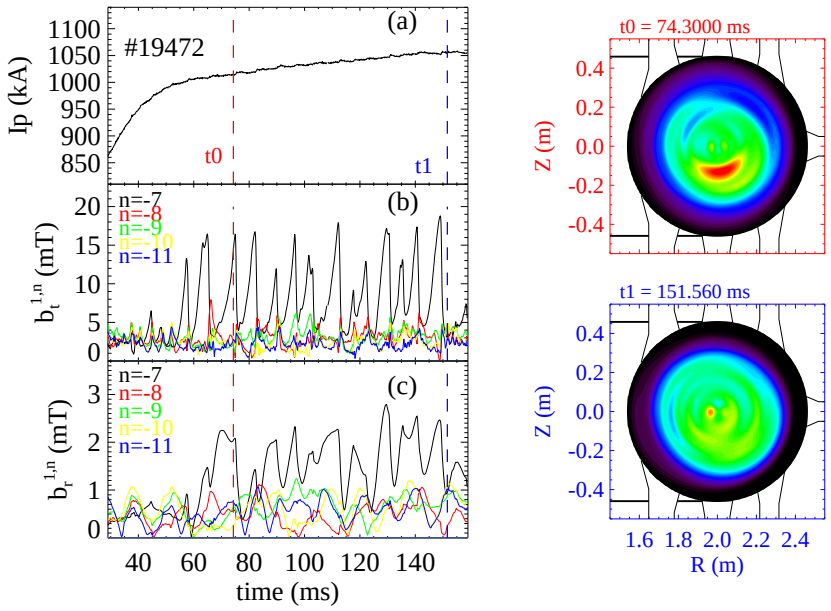

Figure 4.4: *Example of (a) plasma current, (b) toroidal b_t and (c) radial b_r magnetic fluctuations for an intermittent QSH state in the VS operation: the SXR structure appears and disappears, following the $b^{1,-7}$ intermittent dynamic both in the toroidal b_t and radial b_r components. SXR emissivity reconstructions at different times (t_0 and t_1) confirm the appearance and disappearance of a localized more emissive region following the QSH cycle.*

the dominant mode increases and the secondary ones decrease. In *quasi-stationary* cases, instead, a dominant $m = 1$ helicity persists for long time, on average for the whole plasma flat-top (observed at higher plasma currents, $I_p > 0.9MA$), together with a dynamic evolution characterized by some QSH interruptions.

Intermittent QSH is reminiscent of a similar phenomenology observed in other experiments, like in MST [73], where the QSH regime is very often found between sawtooth crashes. After a crash, only one $m = 1$ mode starts to increase, while the secondary ones remains at lower values; the dominant instability increases until the following F crash happens. At that time, the dominant mode increase is suddenly interrupted and then another cycle starts again. In Fig.4.4 an intermittent QSH case for RFX-mod is illustrated: the magnetic mode amplitudes reveal the presence of a dominant $m = 1, n = -7$ mode growing up to its maximum and then crashing for starting again another cycle as determined by the F parameter. SXR reconstructions at two different times are illustrated: one highlights the presence of a localized more emissive region during the QSH period (t_0); the other one instead has a symmetric emissive profile in MH regime (t_1). In Fig.4.5 the quasi-stationary QSH type is illustrated, with the (1,-7) magnetic mode dominating the magnetic spectrum for a long period (two examples of SXR structure reconstructions are

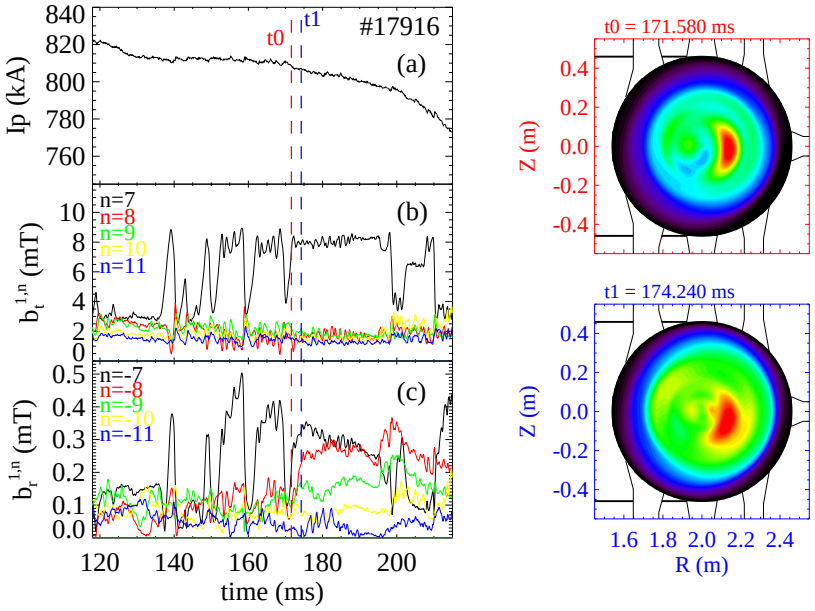

Figure 4.5: *Example of (a) plasma current, (b) toroidal b_t and (c) radial b_r magnetic field in a quasi-stationary QSH state in the VS operation: the SXR structure remains for a long period in which the $b^{1,-7}$ mode dominates the magnetic $m = 1$ spectrum. SXR emissivity reconstructions at two different times (t_0 and t_1) confirm the presence of a localized more emissive region during the whole QSH period.*

displayed too, showing a more emissive region persisting during the whole QSH period). Both intermittent and quasi-stationary QSH are characterized by a similar level of average secondary modes and by the helical symmetry of the plasma core [70].

QSH rotation: external references, rotating perturbations and complex gains

The external coil system can be used not only for inducing QSH structures, but also for setting the island position: in particular, the phase can be varied during the discharge, so that a rotation can be obtained. This was obtained by modifying the VS feedback law in order to follow a reference amplitude and phase for a selected mode. Experiments with a reference on a single mode were successful at controlling the phase but QSH occurrence was not significantly modified. Results of this method are displayed in Fig.4.6: the more emissive region is rotating at the velocity of the magnetic instability induced, along the black circle which represent the resonant surface for that instability.

The external phase and amplitude mode references have been applied also for forcing the QSH structure to be positioned in particular location. For example, considering the laser direction of the Thomson scattering (TS) diagnostic and the limited vessel coverage of the multichord diagnostic for T_e determination, it is

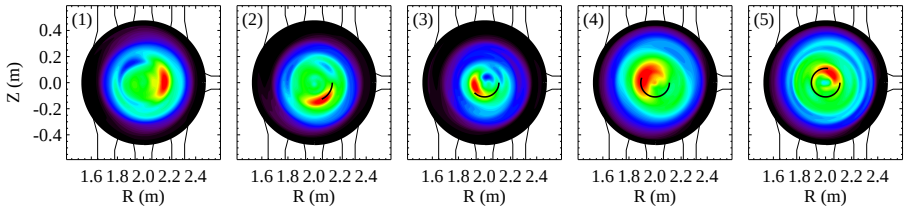

Figure 4.6: *SXR reconstructions for a QSH structure with an external rotation reference. The black line represents the O-point of the magnetic island rotating along the corresponding resonant surface.*

possible to make the island rotate at the frequency rate of the TS laser so that at each laser shot ($\approx$ 25Hz) the island is located in the vessel equatorial plane so to be detected by TS at exactly the same poloidal position. A different aim could be instead of making the island be positioned at a slightly different poloidal position at each laser shot, in order to obtain a scan of the radial island characterization. This is ongoing work: this technique is in fact one of the main goal of the 2008 RFX-mod program.

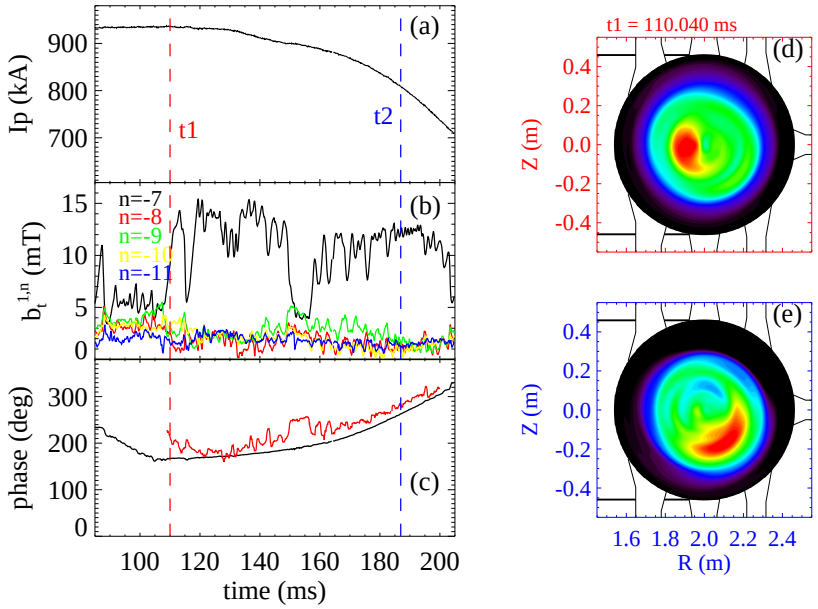

Figure 4.7: *(a) Plasma current and (b) toroidal magnetic field b_t for a complex-gain VS discharge. (c) The magnetic phase (black line) of the dominant mode as realized by complex gains at the tomography section; the center of mass of the SXR reconstructed emissivity (red line) is superimposed. SXR tomographic reconstructions (d) and (e) at two different times show the different position of the SXR structure due to the applied mode rotation.*

The same rotating reference technique has been applied to several modes simultaneously, in order to drag the slinky deformation due to mode locking. Slinky rotation were systematically obtained, allowing experiments at $Ip \lesssim 1.2$MA, but QSH transition never occurred.

A different effort has been to use *complex gains*, applying the regulators to the modes rather than to the individual sensors, pre-setting a complex gain to each mode, i.e. the feedback system applies an out-of-phase cancelation of the mode. That induces a rotation of the mode dominating the $m = 1$ spectrum [49]. In Fig.4.7 an example is displayed, with the plasma current (a) and the toroidal magnetic fluctuations (b). The phase referring to the $m = 1, n = -7$ calculated at the tomography section for complex-gain operation is displayed in (c) with black line, and two emissivity reconstructions [(e) and (f)] at two different times confirm the effective rotation of the structure. The SXR emissivity center of mass calculated from the reconstructions can be identified with the island O-point (i.e. the topological center of the structure), being the SXR structure associated to the magnetic island. The center of mass is superimposed to the magnetic phase in Fig4.7(c) with a red line: the correspondence between them confirms the reliability of this method for QSH rotation, even if in some cases the differences between the magnetic phase and the one coming from SXR measurements could reach 30-40 degrees. Such disagreement led to the discovery of a systematic error in the magnetic field measurements, due to the sidebands aliasing as described in the next paragraph.

SXR measurements: from VS to CMC operation

As highlighted in the previous paragraphs, SXR tomography plays a fundamental role in investigating the QSH structure dynamics, as well as for investigating the plasma column displacement in all the operational configuration. In particular, if the QSH state is externally stimulated with the MHD active control system, tomography can be used for checking the accuracy of the saddle coil operation. Let us consider the case in which the saddle coils are used to produce helical fields, following a reference input in amplitude and phase, and thus leading to a QSH regime. In such QSH configuration, the center of mass should perfectly agree with the position of the magnetic island forced by the external system. However, detailed analysis on the comparison between the SXR center of mass position and the poloidal magnetic island location at the tomography toroidal section highlighted a non-negligible systematic mismatch, larger up to 30-40 degrees. The mismatch was identified also for QSH appearing spontaneously in the plasma column, but it was evident in particular in QSH plasmas induced by the MHD active coil system. The high reliability of the information from the SXR reconstructions suggested for investigating deeply the reason of this mismatch, which was identified in a systematic error in magnetic measurements due to the aliasing of the sidebands generated by the saddle coils [50]. An example is displayed in Fig.4.8. In panel (a) the $m = 1$ temporal evolution of the toroidal magnetic fluctuation b_t is displayed, while in (b) the corresponding phase of the perturbations calculated at the tomographic diag-

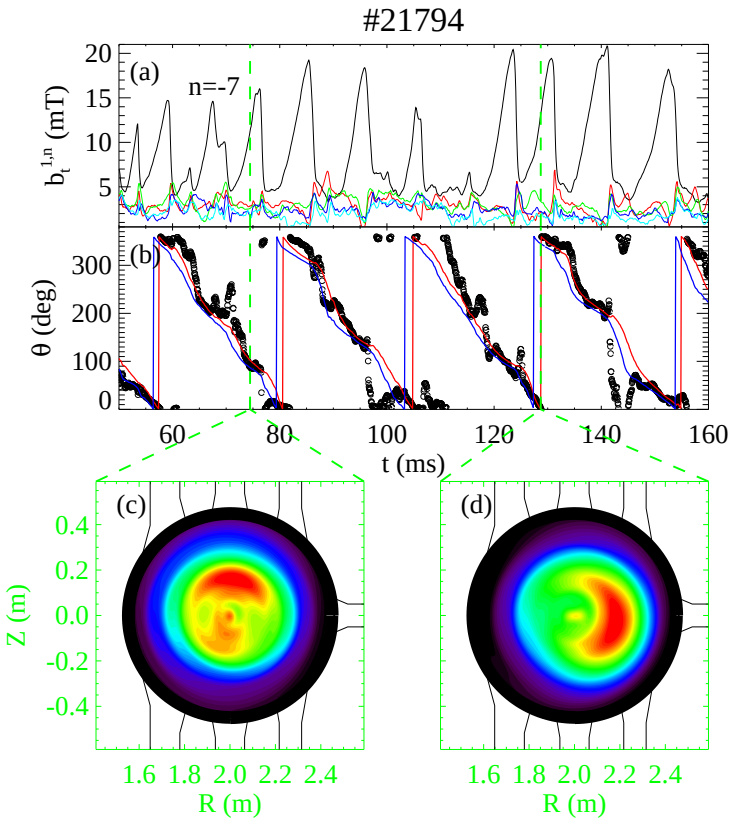

Figure 4.8: *(a) Temporal evolution of the magnetic perturbation $b_t^{1,n}$, for $-11 \leq n \leq -7$. (b) The magnetic phase of the dominant $b_t^{1,-7}$ at the tomographic section, for magnetic measurements affected by aliasing (blue line) and after correction (red line). The poloidal position of the SXR center of mass is superimposed (empty circles). (c) and (d) SXR tomographic reconstructions highlighting a more emissive region, at the two time instants reported as dashed lines in (a) and (b).*

nostic cross-section, together with the location of the SXR center of mass (empty circles), is reported. The blue line in (b) represents the magnetic phase with the aliasing, while the red one corresponds to the magnetic island location cleaned from the aliasing. A very good agreement for the cleaned (m=1,n=-7) phase with the poloidal position of the SXR structure is found when the QSH regime is robust.

When all the $m = 1$ perturbations have similar amplitudes (MH state), the magnetic islands are all comparable in amplitudes and they are overlapping so that no structures emerge in the plasma core. In this case, the SXR center of mass does not correspond to the SXR island O-point, but it should correspond to the plasma column axis lying in the equatorial plane, at $\theta = 0$. In MH states, the SXR center of mass of Fig.4.8 in fact goes to $\theta = 0$, even if sometimes a small localized structure seems to survive so that the center of mass remains in proximity of the location of the $m = 1, n = -7$ mode.

Two SXR reconstructions in QSH period are illustrated in Fig.4.8(c) and (d): a localized SXR structure is evident, positioned at the location corresponding to the magnetic mode rotation. The corrections of the Fourier aliasing have also been implemented in the real time algorithms and have led to the concept of Clean Mode Control (CMC) operation [50, 51].

4.1.2 SXR island characterization

The high spatial resolution of the SXR tomography allows for investigating in details the main features of the plasma column. The angular Fourier decomposition of the SXR brightness allows for reconstructing not only the symmetric shape of the plasma column ($m = 0$), but also the SXR structures appearing in the plasma core during QSH states with higher harmonics (see for details Apx.A). The SXR island shape is mainly determined by the $m = 1$ and $m = 2$ harmonics: using the line passing through the center of the vessel (which corresponds approximately to the plasma magnetic axis, neglecting the horizontal Shafranov shift, estimated to be of a few centimeters) and the island O-point, it is possible to define the island *radial width* w_{SXR} as the FWHM of the sum of the first two harmonics. Considering that the $m = 2$ harmonics have a small effect on the structure shape, it is possible to simplify the calculation considering the FWHM of the $m = 1$ only. Examples of the SXR island width w_{SXR} for different discharge operations are reported in Fig.4.9(a), where VS cases with the cleaned sidebands are represented by stars, and CMC by empty circles. Different plasma equilibria have been considered: deep F discharges (F$\approx -0.07 \div -0.1$) are in black, while shallow ones (F $\approx -0.01 \div -0.02$) in red. Here, only pure VS and pure CMC shots have been investigated, that means only spontaneous QSH structures have been considered (a total of 5 shots for each operation). The radial width w_{SXR} may vary considerably: from about 6cm at the deepest F values up to about 25cm at the shallowest ones. This is a consequence of the plasma equilibrium and of the q profile: deepest F values imply a deepest

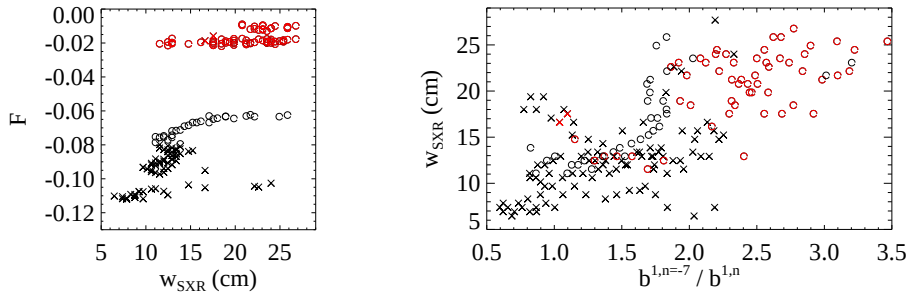

Figure 4.9: *(a) SXR island width w_{SXR} at different plasma equilibria and (b) as function of the ratio between the dominant mode and the secondary ones, $b_{1,-7}/b_{1,n}$, for VS (stars) and CMC (empty circles) discharges.*

$q(a)$ at the plasma edge, with higher gradients in the region of the tearing mode resonance, which is in proximity of the core of the plasma column. Steepest q gradients mean that the resonant surfaces for the tearing modes are radially closer than at flatter gradients. So magnetic islands for deep F values are closer, and their overlapping does not allow a significant growth of the structure, because of the chaos generated by the contiguous $m = 1$ modes. As a consequence, the SXR structures detected are in general radially smaller for deep F discharges than for the shallower ones. Then, considering the toroidal magnetic mode amplitudes b_t and the ratio between the dominant mode $b_t^{1,-7}$ and the secondary ones $b_t^{1,n}$ (being $b_t^{1,n} = \sqrt{\sum_{i=-15}^{-8}(b_t^{1,i})^2}$), w_{SXR} is larger for purer QSH, that is for larger values of $b_t^{1,-7}$ at same values of secondary amplitudes, as illustrated in Fig.4.9(b).

SXR structures and thermal islands

A more complete survey on SXR structures is given by the information coming from the Thomson Scattering (TS) diagnostic installed in RFX-mod [74]. This diagnostic provides the radial electron temperature profile in 84 spatial points along the horizontal mid-plane, with a time resolution of 25ms (corresponding to approx-

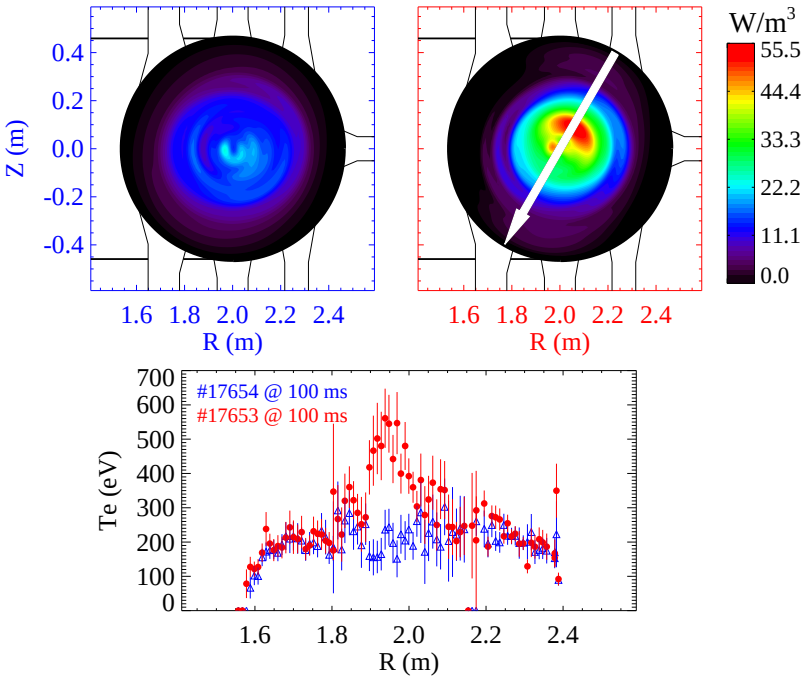

Figure 4.10: *SXR reconstructions and T_e profiles from TS diagnostic for an MH state (blue colors) and a QSH one (red colors). In MH, the T_e profile is completely flat in the plasma core, while the gradients are limited to a narrow region in the plasma edge. In QSH, a thermal hotter region in correspondence of the SXR structure is evident.*

imately ten profiles per discharge). The TS diagnostic and the SXR tomography are located in different toroidal position of the RFX-mod vessel: nonetheless, information from TS can be reported to the tomography cross-section by considering the toroidal periodicity of the plasma and of the magnetic instabilities.

In QSH regimes, if the magnetic island is positioned at a favorable poloidal location for the TS diagnostic, the temperature T_e profile is characterized by a hotter localized region, corresponding exactly to the position of the magnetic island. Taking into account the helical geometry of the structure and the toroidal distance between the diagnostics, the position of the localized T_e enhancement closely corresponds to the SXR more emissive region in the reconstructed tomograms. In Fig.4.10, the SXR reconstructions for a MH state (blue panel) and for a QSH (red panel) are illustrated. The T_e profiles measured by the TS diagnostic [75] for both MH (blue circles) and QSH (red circles) states represent the T_e variation along the diameter shown by the white arrow in the tomographic poloidal section. In MH, T_e is characterized by a flat profile, except for the gradients in proximity of the plasma edge ($\geq$ 2.4m and $\leq$ 1.65m). In QSH, over the central flat T_e region, a localized T_e structure is present, and as a consequence the SXR emissivity distribution has a more emissive localized region. The T_e flat profile around the island suggests that in the plasma core the electron energy transport coefficient is high. On the other hand, steep gradients at the island edge indicate that transport is reduced in that region. Despite this transport improvement, the island volume is rather small so that the effect on global confinement is limited. But if the volume increases and the island becomes larger and larger up to cover the all entire plasma core, a global enhanced confinement of the entire plasma could be expected.

4.2 SXR structures in OPCD operation

A different way to induce QSH regimes in RFX-mod plasmas is to reduce magnetic fluctuations by means of the *Oscillating Poloidal Current Drive* (OPCD) [55]. It was already known that OPCD was favoring the onset of QSH in RFX. In RFX-mod, OPCD is the most effective technique to systematically obtain QSH regimes [56]. OPCD operation is applied in RFX-mod together with VS, in order to further reduce and control the mode amplitudes at the plasma boundary: now the reduction of the magnetic fluctuation level is systematically obtained, together with the formation of a QSH state. At the same time, a global increase of the electron temperature and a reduction of the electron energy transport are obtained [56]. In the co-dynamo phase (that lasts as long as the electric field at the edge remains positive), the innermost resonant harmonic amplitude measured at the plasma edge increases while the secondary modes decrease significantly, resulting in a QSH spectrum. In spontaneous QSH observed in non OPCD discharges, such a decrease of the secondary modes is not observed. Moreover, in the phase of reduced internal chaos, an increase in the electron temperature measured by the on-axis double filter diagnostic described in 3.4.1 is observed.

The correlation of the OPCD effects on QSH and plasma temperatures are summarized in Fig.4.11, where each point corresponds to the maximum of the OPCD cycle effect: more than 90% of the highest temperatures are reached during QSH discharges [56]. OPCD produces a dominant mode which tends to be higher as the secondary are reduced, therefore OPCD stimulates systematically the onset of QSH states.

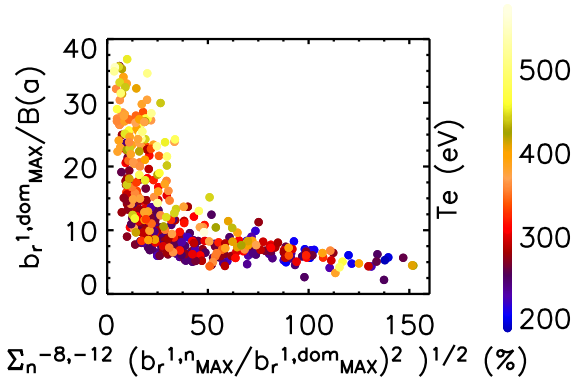

Figure 4.11: *T_e as function of the normalized amplitude of the dominant mode $b_r^{1,dom}$ and the secondary modes $b_r^{1,n}$. Each T_e value has been calculated at the maximum amplitude of the mode dominating the $m = 1$ QSH spectrum during a OPCD cycle (data from [56]).*

During QSH induced by OPCD in the co-dynamo phase, a localized more emissive SXR region arises in the plasma core. This structure is well correlated with the magnetic QSH that is observed and is also representative of a thermal structure. In Fig.4.12(a), an example of a SXR structure during the OPCD cycle is displayed; reconstruction of a MH state during the anti-dynamo

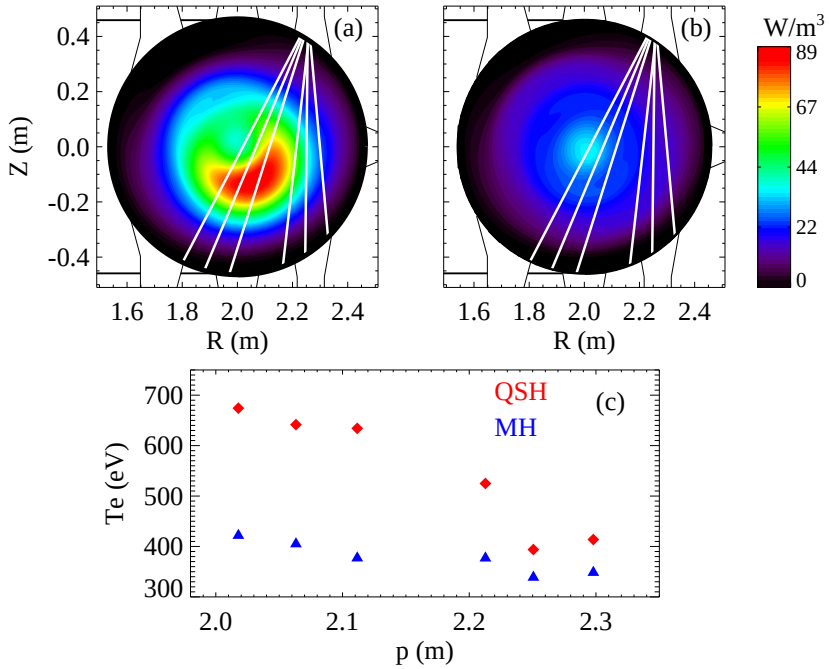

Figure 4.12: *SXR tomographic reconstructions in the QSH (a) and MH (b) phase of an OPCD ($I_p \sim 960kA$). (c) Temperature profiles obtained with the multichord diagnostic for the cases in (a) and (b) for the white lines of sight superimposed to the two reconstructions.*

OPCD period is displayed in Fig.4.12(b), where no localized structure is present and a symmetric profile is established. For these two reconstructions the corresponding T_e profiles measured with the multichord diagnostic are reported in panel (c), for the white lines of sight superimposed to the SXR reconstructions: the T_e increase involves mostly the plasma core ($2 < p < 2.16$m), where the SXR structure is formed and a ΔT_e (between the maximum T_e island value and that of the plasma background) of about 250eV is observed. This value, typical in the RFX-mod thermal structures during QSH, corresponds to the maximum T_e observed inside the island; the electron temperature of the plasma nearby ($p > 2.18$m), which is heated too, is higher in QSH, so that a global improvement of pressure in the entire plasma column is observed.

4.2.1 Island characterization in a OPCD cycle

The presence of a non-vanishing amplitude of secondary modes is believed to be responsible for intermittency in QSH states. In particular during a OPCD cycle, where the mode amplitude values are driven by the external field modification, it is possible to identify the intermittency of the QSH state strictly linked to the

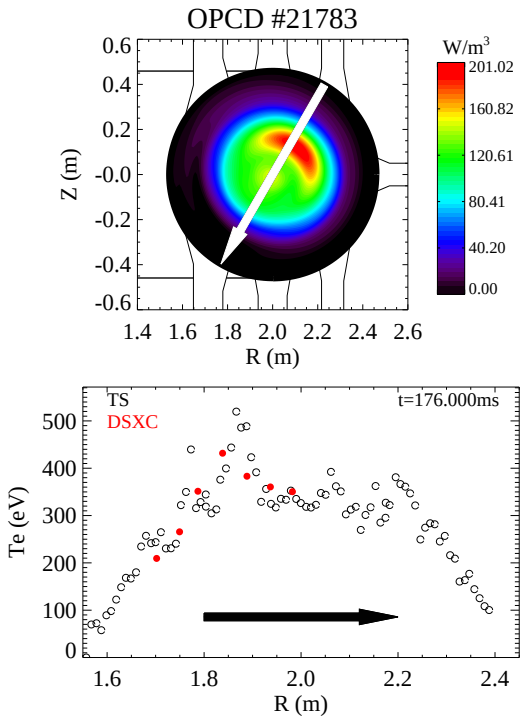

Figure 4.13: *Example of a OPCD QSH island in RFX-mod: the SXR reconstruction and the T_e profiles from the TS diagnostic (empty circles) and the multichord one (red full circles) calculated along the white arrow in the emissivity distribution are illustrated.*

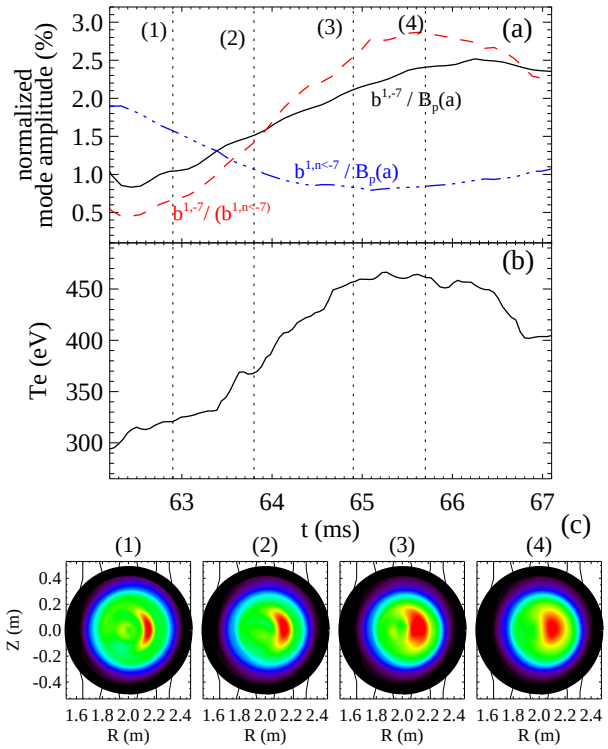

Figure 4.14: *Example of a single QSH-MH cycle during OPCD in RFX-mod: (a) temporal evolution of dominant (black) and secondary (blue) magnetic field fluctuations (toroidal component); the red curve is the ratio dominant/secondary fluctuations; (b) electron temperature, as measured by the on-axis multifilter diagnostic; (c) tomographic images corresponding to times (1)-(4) in panels (a) and (b).*

OPCD cycle phases (as reported in the previous paragraph). Hot islands appear and disappear in the core, according to a cycle where dominant and secondary modes have an opposite effect on the island width.

An example of SXR reconstruction during the maximum of a OPCD QSH is displayed in Fig.4.13(a). Panel (b) shows the corresponding T_e profiles (TS data is displayed with empty circles while multichord SXR ones with red circles). The region between 1.8 and 1.9m is characterized by an enhanced T_e in both diagnostics.

Let us consider a single OPCD cycle: how does the thermal structure evolves throughout the cycle? An example is shown in Fig.4.14: in frame (a), the increase of the dominant mode amplitude (the black curve represents the edge toroidal field fluctuation, $b_t^{1,-7}$, normalized to the equilibrium poloidal field at the edge $B_p(a)$) is evident. At the same time, the decrease of the normalized secondary modes (the blue curve, $b_t^{1,n<-7} = \sqrt{\sum_{n'=-15}^{-8}(b_t^{1,n'})^2}$ takes place. The ratio of the dominant to secondary modes (red curve) reproduces quite well the time trace of the electron temperature, as measured by the on-axis multifilter diagnostic (Fig.4.14(b)). This

is linked to the formation of a hot SXR island in the core of the plasma, whose width also increases proportionally to the ratio of the dominant to secondary mode amplitude. SXR tomograms with the localized structure evolution are displayed in Fig.4.14(c). The connection between heating of the island, mode amplitude and island width w_{SXR} defined in §4.1.2, is highlighted by plotting several indicators against each other in Fig.4.15. T_e is a decreasing function of the secondary mode amplitude: this means that a low level of secondary modes is beneficial for the warming up of the island. The role of the dominant mode is opposite: for example, the island width w_{SXR}, is a monotonically increasing function of the dominant mode amplitude [Fig.4.15(b)], which is a well-known result in linear theory. Finally, in Fig.4.15(c) electron temperature T_e is plotted as a function of the ratio $b_{1,-7}/b_{1,n<-7}$ between dominant and secondary modes. It is evident that temperature is proportional to this ratio, with a very good correlation ($R > 0.9$). The resulting picture is that dominant mode increases, secondary modes decrease, the island width increases, and the island warms up. Since all of these phenomena are correlated through MHD dynamics, it is difficult to infer a causality relation.

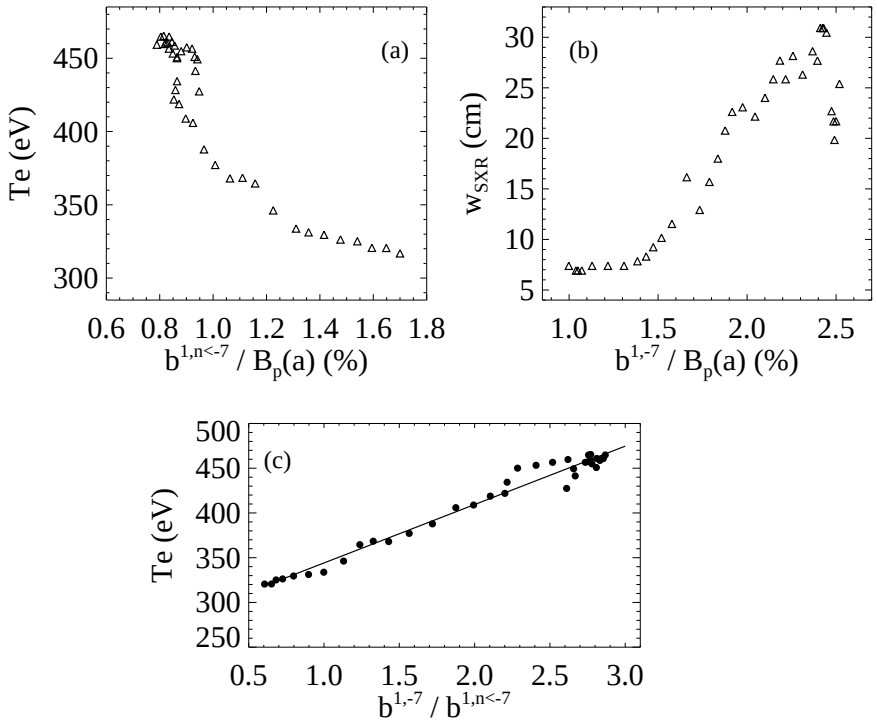

Figure 4.15: *(a) Electron temperature as a function of secondary mode amplitude; (b) island width w_{SXR} as a function of the dominant, $n = -7$ mode amplitude; (c) electron temperature as a function of the ratio between dominant and secondary modes. Data points are sampled during a single OPCD cycle (the same as in Fig.4.14).*

In linear theory the size of the island is a monotonically increasing function of the dominant mode amplitude; secondary modes act as a perturbation of the island, often determining a region of weakly chaotic lines which surround the magnetic island [76]. If the amplitude of the single helicity is large enough, the sensitivity of the system to the perturbing action of secondary modes (namely, with $n < -7$ in RFX-mod) becomes smaller. In this case, a radially wider structure corresponds to larger amplitudes of the dominant mode, in which the O-point is coming closer to the X-point, until this disappears. That corresponds to the so-called expulsion of the X-point (separatrix) associated to the magnetic island [77]. Experimentally, it is still not known whether the islands observed in RFX-mod correspond to a separatrix expulsion or not: there are some indications that well-formed $n = -7$ islands could correspond to a state without an X-point, where the island becomes the new helical equilibrium for the RFP configuration [78]; moreover, detailed studies in the MST experiment show that at high levels of the dominant $n = 6$ mode amplitude, the role of the $n = 7$ mode is negligible, suggesting the presence of a new equilibrium which is rather insensitive to the perturbation of the secondary modes [69]. A quantitative description of the relative importance (on the basis of numerical simulations) of the dominant and secondary modes on the thermal conductivity inside the island is still ongoing research.

A difficulty in analyzing data from RFX-mod is that the growth of the $n = -7$ mode and the decrease of the $n < -7$ are generally correlated through their MHD dynamics, so that it is not possible from the available data to ascertain their relative impact on the thermal properties of the island. A final remark regards the transient nature of QSH islands during OPCD. Due to limited time duration of OPCD, it is questionable whether a thermal equilibration of the island with the surrounding plasma is ever reached at all. Anyway, in Fig.4.14, it is evident that T_e is approximately constant from 65 to 66.5ms.

4.3 Transport reduction in QSH

An explanation of the strong heating observed in the core of a RFP during a QSH state has been given in Ref.[79]: inside the island, the heat transport coefficient $\chi_{E,e}$ is much smaller than in the surrounding chaotic sea, due to the formation of well defined magnetic surfaces, so that the magnetic chaos is no longer the mechanism responsible for transport, which can decrease to values comparable to the tokamak ones. To verify this picture and to calculate the value of $\chi_{E,e}$, the 2D code M1TeV [80, 81], which describes magnetic islands in tokamaks, has been adapted to the RFP configuration.

Let us first recall the basic properties of the magnetic field topology in QSH; M1TeV will use a geometry based on such properties. Given a QSH magnetic spectrum, Poincaré plots of magnetic field lines display a region of conserved flux surfaces, surrounded by a more chaotic region. It has been recently found that, if the dominant mode is sufficiently high (i.e. a wider island occurs), the transition

from the conserved region to magnetic chaos occurs more gradually. In particular, an intermediate region called *sticky* region appears around the island core: magnetic field lines are chaotic but they still fill in a bounded domain. These magnetic topology properties affect test particle transport: the loss time, i.e. the time required for a half population of particles to reach a defined loss surface, in the sticky region is in fact lower than in the island core, but higher than in the outer chaos. In Fig.4.16(a), a Poincarè plot of a QSH island for RFX-mod is shown: the conserved flux surfaces occupy the central region of the island and are surrounded by chaos. M1TeV uses a simpler parametrization of the flux surfaces corresponding to a single $m = 1$ mode (Fig.4.16(b)): within this parametrization, no sticky region appears, but it is possible to modulate the value of $\chi_{E,e}$ across the minor radius. The island last conserved flux surface is closed (the X-point is present), so that the core is visible and topologically separated from the plasma edge.

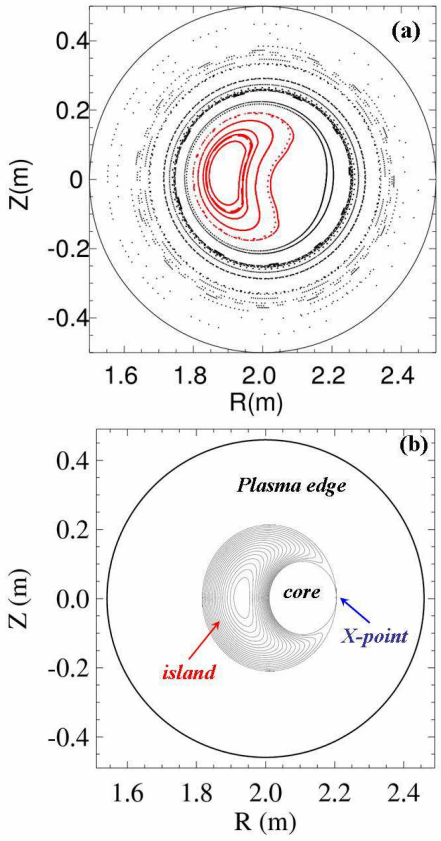

Figure 4.16: *(a) Poincarè plot of a magnetic island in RFX-mod by ORBIT code. (b) Section of magnetic surfaces inside the island as defined in M1TeV.*

M1TeV code for RFX-mod

Within the M1TeV approximation, the plasma core is divided into three parts: the island, where all the flux surfaces are conserved and closed, the plasma edge characterized by chaos, and the core (containing the former magnetic axis), which is separated from the edge by the X-point. It is possible to assign different values of $\chi_{E,e}$ to the three regions.

In order to focus on heat diffusion, the topology evolution of the island is kept constant in time, as we are interested in the diffusion process. The island is assumed to appear on a timescale much longer than diffusion. In fact, the transport time (0.5ms with $\chi = 10\mathrm{m}^2/s$) is much shorter than the resistive diffusion time (30ms at $\chi = 10\mathrm{m}^2/s$). In this way, the QSH phenomenology is simplified, separating the magnetic evolution (reconnection) of the island, and the heating process.

At the beginning of the simulation, a flat temperature profile is assumed, con-

sistently with experimental results from TS in MH regimes. The diffusion process within an island of a given topology is then computed according to the diffusion equation [79]. The source in the diffusion equation is given by the ohmic power inside the island. The chaotic region outside the island is simulated by assuming there that $\chi_{E,e} = 1000 m^2/s$, according to experimental results [82]. No matter what $\chi_{E,e}$ value is used, the simulation will give a negligible temperature gradient in the edge region. Different simulations are performed by varying the diffusion coefficients inside the island so that the difference in T_e between inside and outside the island matches the experimental values.

As experimentally X-point are rarely seen (Fig.4.16(a)), some residual chaos is likely to exist also in the island, near the separatrix. This is reasonable, due to the presence of a non-vanishing secondary mode amplitudes, as pointed out in §4.1.2. This is implemented in the code by setting $\chi_{E,e} = 1000 m^2/s$ on a few magnetic surfaces inside the island. Without any chaos around the X-point, the temperature increases across the whole plasma core. By increasing the amount of this "ergodic" area around the X-point, the temperature in the O-point is reduced.

Varying the input parameters (island radial width, the input power and $\chi_{E,e}$) in order to reproduce the T_e experimentally observed inside the island, M1TeV permits to estimate the $\chi_{E,e}$ value inside the island, highlighting that the essential cause of the heating of the magnetic island of a QSH state in RFX-mod is the reduction of the perpendicular thermal diffusion coefficient inside the island. No other mechanism (adiabatic compression, waves, etc.) is necessary to explain the peaking of temperatures observed in the experiments. Simulations have shown that the island ΔT_e is proportional to the island width, to the deposited power and to the inverse of the heat diffusivity. Comparing the M1TeV steady-state temperatures with the peak temperatures measured in the RFX-mod experiment during OPCD, it has been observed that QSH states bring about a reduction of the perpendicular heat conductivity from 1000 to $9-30 \mathrm{m}^2/s$, corresponding to a temperature jump in the range $80-300$eV. These values become comparable to the tokamak range of particle diffusivity, and are only a factor 2 larger than the values estimated by a guiding center code simulation [76], where ion motion is determined only by neoclassical effects.

4.4 QSH structures in high current OPCD plasmas

Recently, plasma current has been raised to 1.5MA, the highest value ever achieved for a RFP, and OPCD at such these regimes have been operated. High I_p values and the reduction of $b_{1,sec}$ achieved with OPCD operation have been resulted in enhanced QSH thermal profiles, with improved heat transport. An example is reported in Fig.4.17, where the T_e profile is illustrated. The maximum values of T_e are higher than in the past (reaching $\approx$ 1keV), as well as the ΔT_e of the island (generally about 300-500eV) and the ∇T_e gradient (about 4-7keV/m). The heat diffusivity in these regions decreased to the range of $5-15\mathrm{m}^2/s$, the lowest ever reached in RFX-mod [83].

At the time of writing, the three diagnostics used so far for QSH characterization were not simultaneously available. Only the multichord two-filter diagnostic operated continuously, allowing to compare different experiments.

Beyond the typical one illustrated in Fig.4.17, which is characterized by a localized thermal structure, two new different kinds of T_e profiles have been identified: the ***type 1***, with an evident thermal island in the plasma core displaced over a T_e plateau; the ***type 2***, where a peaked gradient confines a high T_e central plateau. Examples of T_e profiles for type 1 and type 2 are illustrated in Fig.4.18(a) and (b), respectively. The temperature profiles are from multichord diagnostic (red circles) and TS (blue circles) at the same time. SXR reconstructions come from similar plasma discharges with comparable T_e multichord profile, both for type 1 and type 2. In type 1, a localized SXR and thermal structure is present, while in type 2 the SXR structure is so large that it covers a significant portion of the plasma core.

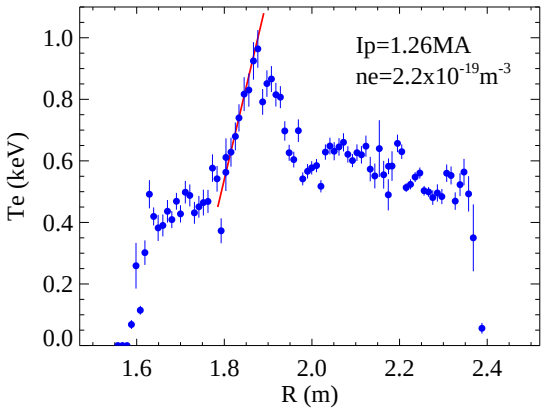

Figure 4.17: *High steep gradients in enhanced QSH thermal profile obtained in a high current OPCD discharge in RFX-mod (#21982, $t = 75ms$).*

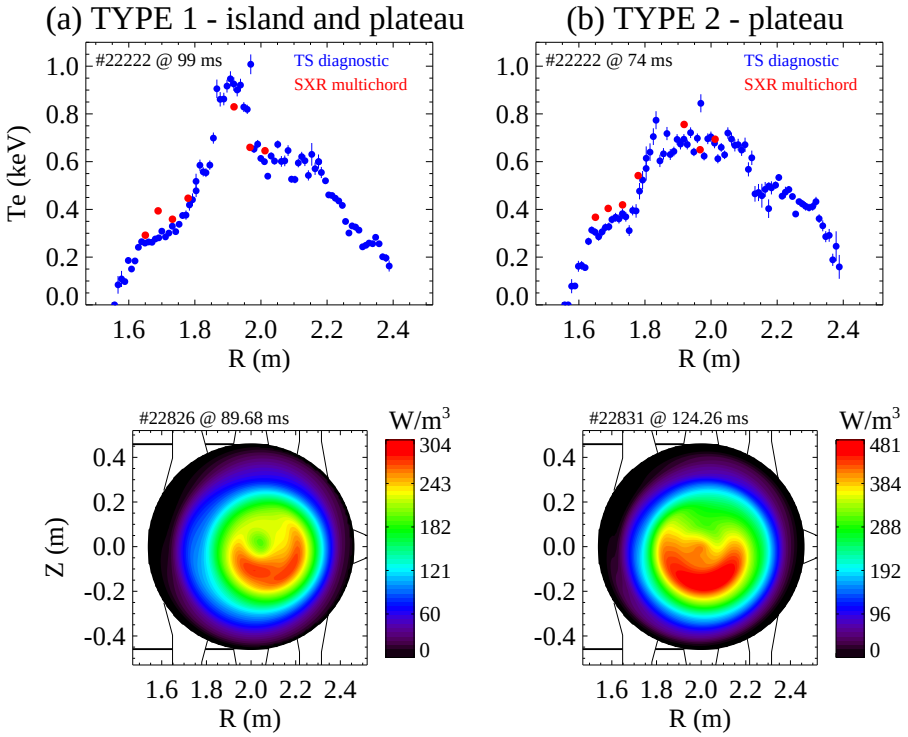

Figure 4.18: *Temperature profiles (from TS and the SXR multichord diagnostics) and reconstructed SXR emissivity distributions for new QSH states obtained in RFX-mod, in high current OPCD discharges. Two different QSH behavior have been identified: type 1 (a) and type 2 (b).*

4.4.1 SXR T_e evolution

Despite its lower spatial resolution (if compared to TS), the multichord diagnostic provides valuable information on the structure time dependence. In particular it can be used to estimate the duration and evolution of the thermal structure.

Let us consider type 1 QSH regimes (that is a thermal island over a plateau), with a T_e profile as in Fig.4.19(a) ($t = 99$ms), where the TS (empty circles) and multichord (colored full circles) temperature measurements are illustrated. The QSH regime starts at $t = 87.5$ms and lasts up to 105ms. The 3D temporal evolution of the T_e profile from multichord diagnostic in the QSH regime is displayed in Fig.4.19(b). In (c), the evolution of each multichord T_e measurement is illustrated, with colors corresponding to the full colored circles in (a). It is evident in (c) that there are two different temporal ranges: in the first part ($87.5-98$ms) the temperature of all the multichord signals rises simultaneously; in $t = 98-105$ms, instead, the central T_e values (corresponding to the red, green, yellow and black colors, with $1.8 < p < 2.2$m) keep on raising until the end of the QSH regime, while the external chords remain at similar lower values (blue, pink and cyan colors). In cor-

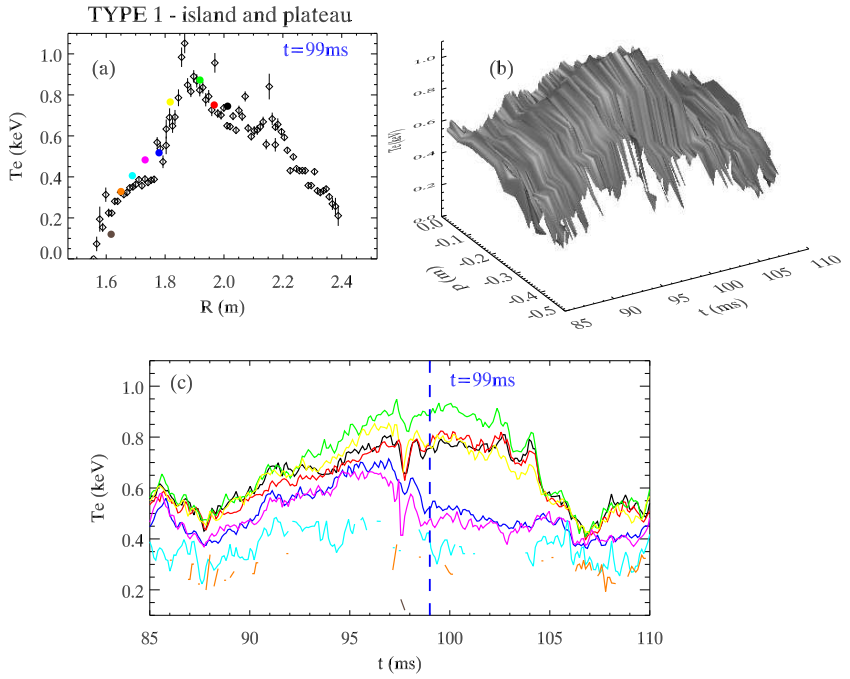

Figure 4.19: *TYPE 1: T_e profile (a) and its temporal evolution in 3-D plot (b) of a QSH period. The T_e evolutions for each full colored circles from multichord in (a) is displayed in (c), with color correspondence.*

respondence to the end of the QSH period, at $t = 105$ms, all the T_e values decrease (from 107ms on). The ΔT_e from the central and external chords remains constant for about 5ms, after which the higher temperatures decrease at lower values and all the central T_e values go on to decrease down to about 0.4keV, at the end of the

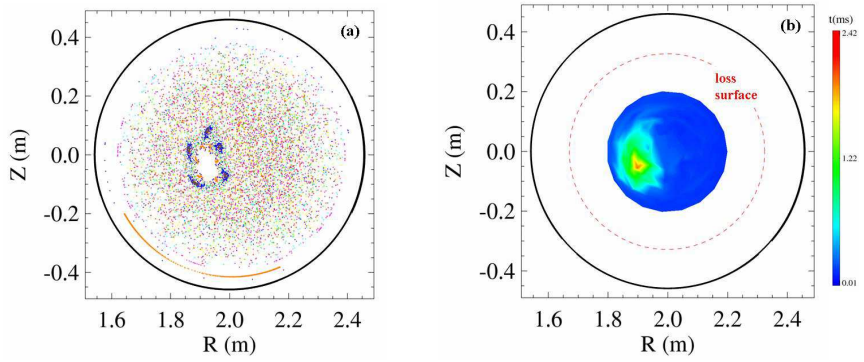

Figure 4.20: *(a) Poincaré plot computed by ORBIT and (b) particle τ_{loss} calculated by ORBIT in the plasma core region.*

QSH period. It is possible to deduce that there is a general heating of the plasma core in which a localized structure arises from the plateau background, after the initial heating. A topological magnetic reconstruction by ORBIT for type 1 case is illustrated in Fig.4.20(a), where a localized region of more conserved flux surfaces is evident and surrounded by a sticky region in the plateau. The $\tau_{loss,e}$ time for electrons reaching a circle surrounding the plasma core as simulated in the code is displayed in (b), where an asymmetric profile is evident: it is peaked in the region corresponding to the magnetic island ($\tau_{loss,e} = 2.5$ms), has an intermediate value in the plateau region (~ 0.5ms) and it is very low outside the island.

A different behavior is observed for the type 2 case, illustrated in Fig.4.21. In this case, all the central measurements (a) of the multichord diagnostic are almost at the same T_e value of about 0.7keV, which is the same as measured from the TS diagnostic. Their time evolution is reported in the 3D plot (Fig.4.21(b)) and in (c) with corresponding colors as in (a). No evidences of a hotter region are observed: the T_e measurements grow all together during the QSH period ($190-200$ms) and different gradients are observed. While in the plasma core the plateau is maintained for all the QSH period ($\sim 190-199$ms), at the edge very steep gradients take place. The $\tau_{loss,e}$ rate calculated by ORBIT in this case maintains the asymmetric shape

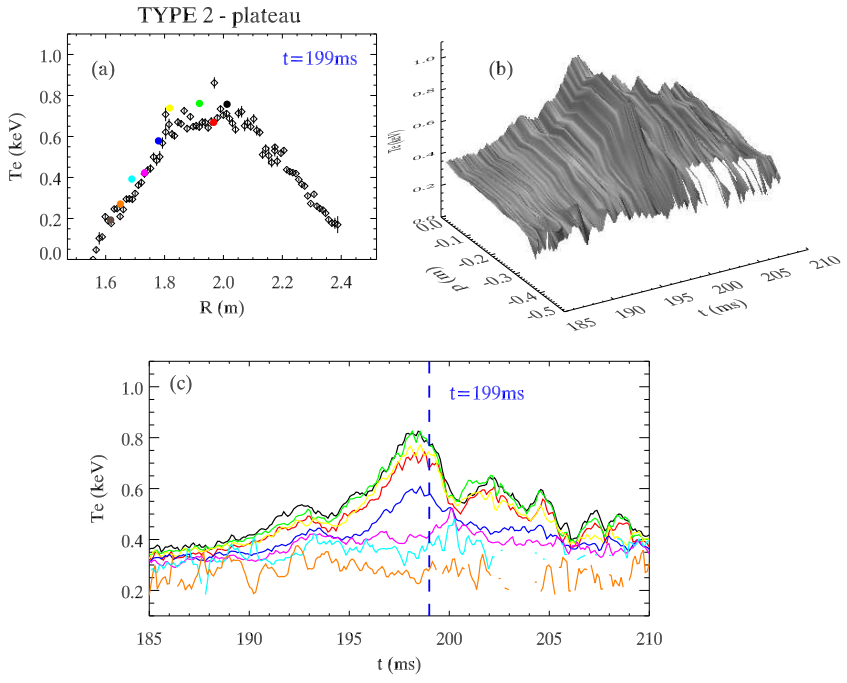

Figure 4.21: *TYPE 2: T_e profile (a) and its temporal evolution in 3D plot (b) of a QSH period. The T_e evolutions for each full circle from multichord in (a) is displayed in (c), with the same color correspondence.*

as for the type 1, but the values are higher (about 30ms). The asymmetry due to the magnetic island is not clearly understandable considering a completely flat T_e profile, even if the higher $\tau_{loss,e}$ values suggest lower transport coefficient in the plateau region. It is possible to speculate that other phenomena are taking place in this region, thus determining such a flat T_e profile, but they are not yet understood.

4.4.2 M1TeV for high current QSH in RFX-mod

An attempt to give an explanation of what happens in QSH states described in the previous paragraph has been performed with the M1TeV code. In this code, a fundamental role is assumed by the angular island dimension, which is determined by the chaotic region introduced near the separatrix. If the island separatrix surface is maintained and the X-point is “closed”, there is a topological and thermal separation between core and edge of plasma, which can be simulated with high but different $\chi_{E,e}$ values. In this case, the conserved flux surfaces of the island are all characterized by low $\chi_{E,e}$ values, while in the previous paragraph the region around the X-point was assumed to have high $\chi_{E,e}$ values, similar to those in the region outside the island. An example of this M1TeV island configuration is reported in Fig.4.22. It is not necessary that $\chi_{E,e}$ has the same value in the core and outside the island, as soon as it is larger than the inside. By fixing the island width, it is possible to let T_e evolve and then compare the results with the experimental ones, as summarized in Fig.4.23.

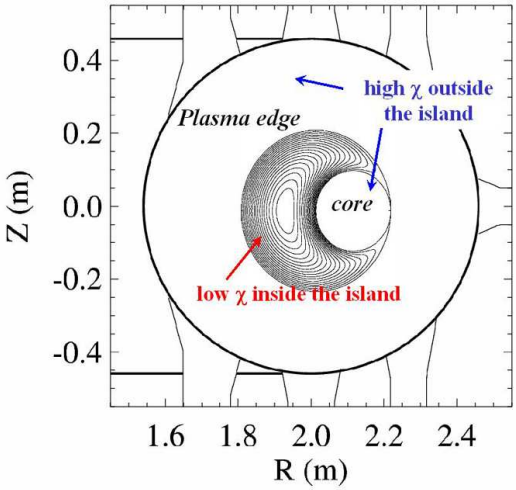

Figure 4.22: *$\chi_{E,e}$ as defined in the M1TeV in presence of a "closed" separatrix: $\chi_{E,e}$ values outside the island and in the core are not requested to be exactly the same.*

The presence of a closed separatrix in the simulation allows for a growth of T_e inside the island, leading to a localized and well-defined thermal structure. This structure is reported in Fig.4.23(a), where the contour plot of the simulated T_e is illustrated. The T_e profile calculated along the black arrow in (a) is displayed in (b); the corresponding experimental T_e profiles are showed in (c). The correspondence between the simulated temperature profiles and the experimental ones is very good. The T_e profile for type 1 is well simulated under these assumptions in M1TeV. The low value of $\chi_{E,e}$ inside the island where the flux surfaces are well conserved determines the growth of a thermal localized structure. The high $\chi_{E,e}$ value assumed in the core could explain the flat temperature profile, which however is at T_e val-

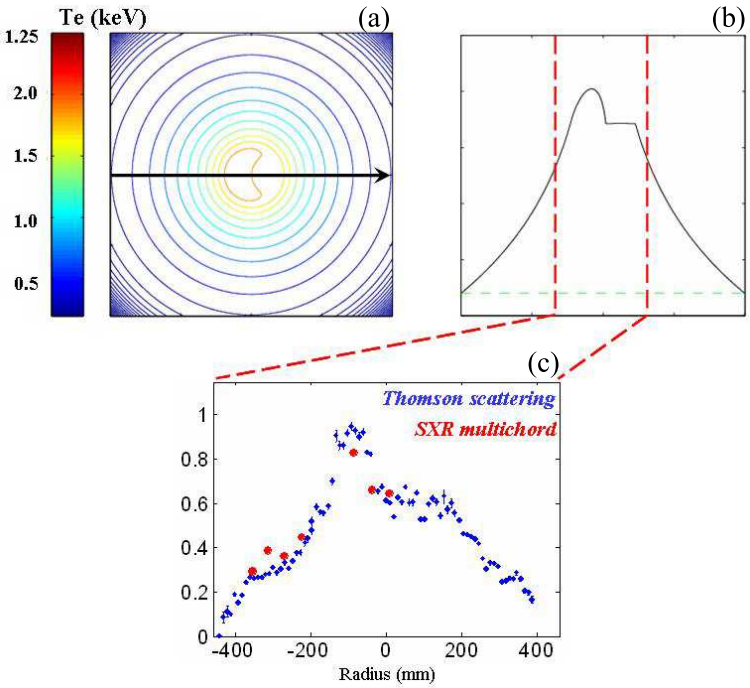

Figure 4.23: *TYPE 1: M1TeV temperature results match the experimental T_e measurements.*

ues higher than the ones reached outside the island, due to the separation between the core and the external region due to the X-point. A further confirmation of this configuration is reported in Fig.4.24, where (a)-(b) the 2D T_e profile from M1TeV is reported, looking along an arrow which is differently displaced. In this case, the temperature profile assumes a shape in which there seem to be two localized thermal structures, in correspondence to two small "dumps". Actually, the thermal island is only one, but it is cut in a particular direction, taking into account the two tails of the bean-shaped island. Experimentally, T_e measurements with the same shape have been observed, thus further supporting this model (Fig.4.24(c)).

Even though so promising for the type 1 island case, nonetheless M1TeV simulations do still not reproduce type 2: there are no set of inputs parameters to reproduce a such flat plateau in the plasma core as in Fig.4.18(b), with high temperatures and steep gradients at the edge. The assumptions and approximation M1TeV is based on could not be optimal for the understanding of such QSH states: these T_e profiles seem not to be an evolution of type 1 case, but a separate and different regime.

Possible explanations which are still object of discussion are the following:

1. the time dependence of the source: as the island heats up, the source decreases, at least in the regime where the resistive time is longer than the transport time;

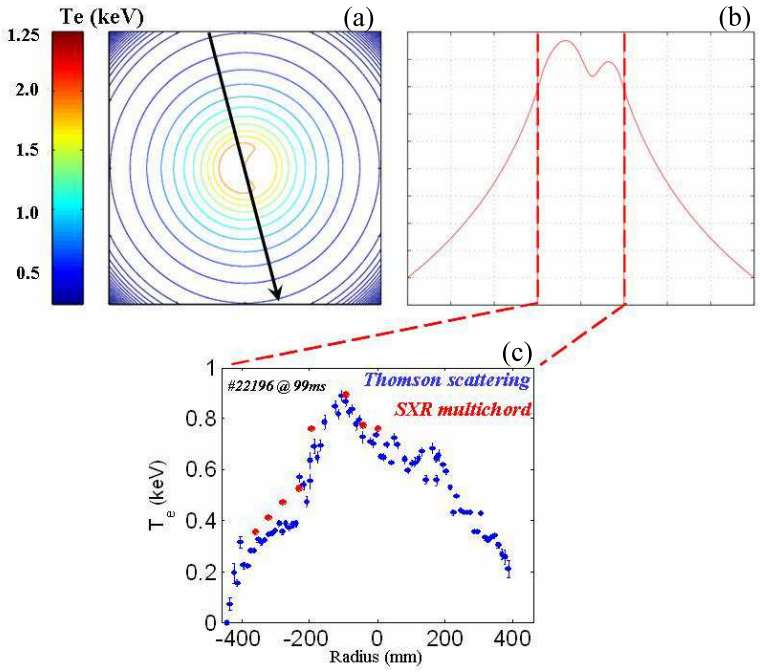

Figure 4.24: *TYPE 1: M1TeV temperature results match the experimental T_e measurements for a different perspective than in Fig.4.23.*

2. a complete $m = 1$ reconnection, which in the tokamak gives birth to poloidally symmetric temperature profiles [84].

Both research directions require anyway to take into account in M1TeV the topological evolution of the island together with the diffusion equation.

A clear and definite explanation of these QSH island features (both for type 1 and type 2) in RFX-mod is not yet achieved. A first attempt has been proposed in Ref.[85], where the authors suggest the association between type 2 profiles and the expulsion of the separatrix, even if in this thesis latter case a large temperature gradient within the island be visible (at a first approximation, flux surfaces are surfaces of constant temperature). At this stage, we can only assert that in the plasma column, the central region seems to be clearly separated by the external one, even if the mechanism is not yet understood. The analysis is still ongoing work, but the promising results with ORBIT and M1TeV codes suggest that the understanding of these new QSH states, characterized by reduced transport and enhanced confinement, is about to be reached.

CHAPTER 5

SXR in MST: from tomography to *Te* map determination

The MST experiment has complementary characteristics with respect to RFX-mod: the metal wall allows low density operation; lower currents are typically investigated and therefore lower power is used; vacuum requirements are less stringent allowing extra flexibility for diagnostic development. That allows for the SXR tomography to run in various configuration settings. The most common and exploited configuration is the *normal* configuration, where all the Be foils mounted on the four probes have the same thin thickness ($\approx 15\mu$m). That permits to apply the tomographic algorithms to obtain plasma SXR emissivity reconstructions with a temporal resolution dictated by the bandwidth of the electronic system [69]. This is the configuration used for the studies and results obtained in the first part of this chapter (§5.1).

As SXR emission is an indirect function of plasma temperature, experiments have been performed to study the feasibility of a diagnostic for 2D electron temperature measurements, based on SXR tomography. During the development phase, which is still ongoing activity, several configurations were realized and studied:

- The ***multicolor*** configuration. Mounting Be foils with different thickness on each probe, plasma emissivity can be investigated in different energy ranges and any contribution to radiation but bremsstrahlung can be studied. This allowed to determine the optimal filter thickness aimed at estimating the electron temperature. A first investigation on electron temperature profiles has been possible even with this configuration, by simulating measurements by means of the model described in Apx.C. Details and results obtained with this SXR tomography configuration are reported in §5.2.

- The ***two-color*** configuration. Such a configuration can be thought of as two independent SXR diagnostics in two different energy ranges. Therefore, plasma temperature can be obtained by analyzing the ratio between the SXR tomograms. Details are described in §5.3.

Finally, two examples of these tomography configurations for T_e estimation in high current PPCD plasmas are reported: the temperature evolution in a MH plasma (§5.4.1) and during pellet-injected discharges (§5.4.2).

5.1 SXR tomography results in MST

A detailed study of the dynamics and magnetic topological effects of resistive-tearing modes for different operational regimes in the MST experiment is illustrated in Ref.[69]. SXR tomography played a fundamental role in these studies, together with numerical reconstruction of magnetic-field lines by ORBIT code [43, 44]. Particular attention has been focused on mode dynamic during PPCD operation. While it always occurs that secondary modes decrease during PPCD, the behavior of the dominant mode varies. In some cases, QSH spectra are observed, together with a poloidally localized SXR structure. In other cases, also the dominant mode decreases. The decrease is such that magnetic islands in the core do not overlap: SXR tomography allowed to detect the SXR structures located around the rational surfaces of the innermost resonant modes [42]. In all

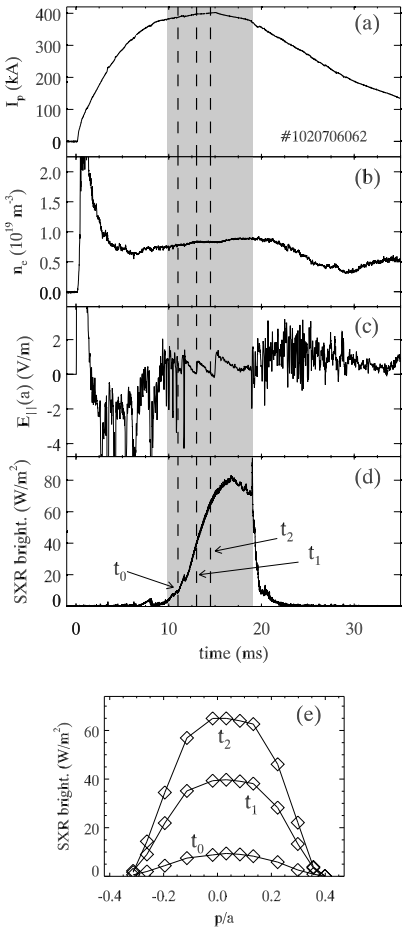

Figure 5.1: *Waveforms of the main plasma parameters for a 400kA PPCD discharge: (a) plasma current, (b) core electron density, (c) parallel electric field, and (d) core SXR brightness. The grey band highlights the period in which PPCD is applied. (e) Radial profiles of the SXR brightness at three times during PPCD [69].*

these studies, the MST tomographic diagnostic has been run with only two probes (SXR1 and SXR2). In the following paragraphs, more details on 400kA PPCD discharges and on the SXR structures observed in this operational regime are reported.

5.1.1 QSH imaging in PPCD plasmas

An example of MST 400kA PPCD discharge as considered in [69] is illustrated in Fig.5.1, where plasma current (a) as well as the density n_e (b), the parallel electric field at the plasma edge $E_{||}(a)$ (c) and an example of SXR signal (d) are displayed. The grey region highlights the time interval in which PPCD operation is applied (between 9 and 19ms). In panel (e), three SXR brightness profiles from SXR1 probe are illustrated, corresponding to three different times (t_0, t_1 and t_2) during PPCD. The SXR signals typically increase their value and reach the maximum when the deepest values of the reversal F parameter are achieved.

In Fig.5.2, an example of tomographic reconstruction with QSH spectrum during the PPCD discharge at $t = t_2$ of Fig.5.1 is illustrated. The brightness profiles used as inputs to the inversion algorithm are shown in Figs.5.2(a) and 5.2(b) with full circles. The continuous line in these figures represents the brightness profiles computed from the inverted emissivity map. The matching between experimental and inverted data is very good. The reconstructed SXR emissivity map reported in Fig.5.2(c) highlights a bean-shaped, highly emissive structure on the top of a symmetric profile. A comparison with magnetic data shows that this structure is associated with the ($m = 1,\ n = 6$) magnetic mode, which dominates the QSH spectrum, being the innermost resonant one. The maximum of SXR emissivity correspond to the island O-point, and it is approximately 20% more emissive than the background.

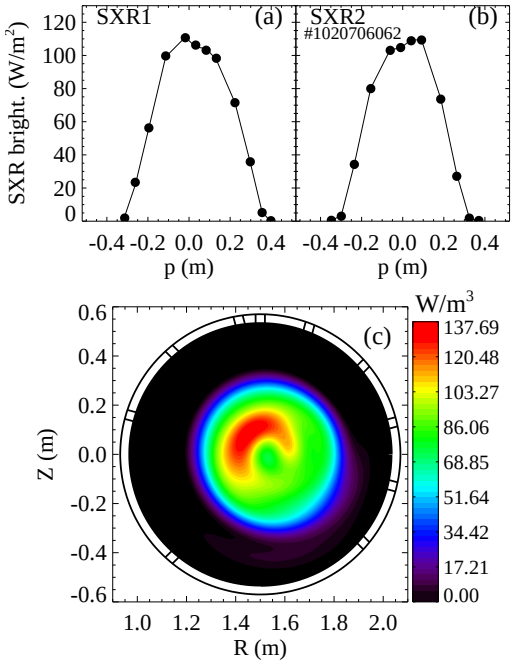

Figure 5.2: *(a) and (b) SXR brightness profiles (full circles) with evidence of a radially localized structure. The data correspond to the same shot as in Fig.5.1 at t=15.47 ms. The solid line represents the SXR brightness as computed from the inverted 2D emissivity map reported in (c), which shows the presence of a SXR island in the plasma core [69].*

In MST, due to the magnetic-mode rotation, the identification of these structures can be performed on a single shot basis using fluctuation analysis. In fact, SXR islands are observed to rotate at the same frequency as the dominant magnetic modes (see next paragraph for details). In addition, the position of the reconstructed SXR structure corresponds exactly to the poloidal position of the magnetic island O-point, as derived from magnetic measurements [69]. The toroidal array of pickup coils allows the determination of the amplitude and phase of the poloidal component of the perturbed field. The poloidal position of the magnetic island O-point at the tomography section corresponds to the poloidal position of maximum field taken at that toroidal angle. The identification of the SXR structure with magnetic island is supported also by numerical simulation with the ORBIT code. An example of comparison between the tomographic reconstructions and the Poincaré plots of the magnetic field is shown in Fig.5.3. The SXR tomographic reconstruction (a) of the bean-like structure investigated above, stretches over a large volume of the plasma column and is rather elongated in the poloidal direction. The corresponding Poincaré plot (b) shows a region with conserved flux surfaces, both in radial and poloidal extensions, that resembles the SXR structure.

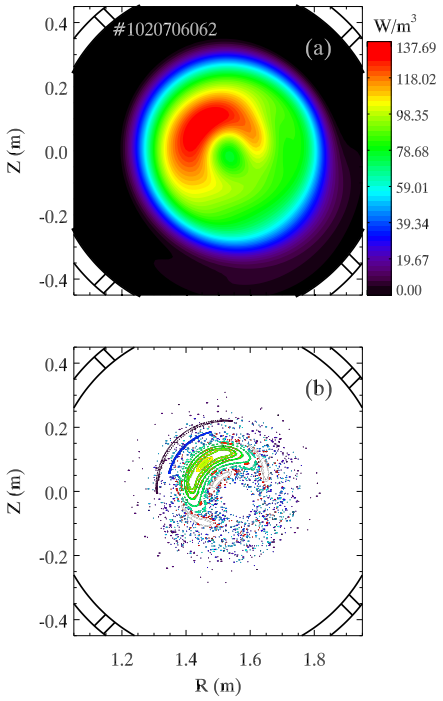

Figure 5.3: *(a) SXR emissivity map reconstructed during the QSH PPCD discharge presented in Fig.5.2. (b) ORBIT reconstruction of the magnetic field lines at the same time [69].*

The SXR and magnetic structures associated to QSH spectra are also detected in standard plasmas, even though smaller and less persistent if compared to PPCD (400kA). This is mainly due to the reduction of secondary mode amplitudes which is a general feature of PPCD experiments with a QSH spectrum [69].

Magnetic mode rotation and SXR oscillation

Typically, in QSH plasmas regular oscillations are present in the SXR brightness signals, with a frequency which is associated to the poloidal rotation frequency of the dominant mode. The maximum of the brightness profile oscillates around the magnetic axis of the plasma column. If lines of sight looking at the plasma edge are considered, the oscillation pattern corresponds to the oscillation of the domi-

nant mode. In particular, for those external chords opposite to the magnetic plasma axis, the oscillation patterns are out-of-phase [69]. That is due to the rotation of the SXR structure, which intersect the lines of observation at different times. A more complex behavior is instead present in those chords passing near the magnetic axis, where a double-oscillation pattern appears: at the rotation frequency of the dominant $(1, n_0)$ magnetic mode f_{1,n_0} and at its second harmonics, $2f_{1,n_0}$. An example of these dynamics is illustrated in Fig.5.4: a cartoon of a SXR structure rotation is illustrated in panel (a), together with four lines of sight, the external opposite chords (A and D) and the central ones (B and C). The blue region represents the SXR structure, which is rotating along the green circle, centered on the plasma magnetic axis. The experimental SXR measurements, black lines in panel (b) for the chords represented in panel (a), are compared and well superimposed to the simulated ones (red lines). These SXR brightness simulations have been computed using a SXR model that assumes pure bremsstrahlung radiation. A detailed description of the model is reported in Apx.C. SXR signals are simulated by assuming that they are produced by a localized hot and more emissive region in the plasma column, added to a symmetric equilibrium emissivity profile, and rotating at a constant angular velocity in flux surface coordinates. Toroidal effects are con-

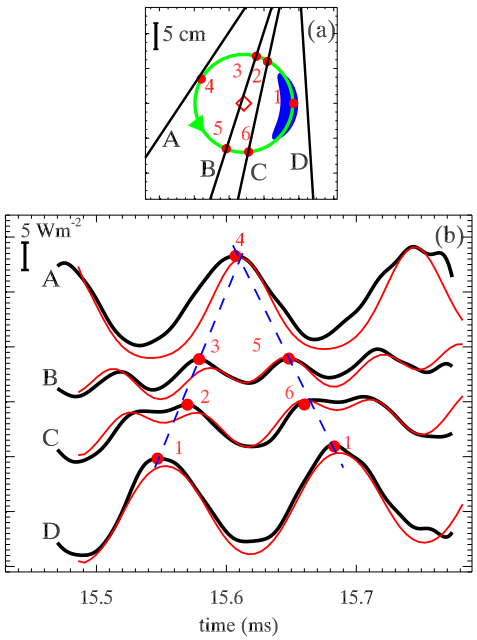

Figure 5.4: *(a) Scheme of the SXR island used to model the experimental signals. The blue region corresponds to the 90% contour level of the model emissivity map. The diamond represents the magnetic axis. (b) Experimental high-pass-filtered SXR signals (thick black line) and modeled ones (thin red line) for the chords shown in (a). The numbers refer to the position of the SXR structure indicated in (a) [69].*

sidered by assuming an outward differential shift of equilibrium magnetic surfaces (see Apx.C). In addition, the model takes into account also the helical displacement of the flux surfaces due to the dominant magnetic perturbation [69]. As the hot localized region is rotating, a linear variation of the poloidal angle of the center of the structure has been considered. In Fig.5.4(b), a very good correspondence between the experimental signals and the simulated one is observed.

In the framework of this model, the presence of the first harmonic in signals measured by central chords can be explained as follows. If we call ρ^* the radial position of the island, chords with impact parameter $p > \rho^*$ display a single peak, as the structure crosses the chord only once in a rotation period [see cartoon in Fig.5.4(a)]. Chords with $p < \rho^*$ are instead characterized by two peaks per period, as the region crosses them twice per rotation. The double-peak pattern, i.e. the higher harmonics in the central chords, is a feature that permits to identify the presence of a poloidally localized rotating structure, which has harmonic components with $m > 1$. In fact, if the structure has a pure $m = 1$ component and only a sinusoidal poloidal dependence is assumed for the hot region, no signs of a double peak appear in the simulation.

5.1.2 MH imaging in PPCD: evidences of multiple helical flux surfaces

In PPCD discharges with Multiple Helicity spectrum, SXR tomograms allow for detecting the presence of multiple structures. Modes amplitudes are low and the corresponding islands are rather narrow. The corresponding SXR signals are difficult to detect, compared to single QSH islands. Nevertheless, a clear evidence has been found by analyzing the fluctuation pattern [42]. The analysis of the filtered SXR signal at the two harmonics in fact reveals the presence of a beating pattern, due to the different rotation frequency of the two modes. The beating pattern is observed both in the first and in the second harmonics: it implies the presence of two single poloidally localized structures rotating in the plasma core, at those frequencies [42]. SXR reconstructions of these two islands are displayed in

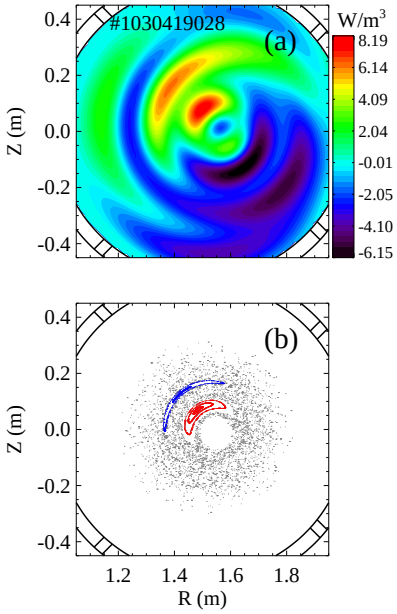

Figure 5.5: *(a) SXR emissivity map reconstructed from highpass-filtered signals and (b) ORBIT reconstruction of the magnetic-field lines during a MH PPCD discharge in which the ($m = 1, n = 6$) and ($m = 1, n = 7$) islands appear simultaneously.*

Fig.5.5(a), performed considering only the fluctuating component of the measured brightness signals, so that the radial shape of the perturbed emissivity is better visualized. These signals have been filtered between 22 and 64 kHz to retain only the first and second harmonics of the fluctuation. The radial positions of the two structures are consistent with the resonance radii of the $(m = 1, n = 6)$ and $(m = 1, n = 7)$ modes. By analyzing a sequence of tomographic reconstructions, not shown here, the two structures rotate in the poloidal direction at different velocities. The field line tracing performed with the ORBIT code and reported in Fig.5.5(b) shows the presence of two magnetic islands at the same radial positions of the reconstructed SXR structures displayed in Fig.5.5(a).

5.2 Multicolor configuration

5.2.1 Impurity contribution to radiation

In the MST device the inner metal wall is made of Aluminum [86], and the SXR measurements can be affected by the presence of Aluminum ions (fully or partially stripped) inside the plasma, both with recombination and line radiation contributions. The most intensive Aluminum lines are those of Al XIII, at energy of 1.729keV [87]. If we consider high current PPCD plasmas ($I_p \approx 500 - 550$kA), this radiation contribution is limited to the core of the plasma column. In addition to the lines, Aluminum recombination steps are present too, with energy of 2.1 and 2.4keV [87].

Further line contributions are due to several other impurities, including He, B, C, N, and O [86]. In PPCD experiments on MST, however, bremsstrahlung is a significant fraction of the total emission and it can be accurately measured, if appropriate Be foils are used for SXR measurements.

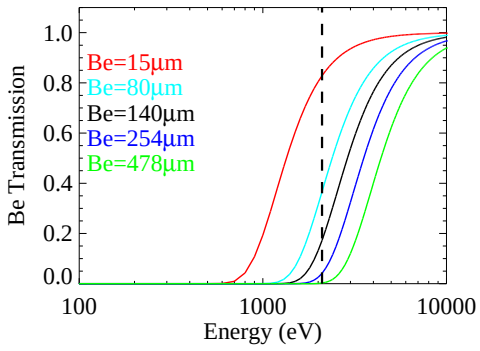

Figure 5.6: *Beryllium transmission function: different thicknesses have been considered. The dashed line corresponds to the energy of the Aluminum line radiation at* ≈ 2.0*keV.*

All these considerations led to the idea of running the tomographic diagnostic in the *multicolor* configuration, in order to investigate the plasma emissivity in various energy ranges, and try to estimate if contributions other than bremsstrahlung affect the SXR measurements. Two sets of filters have been selected:

- **Set #1:** 80, 15, 140 and 478μm for SXR1,2,3, and SXR4, respectively;

- **Set #2:** 140, 15, 254 and 478μm for SXR1,2,3, and SXR4, respectively.

The thicknesses have been measured with an error of $\pm 1\mu$m. The cut-off energies for these thicknesses are illustrated in Fig.5.6, where the transmission function of Be filters is reported. The black dashed line corresponding to $\approx$2.0keV is approximatively at the energies of the Al line radiation and recombination steps. If 10% of the transmission function is considered as Be cut-off energy, only thicknesses larger than $200-300\mu$m prevent SXR measurements from being affected by line radiation or recombination step contributions.

Since large Be thickness values have been used (if compared to the 15μm adopted in the normal configuration), only 500-550kA PPCD shots have been exploited, in order to have sufficiently high SXR fluxes impinging onto detectors.

An attempt to check out if the Aluminum radiation really affects the SXR measurements has been performed. An example of SXR brightness spectrum for the above set #2 of Be foils, is illustrated in Fig.5.7. By considering the measurements from chords looking at the same plasma region but using different Be thickness, the brightness spectrum can be obtained. The brightness of the four chords of Fig.5.7(a), which has been averaged on 0.2 ms at the maximum of SXR emissivity, is illustrated in Fig.5.7(b), as function of the Be cut-off energy (the colors of the full circles in (b) correspond to the colors of the lines of sight in (a)). By considering the bremsstrahlung dependence from T_e ($\sim e^{-E/T_e}/\sqrt{T_e}$), a fit can be computed, but considering only the measurements that do not include Aluminum contributes, that is for the signals with 254 and 478μm thickness. Those signals with thinner foils are affected by Al radiation: in the 15μ-thick signal (red circle) the Al contribution seems to be consistent, while in the 140μ-thick one (black circle) it is marginal. This confirms that in the normal configuration with 15μm-thick Be foils, SXR measurements are affected by Aluminum radiation and pure bremsstrahlung

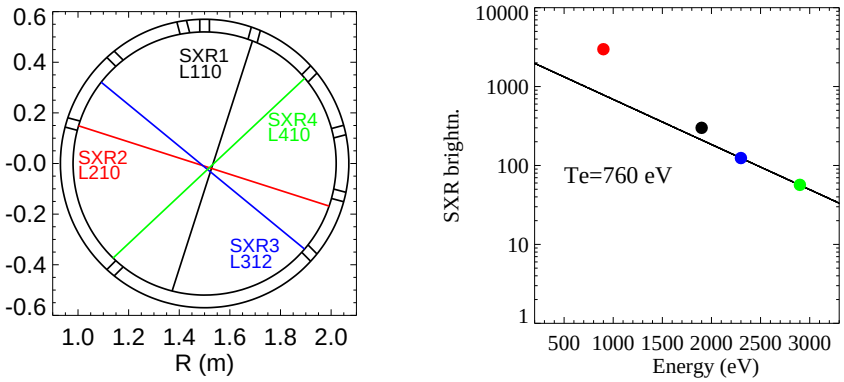

Figure 5.7: *(a) Lines of sight looking at the same plasma region, but with differen Be foil thickness. (b) Energy spectrum of the SXR measurements corresponding to the line of sight in (a), fitted by a T_e function (black line) including only bremsstrahlung radiation dependence. The fit has been computed only among the measurements corresponding to the blue circle (254μm) and green one (478μm), which should be lacking of line and recombination radiation contributions. The red one (15μm) does not belong to the fit, while the black circle (140μm) is marginally affected by Al radiation.*

contribution can be evaluated only with filters thicker than 200-300μm.

5.2.2 SXR emissivity simulation

As in the multicolor configuration the four probes house Be filters with different thickness, the tomographic algorithms cannot be applied for the plasma emissivity reconstruction. Anyway, information on the emissivity, and in particular

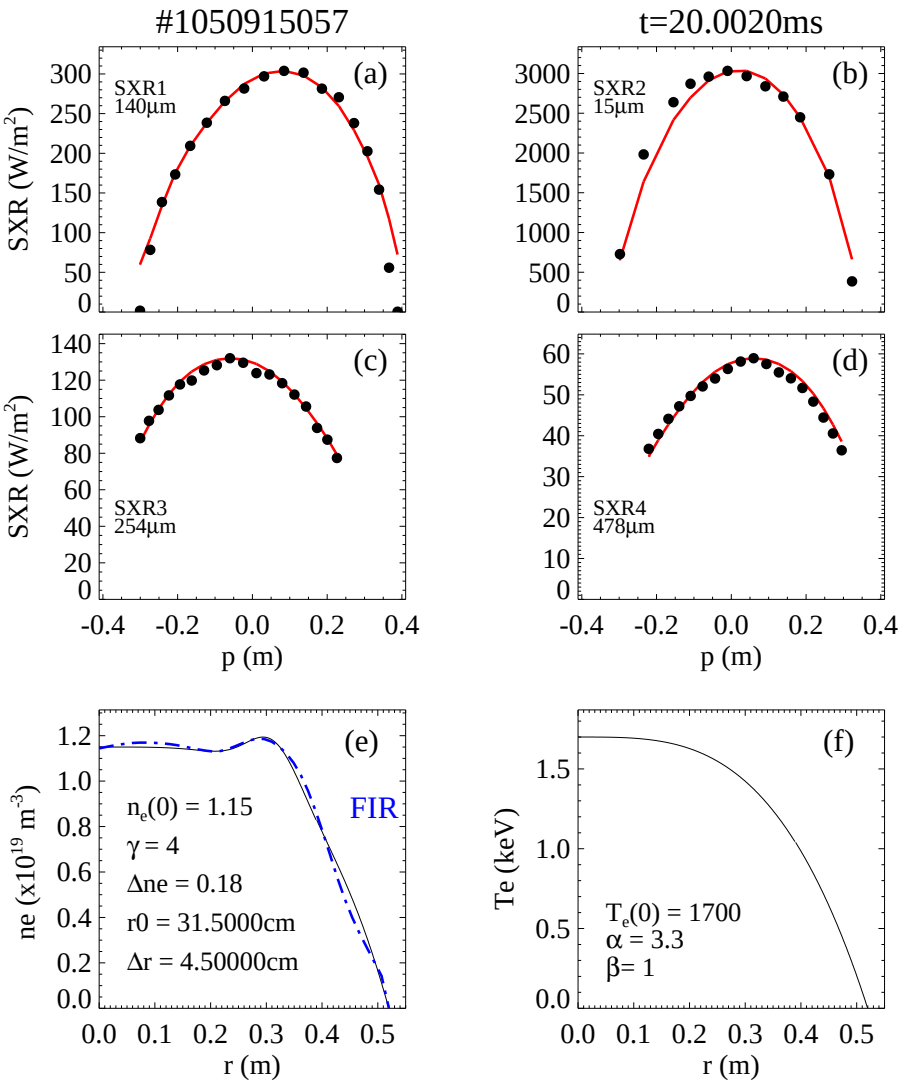

Figure 5.8: *Experimental brightness (full circles) and simulations (red lines) for a SXR emissivity profile modeled with T_e and density symmetric profiles displayed in the two bottom panels. Experimental density profile (from FIR diagnostic) has been used, while T_e has been obtained by matching the SXR simulation with the experimental measurements.*

on T_e and density profiles, can be obtained all the same by modeling the SXR emissivity distribution in order to match the experimental brightnesses with those computed with the model in Apx.C. An example is shown in Fig.5.8. In order to better reproduce SXR brightness profiles, a slightly hollow density profile has been used, as shown in Fig.5.8 (such a radial profile is consistent with interferometric measurements from FIR [88]). The four upper panels display the SXR experimental brightness profiles (black full circles) for the four cameras (the corresponding Be foil thickness is highlighted for each probe). In the last two bottom panels, the density and the electron temperature profiles used in the simulation are displayed. For the density, the experimental measurements from the FIR diagnostic are superimposed (red line), while no Thomson Scattering measurements of T_e are available for this case. The parameters used for the simulation of both n_e and T_e are shown in the corresponding panels. The shot considered here (#1050915057) corresponds to a PPCD plasma in a MH state. QSH regimes are difficult to be considered: even if SXR tomography can detect and resolve the small structures appearing in such regimes with thin Be foils, using thick filters as in the multicolor configuration no evidences of out-of-phase SXR oscillations due to the mode rotation as in §5.1.1 are observed. Moreover, the high level of noise requires significant filtering, so that detection of islands is impossible, as the averaged signal period is longer than the rotation period.

By properly adjusting the parameters, the model is able to fit rather well the experimental brightness profiles. Only SXR measurements with the thinner filter (SXR2, Be$=15\mu$m) are not very well reproduced. Such a disagreement is due to the presence of Al contributions, which are not properly included in the model. The SXR emissivity profile determined with the parameters reported in Fig.5.8, is illustrated in Fig.5.9, where both the contour map and a 3D plot are displayed.

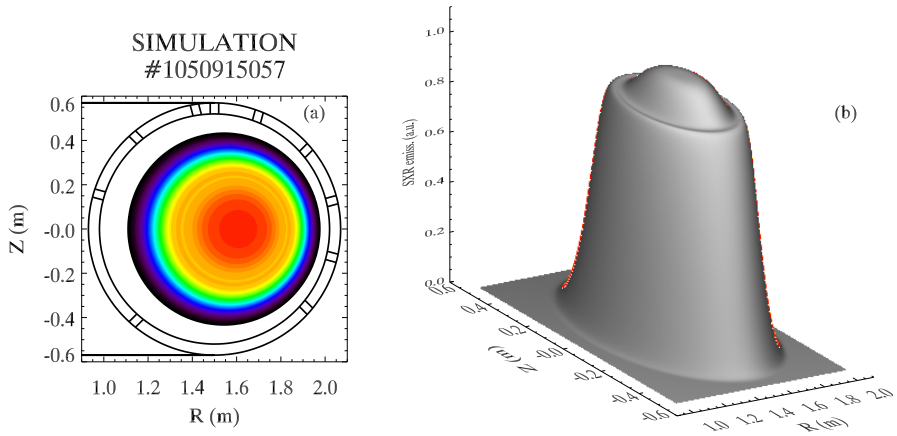

Figure 5.9: *SXR emissivity profile simulated for the case in Fig.5.8.*

SXR emissivity distribution in high current PPCD plasmas

By computing various emissivity simulations for a large number of shots in the multicolor configuration, several characteristics of the SXR emissivity of MST high current PPCD plasmas can be figured out.

- A high displacement of the magnetic axis, Δa, has been detected. It has been found out to vary between 8 and 9cm, sometimes reaching 10cm. Plasma is shifted outward, to the low field side of the vessel, so that the magnetic flux surfaces are greatly compressed. These Δa values must be taken into consideration for the tomographic reconstruction, in order to optimize the algorithm parameters and use the poloidal harmonics just to reproduce asymmetries in the plasma column, excluding the Shafranov-shift. This shift is taken into account by centering a priori the reconstructed emissivity on Δa.

- Steep gradients are present at the emissivity edge, which are smoother at lower PPCD plasma currents. Flatness is found in the core of the plasma column, due to the flat or slightly hollow density profile (as in Fig.5.8(e)).

- The flatness of the core and the steep gradients at the edge lead to a sort of "discontinuity" (as displayed in Fig.5.9(b)), which in some cases gives rise to a hollow SXR emissivity distribution.

- At lower PPCD plasma current, SXR emissivity is typically smoother, with a peaked density profile which corresponds to a peaked SXR emissivity. In that plasma core distribution, no flatness is present.

SXR model and QSH structures

Despite the high level of noise, information on T_e profiles during QSH PPCD have been obtained and are displayed in Fig.5.10. A discharge with a non-rotating island has been considered. In this way, it is possible to operate an average on the SXR signals of 0.2ms in order to reduce the noise but without losing information on the SXR structure shape and position.

The n_e profile implemented into the model has been calculated from the FIR experimental measurements, while T_e has been introduced and varied until a good match between the simulations and the SXR experimental data has been achieved. The simulated SXR brightness profiles (red lines) fit the experimental data (black full circles) coming from the probes, even if small differences are present [see panels (a) - (d)]. The radial T_e profile in the section throughout the island O-point is illustrated in the third row of panels of Fig.5.10: radially the island covers most of the plasma core. A contour plot of the T_e profile simulated for matching the SXR brightness signals is displayed in the last bottom panel (g), where a bean-like thermal island emerges form the plasma column. The large poloidal size of the structure combined to the large radial one as results from the simulation, suggests

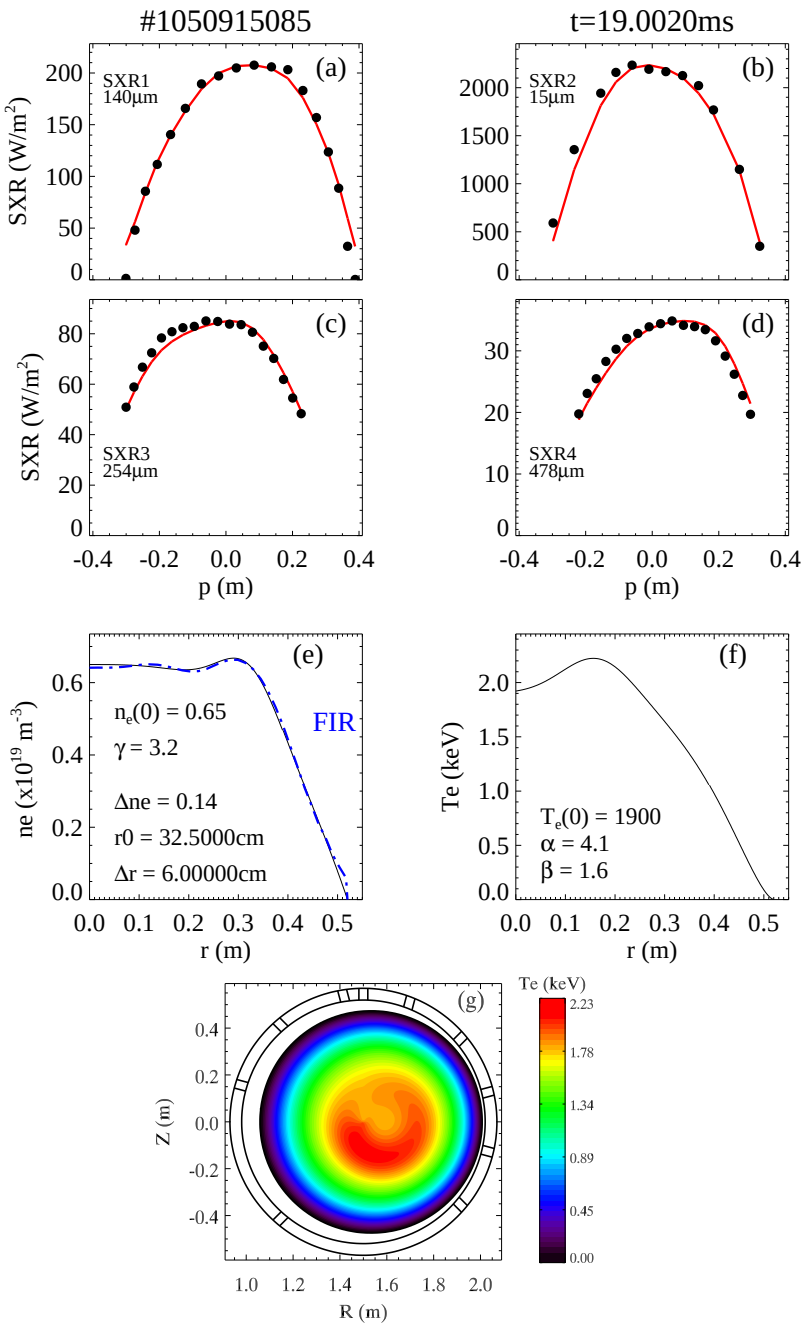

Figure 5.10: *Experimental brightness (full circles) and simulations (red lines) for a SXR emissivity profile modeled with T_e and density displayed in the panels of the second row from the bottom. Experimental density profile from FIR diagnostic has been used. No TS measurements are available; a localized T_e structure has been added (QSH regime). In the last bottom panel (g), a contour plot of the simulated T_e is displayed.*

that the structure is occupying a very large part of the plasma column core: it could be similar to what has been reported for the RFX-mod experiment in §4.4. We can speculate that in this case, the island is so large that it has replaced the column axisymmetric equilibrium, and the island itself is the new core of the plasma. So, the plasma column becomes helically distorted. No additional experimental information are at present available to confirm this hypothesis.

5.3 The two-color configuration and *Te* estimation

Thanks to the multicolor measurements, it has been possible to select the proper filters to obtain SXR bremsstrahlung measurements. Couples of SXR probes have been equipped with identical filters (303μm-thick Be foils on SXR1 and SXR2; 761μm-thick filters on SXR3 and SXR4). Therefore, it has been possible to per-

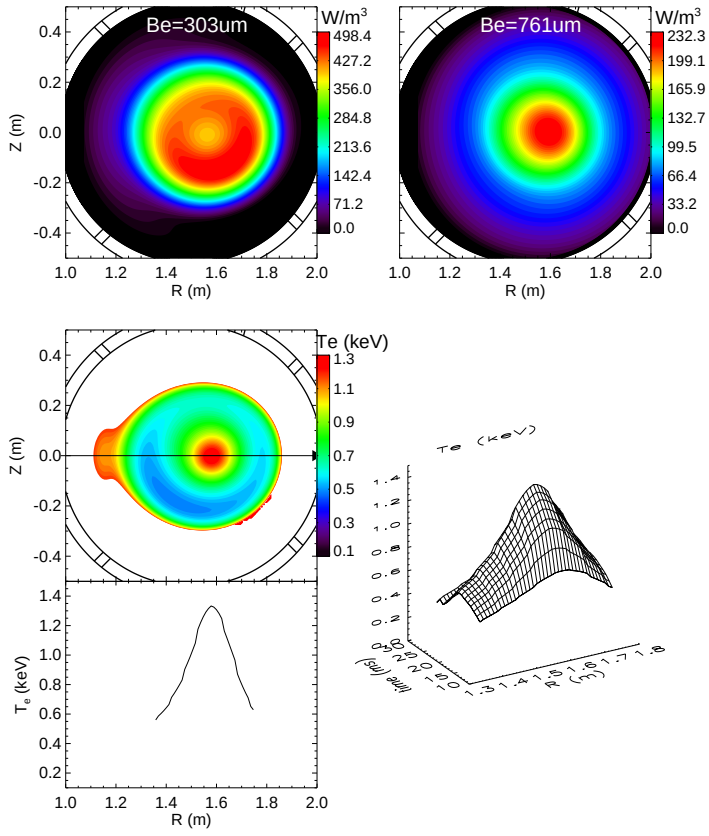

Figure 5.11: *The reconstructed emissivity distributions* $\varepsilon(303\mu m)$ *and* $\varepsilon(761\mu m)$ *, together with the* T_e *contour plot and radial profile for a given time. The 2D reconstruction of* T_e *is also shown.*

form, simultaneously and on the same cross section, two tomographic measurements with different Be filters.

Using only two probes for each reconstruction, the spatial resolution is partially reduced, but it should provide to track fast changes of the electron temperature in the plasma core. The T_e is estimated with the two-foil technique directly by calculating the ratio R between the SXR reconstructions in the two energy ranges. An example of the two reconstructions in the two-color configuration is illustrated in Fig.5.11: for each pair of probes (SXR1-2 and SXR3-4) the contour plot of the emissivity distribution for a 550kA PPCD plasma is displayed. No evidences of a more localized emissive region are present (MH state), and the emissivity is symmetric in both the energy ranges. By using the relation between the ratio of the SXR reconstructions, R, and the electron temperature (§3.4), a 2D estimate of T_e can be obtained. The interpolation formula of $R(T_e)$, for the Be filters used, is [89]:

$$T_e = \exp(8.911 - 2.649\ lnR + 0.885\ ln^2R - 0.156\ ln^3R + 0.011\ ln^4R). \quad (5.1)$$

The T_e contour and the radial profile along the black arrow in the midplane are illustrated in Fig.5.11. Both SXR and T_e profiles indicate that plasma is shifted towards the outboard side of the vessel more than in standard discharges and that the application of PPCD can distort the plasma shape and make it poloidally asymmetric. The reconstructed 2D temperature presented in the same figure shows that the T_e remains above 1keV for several milliseconds, with a maximum value of 1.3keV.

5.3.1 Limits in the two-color configuration

The two-color configuration of the SXR tomography system in MST proved effective at determining the 2D map of T_e: the possibility to estimate a 2D map of the electron temperature all over the entire discharge (or at least when the SXR fluxes are high enough) would be a big goal for studying the performances of the plasma and understanding the RFP physics. However, several practical reasons limit the possibility to reach these goals.

First of all, the two reconstructions are performed with only two cameras, so that the available spatial resolution is low. In this case, for each reconstruction, only 34 and 40 lines of sight can be useful for determining the emissivity distribution in the two different energy ranges. This number of measurements was sufficient for high SXR fluxes as for those measurements obtained with thin Be foils (about 15μm) and reported in §5.1.1, but it is too limited with thicker filters. In fact, Be foils thicker than 200μm allow for small SXR fluxes impinging onto the detectors, so that the maximum gain values in the amplification system must be set ($1 \div 5 \times 10^7$). As a consequence, the signal to noise ratio (SNR) decreases noticeably, and the high amount of noise affecting data used for the tomographic algorithms creates aliasing effects.

A solution to reduce the SXR signal noise level could be to filter the measurements at low frequency (1-2kHz at maximum) or averaging signals into small time ranges. In this case, however, all the information on a localized hotter region and its

rotation (associated to the rotating dominant magnetic mode during QSH) would be lost. Moreover, noise is not uncorrelated and part of it is due to the magnetic field fluctuations. In such conditions, tomographic reconstructions are affected by significant systematic errors.

Finally, the distortion of the plasma column occurring during these experiments is such that a significant systematic error occurs if only two cameras (i.e. only SXR1 and SXR2) are used in the reconstruction. In order to illustrate this error, a simulation has been performed during a MH PPCD shot, with no significant asymmetries in the SXR profiles. From a simulated emissivity as displayed in Fig.5.12(a), a set of synthetic measurements as if all the probes had the same filters can be simulated. The tomographic reconstruction on the synthetic brightness data (Fig.5.12(b)) corresponds very well to the original emissivity in panel (a). On the other hand, if only two cameras are used for reconstructions, a significant dis-

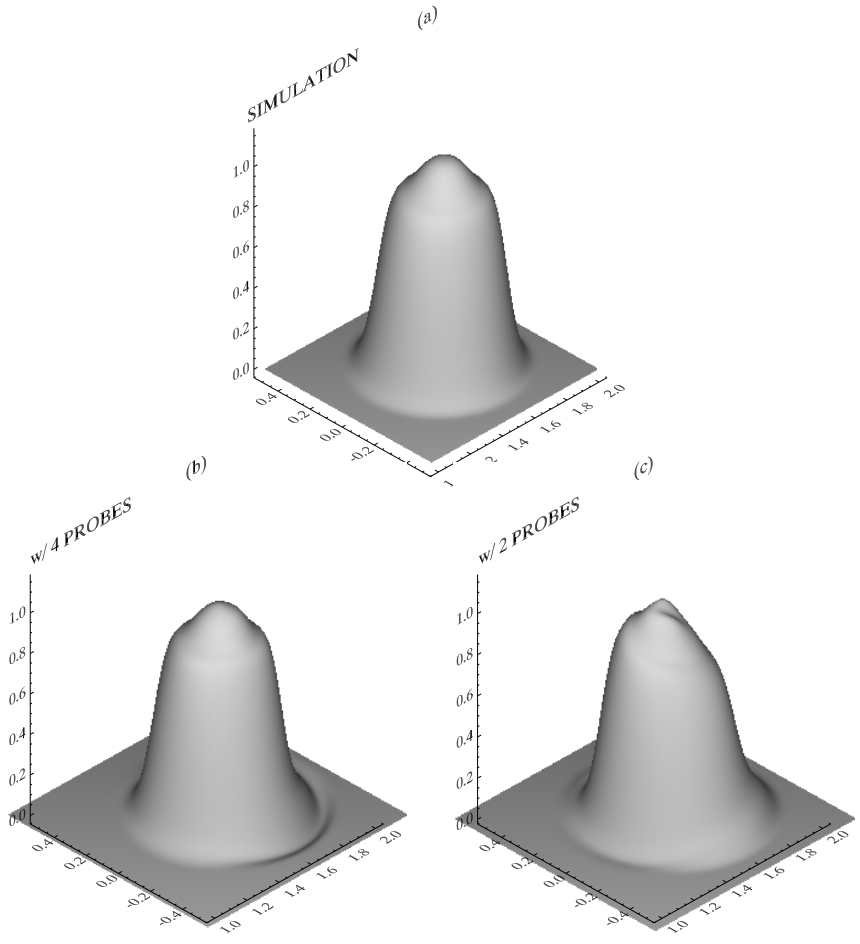

Figure 5.12: *SXR plasma emissivity simulation (a) and tomographic reconstructions, with four probes (b) and with only two probes, SXR1-SXR2 (c).*

crepancy is observed in the reconstruction (Fig.5.12(c)). We can conclude that a different algorithm need to be developed in order to reduce such a systematic error.

5.4 MST PPCD plasmas and *Te* estimate

Despite the various aforementioned limitations, by means of the simulation, information on T_e profiles have been obtained in a variety of PPCD plasmas.

5.4.1 *Te* evolution in a MH PPCD cycle

An example of the on-axis $T_e(0)$ electron temperature calculated by means of the SXR emissivity model for a PPCD shot is displayed in Fig.5.13, together with the main plasma parameter (I_p, density n_e, F and $m = 1$ toroidal magnetic mode amplitudes). The 3D plot evolution of the experimental density profile from FIR data and of the simulated temperature profile performed in the midplane of the plasma vessel for the same shot is illustrated in Fig.5.14(a) and (b), respectively. The $T_e(0)$ maximum value of ≈ 1.7keV corresponds to the maximum of SXR brightness, that coincides with the deepest values of the F parameter. Recent Thomson scattering measurements have shown that the high performances achieved in PPCD shots have been overcome, and new record values of ≈ 2.0keV have been observed [90].

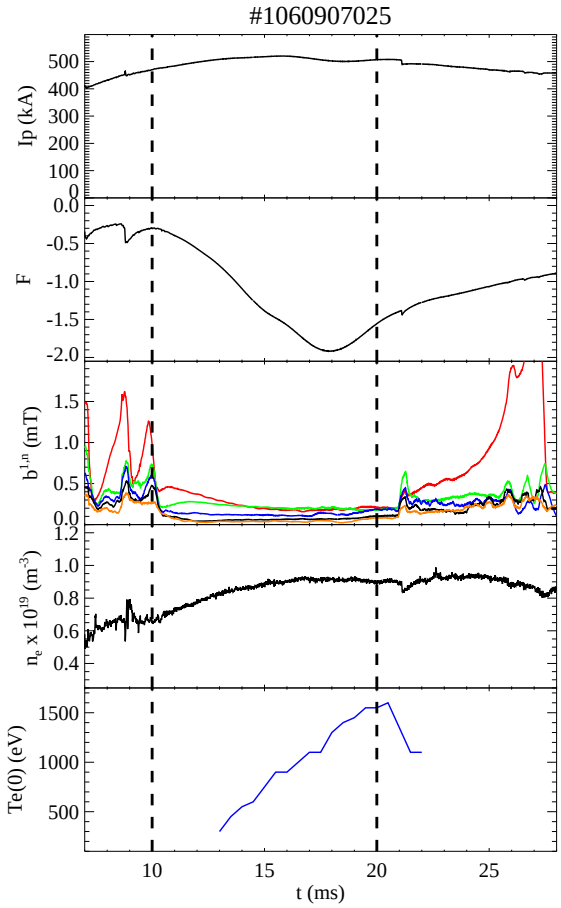

Figure 5.13: *Temporal evolution of main plasma parameters in a PPCD shot. In the last panel, the on-axis $T_e(0)$ temperature estimated by the SXR emissivity model is displayed.*

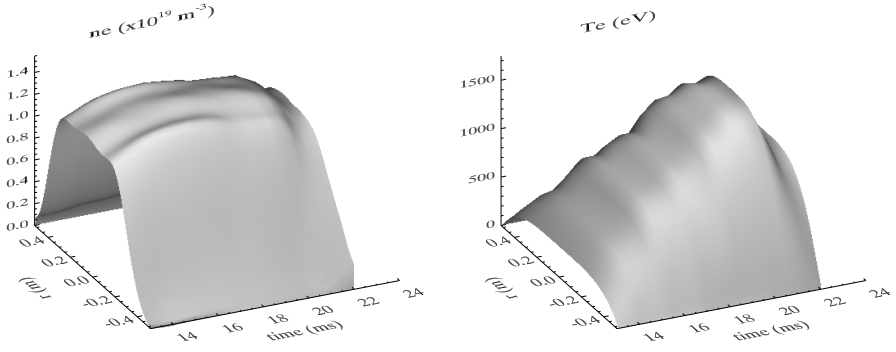

Figure 5.14: *3-D plot of the density (a) and of the midplane temperature (b) profiles in a high current PPCD shot (see Fig.5.13).*

5.4.2 Pellet injection and SXR emissivity

In PPCD discharges, a ten-fold improvement in energy confinement and an approximate doubling of the β parameter (that is the ratio of plasma pressure to the confining magnetic field pressure) are observed [53]. The limit to higher improvements in energy confinement and β is the low value of density, $n_e \leq 10^{19}\mathrm{m}^{-3}$. If this value is overcome, $m = 0$ instabilities are triggered and the energy confinement degrades. It is believed that $m = 0$ destabilization occurring in higher density PPCD shots is due to an unfavorable change in the edge current or pressure profile, brought by the additional influx of cold neutral particles needed to get higher density. In these low density, ohmically heated plasmas, the reduction of tearing instability resulted in a rapid increase in the electron temperature, while the ion temperature remained unchanged.

The maximum electron temperature achieved (1.3 keV) was as much as four times the ion temperature [53]. One mechanism for heating ions is collisional energy transfer from the electrons, but the energy transfer time $\approx T_e^{3/2}/n_e$ is ten times longer than the duration of improved confinement.

This increase in the electron temperature has led to relatively large β, with total β in the MST reaching 15% [53]. Although β is high, it is below the threshold for MHD instability. A β limit has yet to be experimentally identified in RFPs.

One possibility to increase density in the MST device, except for puffing during the discharge, is to inject deuterium pellets into the plasma. The injection of pellets during PPCD application, allows for reducing magnetic fluctuation and for increasing the density up to 4 times the typical value, $n_e \approx 4 \times 10^{19}\mathrm{m}^{-3}$. In Fig.5.15(a), the main plasma parameters for a high current PPCD plasma with pellet injection is displayed: the I_p current, the F parameter, the electron density n_e and the toroidal magnetic fluctuation b_t. At 14ms the confinement improvement starts, as it is indicated by the stop of magnetic fluctuation bursts, shortly after the ablation of the injected pellet. The corresponding T_e and T_i measurements are illustrated in Fig.5.15(b) [91]: the electron temperature increases during the PPCD application,

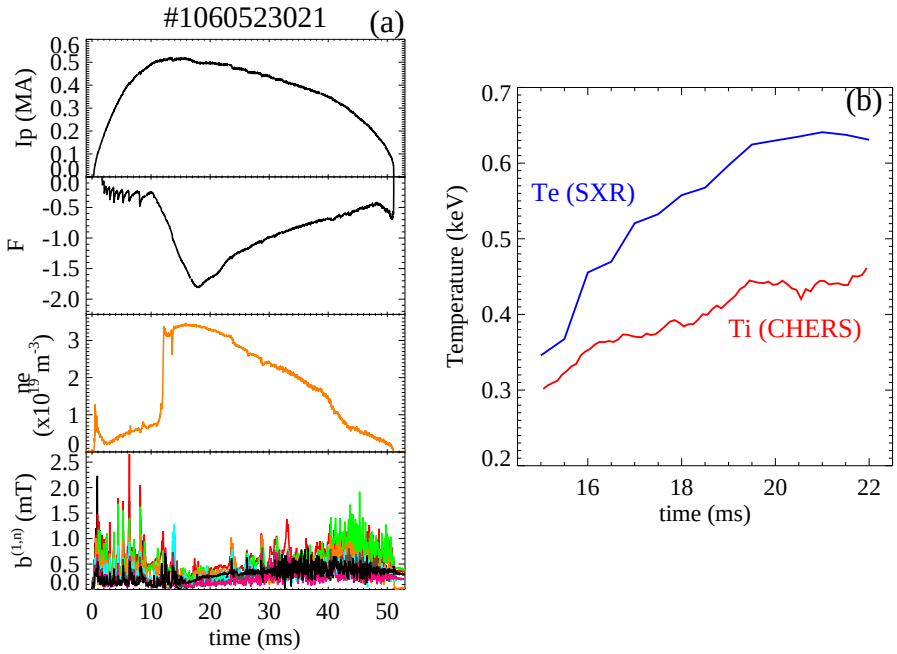

Figure 5.15: *(a) Main plasma parameters in a 500kA PPCD plasmas with two 1.6mm diameter pellets injected at roughly 11ms. (b) Corresponding electron and ionic temperatures as in (a).*

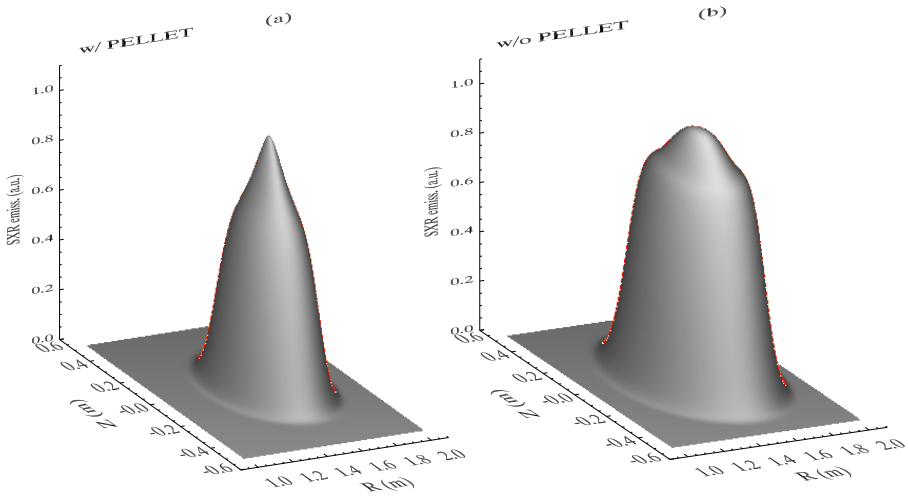

Figure 5.16: *SXR emissivity distribution simulation for a 500kA pellet-fueled PPCD shot (a) and without pellet injection (b). Both the emissivity distributions are considered for the 303µm-thick Be filter tomographic measurements.*

within 14 and 24ms; the ion temperature value increases too during the improvement period, even if it is less effective. T_e, which is the on-axis plasma temperature, is measured with the two-foil technique of the SXR tomography in the two-color configuration. The ion temperature is measured by charge exchange recombination spectroscopy looking at CV ions [92, 93, 94], which are tightly coupled to the bulk deuterons. The improved particle confinement, which means higher density values, is implied by a stationary density profile and a reduction of D_α radiation [95].

In the period of particle confinements after pellet ablation, at I_p larger than

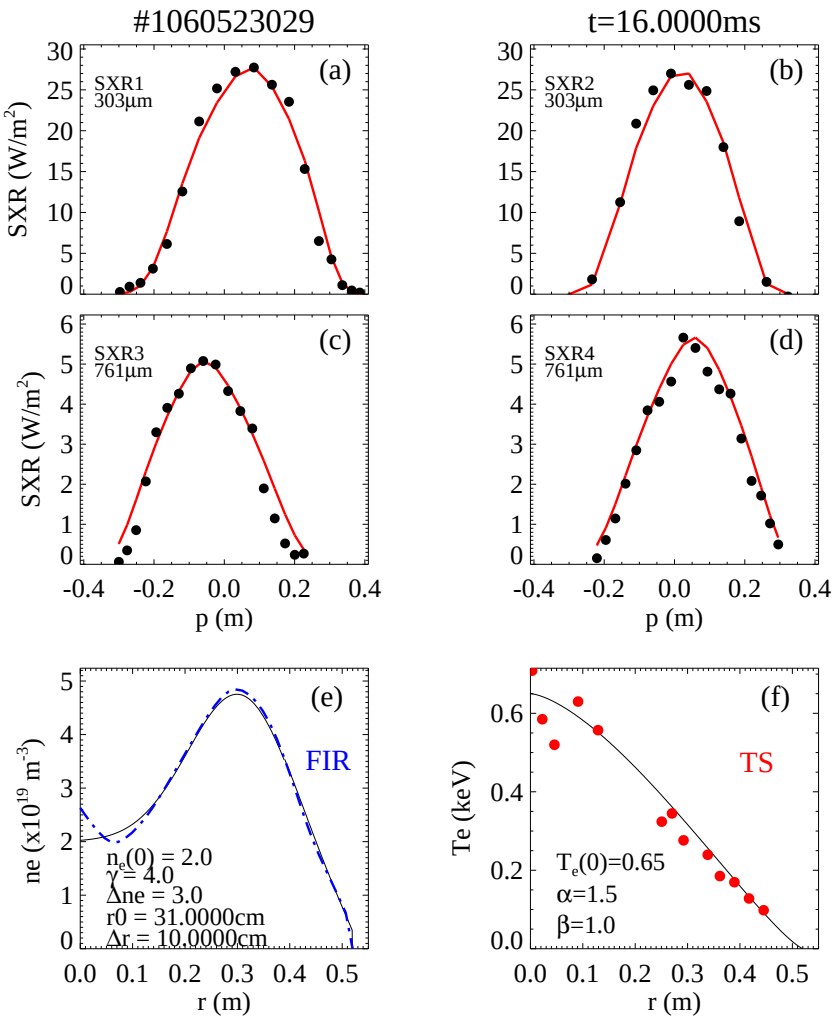

Figure 5.17: *Experimental brightness (full circles) and simulations (red lines) for a SXR emissivity profile of a high current pellet-fueled PPCD shot. Experimental density profiles and T_e (FIR data and TS measurements displayed in the bottom panels) have been implemented into the model. In this case, the density profile following the pellet ablation has a very hollow profile.*

500kA, density profiles can assume various shapes: the typical high current n_e flat or slightly hollow profile as shown in Fig.5.8, can be replaced by a peaked or a very hollow one. Electron temperatures T_e are smaller for pellet discharges than for typical PPCD high current shots, due to higher density values. Even the SXR plasma emissivity distribution is different: lower emissivity is detected as well as more peaked profiles. An example of SXR emissivity as computed by the SXR emissivity model for a pellet-fueled plasma is reported in Fig.5.16(a), while a non-pellet plasma emissivity is illustrated in Fig.5.16(b). In panel (a), SXR distribution is peaked and the emitting plasma volume is focused on the axis of the plasma column, smaller than the case in panel (b), where the SXR emissivity is larger. The experimental brightness profiles (full black circles) and the computed signals (red lines) for the emissivity in Fig.5.16(a) are reported in the first four panels of Fig.5.17. In this case, not only electron density profiles obtained from FIR data are available to be introduced into the model, but also the temperature data from TS diagnostic [96] have been implemented for the emissivity simulation. Slight adjustments for the T_e profiles with respect to the experimental ones are necessary, because the TS profile is measured along a vertical diameter. The plasma column axis is shifted outward for the Shafranov-shift (displacement up to $\sim$ 9cm for high current PPCD plasmas), so that TS measurements could not correspond to the T_e profile in the plasma core. The simulated density and temperature profiles are illustrated in the two panels in the bottom of Fig.5.17, together with experimental measurements: the dashed blue line refers to the n_e FIR data; the red full circles to T_e from TS measurements. The density profile is very hollow, but the low T_e values guarantee for a peaked SXR emissivity distribution, and not a hollow one.

5.5 Summary and open questions on *Te* from SXR measurements

The SXR tomographic diagnostic in MST is a fundamental tool for the understanding of plasma dynamics and characteristics. Detailed and complete studies in high current PPCD shots with the two-color configuration have not yet been achieved, even if several main issues have been highlighted and open questions have been pointed out.

First of all, the SXR emissivity distribution has been characterized: its "typical" shape has been identified; the necessity of optimizing the parameters of the tomographic algorithms or the necessity of different ones for its reconstructions by means only of two probes has appeared.

The multicolor configurations helped to define the minimum thickness for the Be foils to be used in the two-color tomography, to avoid Al radiation contribution.

The SXR model allows for determining electron temperature and density profiles which fit well the experimental measurements from FIR and TS. In fact, starting from density profile from FIR data, n_e can be implemented into the model, and then the T_e profile is varied in order to reproduce the SXR experimental mea-

surements. The best fit is obtained for those T_e profiles which fit well the TS signals. Similarly, starting from experimental T_e and varying the density profiles, the best fit of n_e reproduces the experimental measurements from FIR data. SXR measurements are therefore a fundamental diagnostic whenever FIR or TS are not available. The temporal evolution of n_e and T_e profiles can therefore be determined by repeatedly running the model even though this is a very long procedure.

Detailed analyses and comparisons between T_e profiles from SXR and TS diagnostics are still lacking, even if the preliminary results are encouraging, and are ongoing work. The differences sometimes observed are partially due to the reconstruction parameters which are not optimized, partially explained by the fact that the two instruments look at different regions of the plasma column. Recent analysis seems to suggest that Al contribution might affect the SXR measurements with 300μm-thick Be foils. Preliminary measurements with thicker Be filters (408 and 821μm) have overcome these T_e differences, so that a more detail and systematic analysis can be performed in the next future.

In any case, one of the most important feature identified with the SXR measurements is that, in high current PPCD plasmas, temperature profiles are peaked, and their absolute value is almost the same both for QSH regimes and MH states ($\sim$ 2keV for the best PPCD discharges). Differently to what happens in RFX-mod, T_e profiles are always peaked in such plasmas, and no localized temperature enhancement due to T_e structures emerging in the plasma core has been observed by TS. It could maybe due to the island rotation or a wrong synchronization of the TS laser with the island rotation and position. But could the island be such large to cover the whole plasma core, so that there is no possibility to discriminate from the localized island and the plasma background? This is on-going work, and no explanation has been yet presented. In any case, this could not explain the reason why the highest T_e values of about 2keV can similarly be obtained both in QSH and MH states.

CHAPTER 6

Summary and future perspectives

6.1 Summary

During the Ph.D. course, various research tasks have been investigated, all of them focused on the setting up and optimization of soft x-ray (SXR) diagnostics for the study of the SXR plasma emissivity radiation in two reversed field pinch (RFP) experiments, the RFX-mod and the MST device. The application of the tomographic algorithms to the SXR measurements has allowed for investigating the main characteristics of the plasma column in various operational regimes, and for studying the MHD instabilities arising in the plasma core. The two-filter technique applied to SXR data has permitted the estimation of the electron temperature T_e profiles and maps, in particular during regimes of advanced scenarios like the OPCD at high current in RFX-mod, or the PPCD operation in the MST device, where the best T_e values and performances have been observed. In particular, in RFX-mod, the SXR diagnostics allowed for identifying a new QSH regime.

In the following, the results reported in this thesis are summarized, together with the future perspectives.

6.1.1 SXR results in the RFX-mod experiment

The main points of the diagnostic activities, concerning commissioning and optimization of RFX-mod SXR diagnostics, are outlined in the following:

- While the SXR tomography and the on-axis multifilter spectrometer had been successfully exploited in RFX, and their installation on RFX-mod was relatively easy, the multichord diagnostic has been completely tested and assembled for the first time.

- The best configuration for the electronic chains of the three SXR systems has been investigated and realized, in order to reduce the noise and increase the SNR.
- The geometrical settings of the detection system and the electronic chain have been optimized for each SXR diagnostic.
- In the SXR tomography new beryllium filter supports for curved foils have been designed, realized and assembled, for avoiding the software correction to the SXR experimental signals.

Data analysis of SXR measurements allowed to reach the following results:

- ► The SXR tomography allowed for investigating the position of SXR structures in QSH regimes. The mismatch of the SXR center of mass and the position computed by magnetic measurements allowed to identify an important systematic error in magnetic measurements. Such an error was due to the current circulation in the actively controlled saddle coils. The correction of this error allowed for operating RFX-mod at the highest current for a RFP device.
- ► The reconstructed SXR structures have been identified with the magnetic islands and thermal structures, and their shape and dimensions have been compared to the ORBIT code.
- ► The SXR structure evolution has been investigated in QSH cycles in OPCD operation: the sizes increase as well as the dominant magnetic mode grows and the secondary ones decrease. The temperature inside the island increases, as confirmed by M1TeV code. The temporal evolution of the thermal structure can be followed by the multichord diagnostic.
- ► SXR measurements provide complete information on new types of QSH regimes obtained in RFX-mod at high current and during OPCD operation (but not only): topological information of the magnetic configuration come from the emissivity reconstructions, while the thermal evolution is assured by the high temporal resolution of the multichord diagnostic.

6.1.2 SXR measurements in the MST device

As far as the collaboration with the MST group of the University of Madison-Wisconsin is concerned, data analyses of SXR measurements for the characterization of the SXR structures observed in 400kA PPCD shots have been performed.

- ► SXR structures emerging in 400kA PPCD shots have been characterized, both in QSH regimes and in MH ones. In the former case, a big SXR structure corresponding to the magnetic island emerges in the plasma core: SXR measurements and reconstructions allowed for their characterization. In the

latter case, images of two SXR small structures, identified with a double island, have been obtained, thanks to the high resolution of the SXR tomography.

The plasma emissivity distribution in different SXR energy ranges (multicolor and two-color configuration) has been investigated, running the SXR tomography in various configuration settings:

- A contribution of impurities for measurements with a Beryllium thickness thinner than $\approx 250\mu$m has been identified. This information was used for selecting appropriate higher Be thicknesses, in order to measure only bremsstrahlung SXR radiation.

- Measuring the SXR emissivity in two different energy range allowed for obtaining the first 2D maps of the plasma electron temperature by means of a modified version of the two-foil technique algorithms, based on the ratio of two simultaneous emissivity reconstructions in two different energy ranges. The limited number of lines of sight available for the reconstructions relapses into a limited spatial resolution. Nonetheless, in MH regimes, appropriate averages on SXR measurements and the optimization of the reconstruction algorithms allow for a 2D temperature estimation of the plasma core.

- Evidences of higher spatial resolution of SXR emissivity reconstructions for T_e estimation have been highlighted in order to avoid systematic aliasing due to the limited number of lines of sight used in the reconstructions; thus the necessity for different algorithms to be used.

- Whenever the spatial resolution does not allow for applying the two-foil technique for the temperature estimation, a SXR emissivity model can be used. Even though it is time consuming, the SXR model permits to reproduce the experimental signals by means of density and temperature profiles simulations. Thus, n_e and T_e maps can be determined in an indirect way. Their temporal evolution can be found by iterative applying the simulation to the whole discharge.

- Despite the bandwidth limit, temperature maps of localized structures in QSH have been obtained by means of the SXR model. This was possible in particular experimental conditions, i.e. modes locked to the wall. Such a condition is not common, and it is usually associated to degraded performance.

- Analysis of SXR emissivity distributions at high current PPCD shot (500-550kA) allowed for identify several main features: steep gradients at the plasma edge and a flat core, resulting in a profile very different from the smooth one measured at lower PPCD currents.

6.2 Future perspectives

All the results reported in this thesis can be further enriched by new analysis and studies which are going to be done in the next future.

Future analysis on the RFX-mod experiment. The SXR diagnostics installed in RFX-mod will be fundamental tools for the next RFX-mod campaigns. One of them will be spent for high current discharges (1.5MA, and ultimately 2MA), with OPCD operation, in order to obtain the best plasma performances and higher T_e peaked profiles. In these regimes, new QSH regimes have been observed but a complete and exhaustive physics interpretation is still missing. Future measurements with all the SXR diagnostics running simultaneously (SXR tomography, multifilter and multichord diagnostics) will allow for a detailed observation of the plasma SXR emissivity distribution and of the temperature spatial profile and evolution. In addition, the possibility of injecting pellet into the island will allow for determining if particles are well confined inside the island. SXR measurements are sensitive to density variation, and that could be combined with the density measurement computed by the interferometry installed in RFX-mod. A more detailed description of their spatial characteristics, dimension and shape will be provided.

A new SXR diagnostic for the RFX-mod device. Further information on plasma column behavior and activity will be obtained in the near future by means of a new SXR diagnostic, which will be installed at the toroidal tomography location, replacing the horizontal manipulator installed at present. The diagnostic commissioning is planned for the next summer-autumn (2008), so that by the end of the year it will be operative during the RFX-mod experimental campaigns. A double target will be achieved with this new instrument: a higher spatial resolution for the SXR tomographic diagnostic as well as simultaneous measurements of the plasma emissivity in different energy ranges. Moreover, a simultaneous estimation of the electron temperature (vertical profile) can be obtained with the high temporal resolution characterizing the electronic system. In addition, the flexibility of the new system will allow for running the diagnostic in different configurations, so that various SXR measurements and geometrical settings of the lines of sight can be easily tested and realized. In this way, new important information on MHD dynamics will be gathered in a variety of conditions and operations, in particular as regards the formation and evolution of the SXR structures arising in the plasma core during QSH regimes, which are extremely promising for the understanding of physics in future RFP operations.

SXR and temperature measurements in the MST-device The SXR tomographic diagnostic installed in the MST experiment lends itself to various operations. Thicker Beryllium foils (410 and 821μm) are recently installed for completely Aluminum-free SXR measurements, in the two-color configu-

ration. Additional data will be gathered at high current PPCD shots, and comparison with the Thomson scattering diagnostic will be investigated. In addition, comparison of 500-600kA PPCD shots in MST and in RFX-mod will be studied, in order to investigate the performances and the differences between these two devices.

CHAPTER 7

SXR measurements in RFX-mod: a new diagnostic

7.1 Motivations for a new diagnostic

As explained in the previous chapters, the manifold intrinsic characteristics of SXR measurements make them a fundamental tool for fusion plasma studies, in particular for investigating the MHD resistive instabilities arising in the plasma core and sustaining the RFP configuration, both in MH and QSH regimes. In this context, the RFX-mod device with its thin shell and its unique saddle coil system turns out to be a preeminent experiment to be investigated in all its configurations (usual and exotic ones) and aspects. This represents a valid motivation for developing and realizing a new SXR diagnostic, which will upgrade the already existing tomographic system. A double goal will be achieved: to substantially increase the spatial resolution of the SXR tomography, and to add an extensive flexibility for studying different energy spectrum ranges of the SXR plasma radiation. All these aims will be performed by running the new diagnostic simultaneously in various configurations. The accurate temporal resolution of the in existence tomographic diagnostic will be preserved, permitting to follow the plasma dynamic temporal evolution with high accuracy.

New important information on MHD dynamics will be gathered in a variety of conditions and operations, in particular as regards the formation and evolution of the SXR structures arising in the plasma core during QSH regimes. The high number of lines of sight of this new diagnostic (65 channels) results absolutely necessary for identifying and characterizing in details the SXR structures associated to QSH regime spectra.

7.2 Mechanical project

7.2.1 Main general characteristics

The new SXR diagnostic (DSX3) is going to be installed in the horizontal port-hole of the RFX-mod chamber, replacing the horizontal SXR manipulator of the tomographic system presently installed. As it completes the existing tomographic diagnostic, it maintains several primary characteristics of the original SXR manipulators (such as the remote control and the auxiliary pumping system), but further features are added: a larger number of lines of sights, a wider flexibility in the detection system geometry and the possibility of simultaneity in selecting different radiation energy ranges of detection.

The instrument is separated from the main RFX-mod vacuum ($10^{-8} - 10^{-9}$mbar) by a gate valve, remotely controlled. The decoupling of the RFX-mod vacuum from the diagnostic one requires an UHV auxiliary pumping system, which is implemented in the pumping system of the in existence tomographic diagnostic, from which it inherits the control and regulation system. Actually, the auxiliary pumping system of the tomographic diagnostic (which is the same for the tomographic and bolometric diagnostics, for a total of seven manipulators, all of them similar in the mechanical part) is going to be modified. The seven UHV pumping lines (one for each manipulator) are going to be replaced by a single one: a unique pump for the rough line, a single vacuum tube (160mm in diameter) and a single turbo-pump.

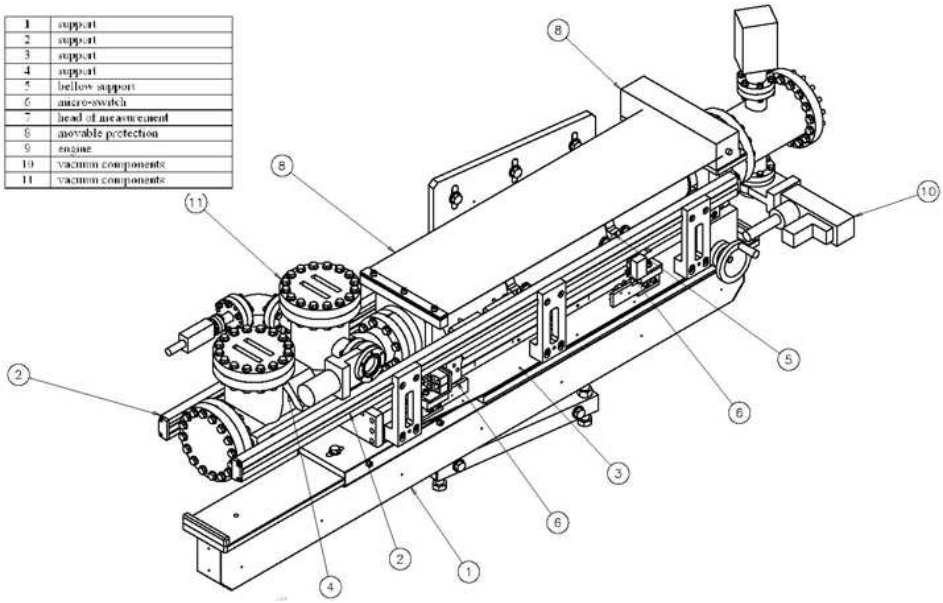

Figure 7.1: *DSX3 overview.*

The connection between the main line and the manipulators will be assured by a peek (insulating) support and vacuum bellow. The line can be ventilated by an electro-valve, remotely controlled. Ionivac instruments will provide pressure measurements for all the manipulators and in several crucial points of the main vacuum line. The system will be controlled by a *Labview* program, in which several interlock sensors will assure for a proper usage of the vacuum control system.

An overall overview of the new diagnostic and of its main parts is displayed in Fig.7.1. The instrument is sustained by a platform, directly connected to the RFX-mod main mechanical support. A custom 4-way cross connects the diagnostic to the main gate valve, and its flanges are devoted to the auxiliary pumping system.

The diagnostic consists mainly of three parts:

- the head of measurement;
- the linear actuator;

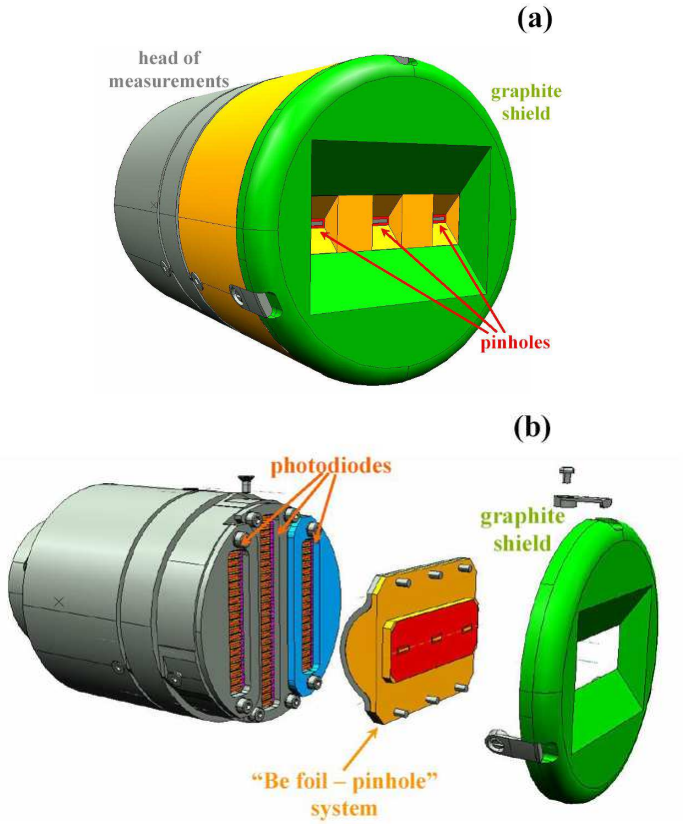

Figure 7.2: *Head of measurement: (a) cylindrical tube housing 65 photodiodes for SXR detection; (b) the "pinhole + Be foils" sandwich system, selecting the SXR energy range of radiation, is connected to the internal side of the aluminum lid, covered by the graphite shield.*

- a tube with flanges for collecting all the signals.

The head of measurement, housing the detector system, is sustained by a tube which allows for the alignment with the RFX-mod porthole, and which is connected to the UHV manipulator. This actuator permits to move the "tube+head" system horizontally, in order to put the instrument at its measurement position. The manipulator is a standard commercial UHV actuator (which can be controlled either manually or by means of a pressurized-air engine), which allows for positioning the head with an accuracy in the order of ± 0.1mm. On its backside, a large custom tube houses several flanges with vacuum feedthrough connectors for leading the signals, which come from the head and run into the tube of the manipulator bellow, up to air.

7.2.2 Head of measurement

The new SXR diagnostic camera consists of a cylindrical, 89mm-diameter stainless steel head, equipped with Silicon photodiodes for detecting the radiation emitted by the plasma. An external view of the head is illustrated in Fig.7.2(a). A graphite shield is mounted on the frontal plate of the head in order to protect it from the interactions with plasma and to guarantee the continuity of the RFX-mod graphite first-wall when the diagnostic is placed at its measurement position. A large opening in the plate permits the diodes to look at the plasma through three small pinholes, mounted on an internal support system [see Fig.7.2(b)]. In correspondence to the pinholes, curved Beryllium filters are installed on the backside of the frontal plate to select the SXR energy spectra.

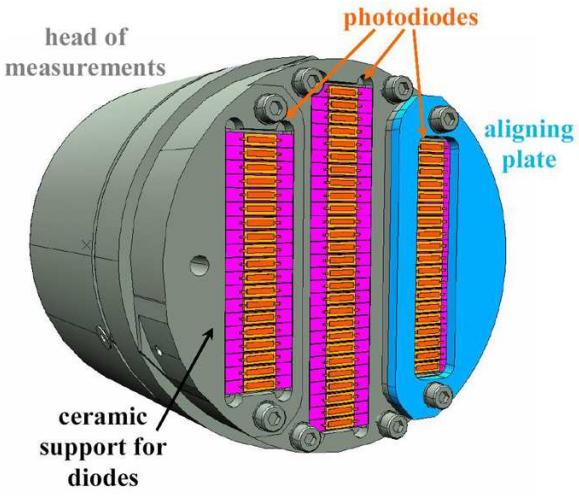

Figure 7.3: *Internal view of the head of measurements: 65 detectors are gathered into three row.*

Three groups of photodiodes are displaced in the internal part of the camera, for a total of 65 detectors (Fig.7.3): they are mounted on ceramic supports and fixed by covers in order to assure the alignment among them and in respect to the plane where the pinholes lie. The arrangement of the diodes, the Be foils and the pinholes, eventually, could be easily modified by replacing the ceramic supports and the Be foil-pinhole support. The diode displacement, as well as the possibility of placing in the head detectors with differ-

ent sizes, make this head a flexible instrument for testing a large variety of different detecting configurations.

Several LEDs will be installed close to the photodiodes, in order to remotely test the entire acquisition system without removing the diagnostic from its measurement position. Experience gained operating the in existence tomography system led to avoid the implementation of an additional cooling system because of the low temperature (estimated less than $100^{\circ}C$ from the SXR tomographic system) at which the camera operates in RFX-mod campaign experiments.

7.3 Pinholes and Be filters

In order to define a precise and limited region of observation, each diode looks at the plasma throughout a well-defined pinhole: the conjugation between the limited sizes of the detectors and those of the pinholes defines a settled plasma region of observation. Three different pinholes are needed, each one associated to each of the three groups of diodes. In correspondence of the pinholes, Beryllium filters acting as energy range selectors are mounted. The thickness of these three Be foils can be the same (and in particular if it is the same as those mounted on the three vertical tomographic manipulators it allows for enhancing the spatial resolution of the tomography) or different (permitting to look at the plasma in a different SXR energy range). A combined solution has been adopted. Two different groups of diodes (the central and an external one) look at the plasma throughout Be foils with the same thickness, while the remaining one has a thicker filter. That allows for obtaining both a higher spatial resolution in the SXR tomographic plasma emissivity reconstructions, and for allowing T_e calculation using the standard two-foil

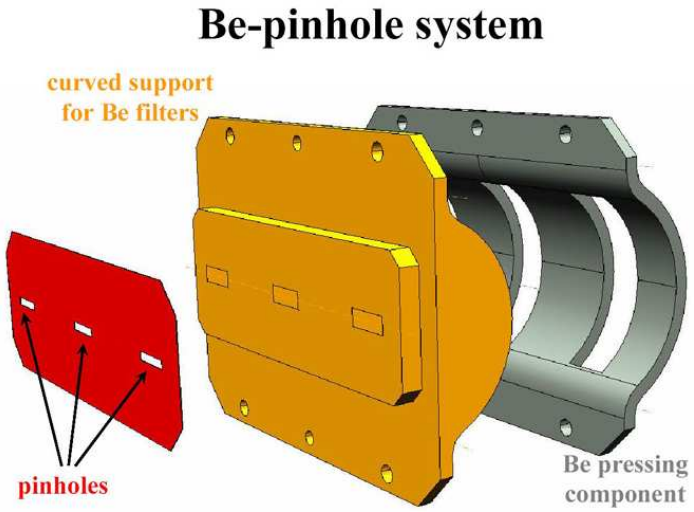

Figure 7.4: *Details of the Be foil-pinhole system.*

technique.

A detailed scheme of the Be foil-pinhole system is illustrated in Fig.7.4. It is a "sandwich" structure fixed in the Al frontal lid which is covered by a graphite shield. It consists of:

- an aluminum foil in which 3 pinholes are dug (the red foil);
- a stainless steel flared curved support for housing the filters, which is stuck to the frontal aluminum lid (the orange part);
- a curved Be-pressing part on the back in order to keep the Beryllium filters and the pinholes altogether and aligned (the grey component).

The Be foils housed in the middle of the "sandwich" structure (between the grey and orange components) have different thicknesses: two of them are 34μm thick (the same value of the Be installed in the SXR tomography), while the third one is 75μm-thick. All these foils respect the following requirements: thickness is measured with a maximum error of $\pm 1\mu$m, purity of 99.4% is assured as well as light tightness.

7.4 Detection system

DSX3 uses Silicon inverse polarized detectors proper to the measurements of the SXR radiation. They are custom made single diodes[1] (Fig.7.5(a)) which fulfill the following requests:

- UHV compatibility and usage in presence of variable magnetic fields;
- dark current less than $1nA$ @20°C;
- a bias Voltage can be implemented (5V);
- active area of 5.9mm$\times$1.1mm$=$ 6.49mm^2;
- Silicon thickness of 100μm, in order to detect photons in the range 10eV $\div$ 9keV;
- response time of about $10^{-8} \div 10^{-9}$s (compatible with the electronic band-width)
- SNR > 10

The detection system is composed of 65 diodes arranged side by side in three different rows (as in Fig.7.3), counting respectively 19, 27 and 19 detectors each. No diode array solution (with common anode or cathode) has been adopted to avoid the cross-talk among detectors and in order to reduce the electrical noise.

[1] I.R.D., http://www.ird-inc.com

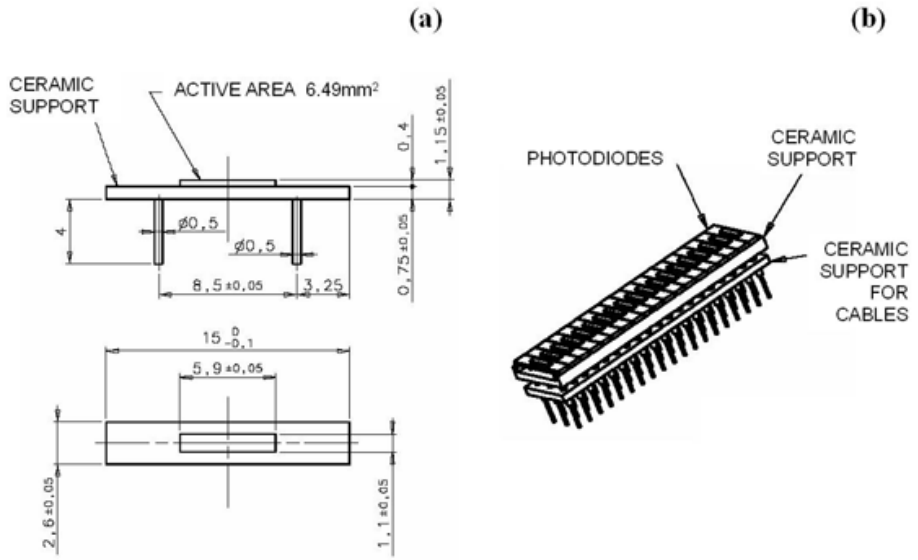

Figure 7.5: *(a) Drawings of a single custom made photodiode and (b) view of a 19 detector row as it looks like when diodes are mounted on the custom-made ceramic support system.*

This solution has been found out to be the less noisy one in various experimental devices, both for fusion studies [24, 69] and for other different applications [97], and of course, the most practical since each diode can be independently replaced in case of damage. The photodiodes are mounted on a UHV ceramic plate and sustained on the back side by supports which help in lining them up [see Fig.7.5(b) for an assemble of 19 diodes and their supports on the backside]. In the frontal side, each of the three groups of detectors is kept by a cover which helps in lining them up.

7.4.1 Geometry of the lines of sight

The combination of the three rows of photodiodes and the corresponding three pinholes define three regions of observation, which can be identified with the three planes, parallel each one to the others, determined by the fan of lines of sight (i.e. the cone axis) emanating from the three rows of the detectors. The three planes of observation are overlapping toroidally for most of the region. As a consequence, the three planes can be assumed to be a unique one, and so all the 65 diodes can be considered as looking at the same plasma cross-section. Actually, the dimensions of the region of observation in the toroidal direction make the three planes not perfectly overlapping, but the lines of sight associated to the one row of diodes are toroidally shifted of about 5-10 cm from those belonging to another plane. In such toroidal extension, no significant changes in the plasma column or in the localized SXR structures take place, so that the assumption that the three planes

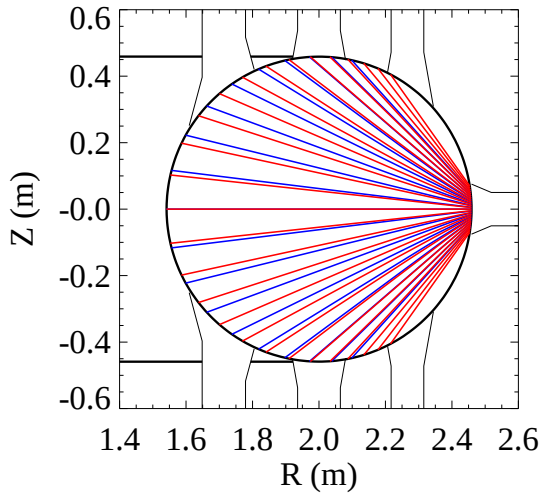

Figure 7.6: *Geometry of the lines of sight of DSX3 (at the tomography toroidal section of RFX-mod vessel) for the three rows of photodiodes: the red lines correspond to the 27 diodes of the central row, while the chords for the two external rows are perfectly overlapping (blue lines).*

are perfectly overlapping and the detectors look at the same plasma region can be stated. The geometrical features of the three groups of lines of sight in the poloidal plane (that is the toroidal cross-section at the SXR tomography) are illustrated in Fig.7.6. Because of the geometrical characteristics, the two rows of detectors with 19 diodes have exactly the same geometrical settings. In order not to have redundant measurements, these rows have been implemented with Be foils with different thickness. In this way, combining the SXR brightness from corresponding lines of observation and applying the two-foil technique, an estimation of the vertical electron temperature profile could be performed (the horizontal one is given by the multichord diagnostic in 3.4.1 and the Thomson scattering diagnostics [74]).

At the same time, the 19 measurements with the thinner foils can be combined with those of the row with 27 diodes (which look at the plasma throughout the same Be foil thickness) in order to have a total of 46 horizontal lines of observation of the plasma, distributed as they belong to a unique fan. They can be therefore implemented on the 57 signals coming from the SXR tomographic vertical manipulators, obtaining 103 lines of sight and measurements for tomographic SXR plasma emissivity reconstructions (the current number of lines of sight is 78), enhancing the spatial resolution of the diagnostic.

7.5 Electronics

The photo-current produced in the detectors impinged by plasma photons will vary (in dependence of the plasma conditions and the operational campaigns) in the

range between nA and μA. It must therefore be amplified and stored by a proper electronic chain. The signals are carried from the detectors to the amplification system by custom twisted cables, qualified for working in UHV. The two conductors carry the signals from the leads of the diodes, while their screen is connected to the ground. Additional graphite shields cover each of the conductors in order to reduce the noise caused by vibration. A similar type of cable has been adopted in the tomographic diagnostic already in existence on RFX-mod. Appropriate UHV feedthroughs work as passages from UHV up to air.

Amplifiers - *FEMTO DLPCA-200 Variable-Gain Transimpedance Amplifiers*[2]

The amplification system of the diagnostic consists in 65 FEMTO 200DLPCA amplifiers, placed in a cubicle near the experiment, and therefore remotely controlled. About half of them are single units while the remaining ones are more compact and inserted in 19" racks (200DLPCA-S). The gain range is between 10^5 and 10^9, with a bandwidth up to 50kHz at G=10^7; several gains can be set ($1\times$,$3\times$,$5\times$). This type of amplifiers has been successfully used in other diagnostics in RFX-mod, as they work ideally in DC measurements, with time resolved measurements down to the μs-region and as preamplifiers for photodiodes. Signals from the amplifiers are sent to the acquisition system placed far from the experiment.

Analog electronic - *YOKOGAWA Digitizer Modules*[3]

Analog signals from the amplifiers are acquired and stored by various YOKOGAWA Digitizer Modules, which are self contained, compact and plenty of memory modules. Their sampling rate is of 1MS/s, but there are several modules which have a sampling rate of 20MS/s. The high sampling rate is necessary to adequately acquire the high bandwidth analogical signals coming from the amplifiers and to allow analysis of high frequency fluctuations if signal level is large enough to require low gains. They have on board memory to store signals lasting at least 400ms at maximum sampling rate (that is the length of RFX-mod plasma pulse @1.5MA).

7.6 SXR measurement simulations

What can we expect from DXS3 SXR experimental signals?

Considering the SXR model as described in Apx.C, DSX3 brightness profiles can be simulated. Let us take a SXR emissivity simulated by matching the experimental signals of the present tomography diagnostic: it is possible to calculate the line-integrated measurements that will be obtained in DSX3. In Fig.7.7 the DSX3 SXR profiles are displayed for a simulated plasma emissivity as in panel (a), where a symmetric distribution is considered, without any localized more emissive region

[2] http://www.femto.de/index.html

[3] http://www.yokogawa.com/it/

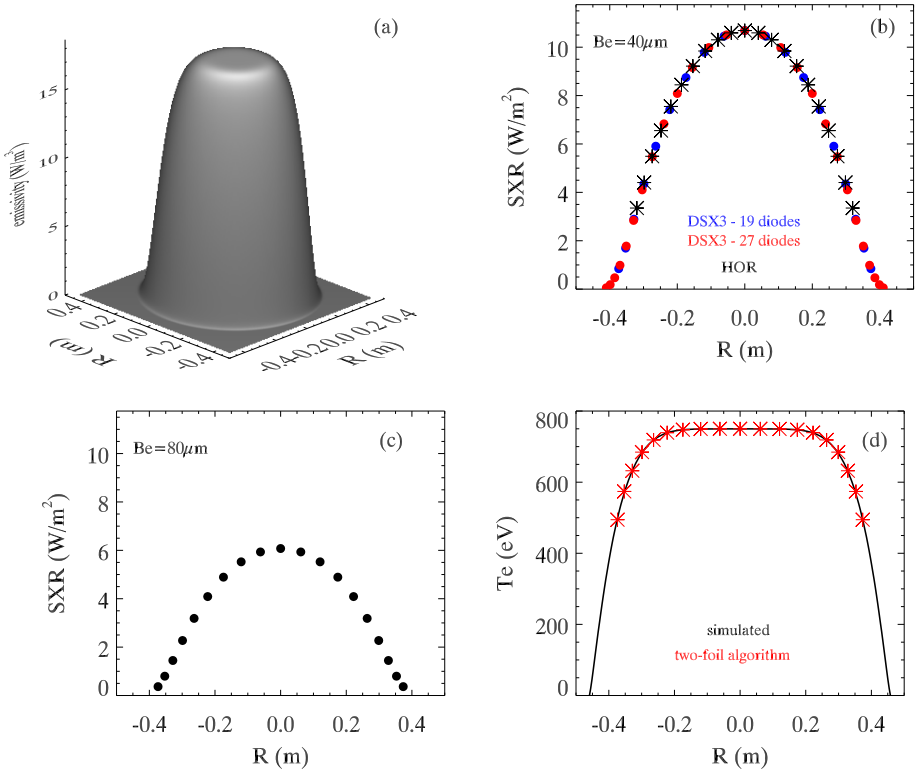

Figure 7.7: *(a) SXR emissivity profile for the simulation; (b) SXR brightness profiles for those rows of DSX3 with the same Be thickness (blue and red circles) and for the present SXR tomography (black stars); (c) profile for the 75μm-thick Be foil; (c) T_e profile simulated (black line) and calculated with the double-foil technique (red stars).*

(MH state). In Fig.7.7(b), the horizontal emissivity profile obtained for the two rows of diode using the 34μm Be foils (the central and an external one) are displayed (red and blue full circles): $19+27$ measurements in spite of the 21 of the present SXR tomography (which are superimposed with black stars). In Fig.7.7(c), the brightness profile with 75μm thickness of the Be filter has lower values (due to a different energy range considered), but a similar shape of those in (b). The brightness ratio for measurements with corresponding impact parameters p, that is the blue circles in (b) and the black circles in (c), leads to the T_e profile estimation with the double-foil technique [see Fig.7.7(d), red stars]. The estimated T_e measurements from the simulated signals are well superimposed to the temperature profile simulated in the model for the emissivity distribution in (a), here represented by the black line.

APPENDIX A

Tomographic algorithms for SXR reconstructions

A.1 Analytical solution of the inversion problem

Let us consider a cross-section of a toroidal vacuum vessel where plasma for fusion research is confined. The SXR emissivity distribution g is a function of two variables, $g = g(r,\theta)$, where $0 \leq r \leq 1$, and $0 \leq \theta \leq 2\pi$, as illustrated in Fig.A.1. A photodiode detector in proximity of the plasma edge and looking at the plasma throughout a small pinhole is impinged by radiation inside the volume defined by the diode and the pinhole sizes. The axis of the volume so defined (a cone) is called ***line of sight*** L (or chord). This chord can be univocally identified in the (r,θ) plane by two parameters: the impact factor p, that is the distance of the line of sight from the center of the vessel, and ϕ, being the angle between p and the equatorial plane. The relation between the experimental measurements f and the emissivity g is a transformation between the (r,θ) and the (p,ϕ) plane, through this equation:

$$f(p,\phi) = \int_{L(p,\phi)} g(r,\theta)\, \mathrm{d}l \tag{A.1}$$

Since the f function can be only partially sampled, various approximated solution techniques have been developed; in plasma physics, the most important are the following ones.

Finite element method. It is based on the approximation of the integral in Eq.(A.1) as a sum over each of the lines of sight, assuming a constancy of the plasma emissivity g inside defined regions called *pixel*, which can be defined to have

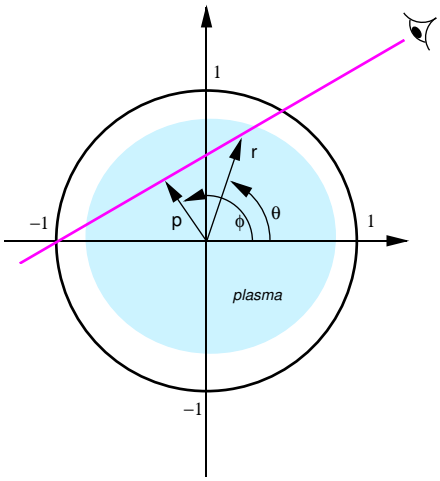

Figure A.1: *Scheme of a line of sight geometry in a poloidal cross-section. The line of sight L is determined by the impact parameter p and by the angle ϕ.*

various shapes. The Eq.(A.1) becomes a matrix equation $\mathbf{f} = \mathbf{W} \cdot \mathbf{g}$, where $\mathbf{f}$ represents the vector of the measurements, and $\mathbf{g}$ the vector of the unknown SXR emissivity. The solution is found by means of various methods, which could be iterative or not.

Analytical solution. It is the main object of this Appendix, and it will be illustrated in details in the following paragraphs. This method is optimum for the reconstructions of $m = 1$ SXR structures, as in the RFP plasmas.

Hybrid method. The radial dependence of the emissivity is discretized, that means plasma is considered as nested circular regions. The angular dependence instead is developed over angular harmonics. The advantage of this method is the possibility to introduce into the computation a large number of a priori information coming from other diagnostics.

A.1.1 Analytical solution method

The finite number of the experimental measurements f of the SXR plasma emissivity g does not prevent from having information on the emissivity, but defines only its resolution.

In the '60s, A.M. Cormack proposed a decomposition of $g(r,\theta)$ and $f(p,\phi)$ over the Fourier series:

$$\begin{aligned} g(r,\theta) &= \sum_{m=0}^{+\infty} \left(g_m^c(r)\cos(m\theta) + g_m^s(r)\sin(m\theta)\right) \\ f(p,\phi) &= \sum_{m=0}^{+\infty} \left(f_m^c(p)\cos(m\phi) + f_m^s(p)\sin(m\phi)\right) \end{aligned} \tag{A.2}$$

where the Fourier transforms are given by:

$$\begin{aligned} g_m^{c,s}(r) &= \frac{1}{2\pi}\int_0^{2\pi} g(r,\theta)\ (\cos(m\theta),\sin(m\theta))\ \mathrm{d}\theta \\ f_m^{c,s}(p) &= \frac{1}{2\pi}\int_0^{2\pi} f(p,\phi)\ (\cos(m\phi),\sin(m\phi))\ \mathrm{d}\phi \end{aligned} \tag{A.3}$$

Cormack proved that the bi-dimensional problem of inversion of Eq.(A.1) can be reduced to a system of 1-dimensional integral equations:

$$f_m^{c,s}(p) = 2\int_p^1 \frac{g_m^{c,s}(r)\ \arccos(p/r)\ r\ \mathrm{d}r}{\sqrt{r^2-p^2}} \tag{A.4}$$

being r and p positive numbers but lower than 1 (normalized coordinates).

Cormack proved that for a given f_m harmonic there is a unique correspondent g_m. The introduction of the Tchebycheff polynomials of the first type, $T_m(x) = \cos(m\arccos(x))$, which is a polynomial function of the first order in x, allows for determining the solution for the $g_m(r)$ harmonic as a function of the f_m harmonic:

$$g_m^{c,s}(r) = -\frac{1}{\pi}\frac{\mathrm{d}}{\mathrm{d}r}\int_r^1 \frac{f_m^{c,s}(p)\ T_m(p/r)\ p\ \mathrm{d}p}{p\ \sqrt{p^2-r^2}} \tag{A.5}$$

In particular, if $m = 0$, $T_0(p/r) = 1$, and the Eq.(A.5) is reduced to an Abel inversion. This equation is however not useful, due to the presence of a singularity at $p = r$.

Eq.(A.5) implies that to solve the m-th angular harmonic of the emissivity g is needed only the m-th poloidal harmonic of the brightness f. The first Fourier harmonics of the brightness are sufficient to reconstruct the correspondent emissivity harmonics. However, the existence of the mathematical solution does not imply it can be determined practically. Experimentally, in fact, the brightness f cannot be sampled completely, but only in a finite number of measurements. Thus the limited resolution in sampling f relapses thus in a limited resolution of the emissivity g. The finite number of experimental measurements is therefore a limit in the inversion problem solution: in order to reconstruct $m+1$ angular (poloidal) harmonics, the $f(p,\phi)$ function must be detected for $2m$ values of significant different ϕ (similarly to the Nyquist-Shannon sampling theorem).

Singularity in Eq.(A.5) can be overcome by expanding the harmonics of the emissivity function g in terms of a polynomial system:

$$g_m^{c,s}(r) = \sum_{l=0}^{\infty} a_{ml}^{c,s}\ R_{ml}(r). \tag{A.6}$$

A.1.2 Zernicke polynomials

The first orthonormal base system historically adopted for Eq.(A.6) was the Zernicke polynomials:

$$R_{ml}(r) = \sum_{s=0}^{l} \frac{(-1)^s\ (m+2l-s)!}{s!\ (m+l-s)\ (l-s)}\ r^{m+2l-s}, \tag{A.7}$$

which allow for easily solving the integral Eq.(A.4), and give an analytical expression for the $f_m^{c,s}(p)$ functions which depend on the $a_{ml}^{c,s}$ coefficients [6]:

$$f_m^{c,s}(p) = \sum_{l=0}^{\infty} a_{ml}^{c,s} \frac{2}{m+2l+1} \sin[(m+2l+1)\arccos(p)]. \tag{A.8}$$

The numerical solution is obtained by truncating the series in Eq.(A.2) and making the sum over a finite number of terms:

$$g(r,\theta) = \sum_{m=0}^{M} \sum_{l=0}^{L} [a_{ml}^{c} \cos(m\theta) + a_{ml}^{s} \sin(m\theta)] \; R_{ml}(r). \tag{A.9}$$

The unknown coefficients a_{ml} are obtained by inserting Eq.(A.9) into $f(p,\phi)$, so that:

$$\begin{aligned} f(p,\phi) \;\; = \;\; & \sum_{m=0}^{M} \sum_{l=0}^{L} [a_{ml}^{c} \cos(m\phi) + a_{ml}^{s} \sin(m\phi)] \; \times \\ & \times \frac{2}{m+2l+1} \sin[(m+2l+1) \; \arccos(p)]. \end{aligned} \tag{A.10}$$

If we have M measurements of f, corresponding to M lines of sight (p,ϕ), Eq.(A.10) allows for writing a system of M linear equation in the N unknown a_{ml} coefficients, which are in number $2(M+1)(N+1)$. In matrix way,

$$\mathbf{f} = \mathbf{W} \cdot \mathbf{g}, \tag{A.11}$$

being $\mathbf{f}$ the M-dimension vector (its components are the measured brightnesses); $\mathbf{W}$ is a matrix, mostly rectangular, which depends on the line of sight geometrical settings; and $\mathbf{g}$ is made of the a_{ml} coefficients. This vector is obtained by inversion of Eq.(A.11), so that:

$$\mathbf{g} = \mathbf{W}^{-1} \cdot \mathbf{f}. \tag{A.12}$$

The tomographic inversion problem is thus transformed into the computation of the inverse matrix $\mathbf{W}^{-1}$.

A.1.3 Singular Value Decomposition

As stated above, the analytical solution of the inversion problem is reduced to the solution of a system of M linear equation in N unknowns, where $M > N$ [61]. If no experimental errors enter the measurements, only N equation could be considered; but this is not our case.

Generally the vector $\mathbf{g}$ is found by minimizing the vector:

$$\mathbf{r}_2 = ||\mathbf{W} \cdot \mathbf{g} - \mathbf{f}|| = \sqrt{\sum_i (\mathbf{W} \cdot \mathbf{g} - \mathbf{f})_i}. \tag{A.13}$$

That allows for determining the most probable solution if the experimental errors have a Gaussian distribution. The minimum solution is obtained using the Singular Value Decomposition (SVD) of the matrix **W**:

$$\mathbf{W} = \mathbf{U} \cdot \mathbf{S} \cdot \mathbf{V}^T, \tag{A.14}$$

being:

- **U** is a $M \times N$ matrix, whose columns are orthogonal;
- **S** is a diagonal matrix, where $S_{ii} = w_i$ are singular eigenvalues of the matrix **W**;
- **V** is a orthogonal matrix $N \times N$

The solution minimizing the "l-norm" is [98]:

$$\mathbf{g} = \left(\mathbf{V} \cdot \mathbf{S}^{-1} \cdot \mathbf{U}^T\right) \cdot \mathbf{f} = \mathbf{H} \cdot \mathbf{f}. \tag{A.15}$$

The $\mathbf{S}^{-1} = \mathrm{diag}(1/w_i)$ is a diagonal matrix made of the inverse of the singular eigenvalues. The **H** matrix is called "generalized inverse" or *pseudo-inverse*. The singular eigenvalues contain information on the spatial resolution of the tomographic system. If the eigenvalues are very small or equal to zero, the basic orthogonal functions cannot be determined by the settings of the detection system considered, because there are several combination of groups of emissivity functions g producing similar measurements. The problem is ill-posed. So, generally the small eigenvalues are not taken into account, because they render the solution full of oscillation: in the determination of the **H** matrix only the bigger w_i eigenvalues are used, fixing a threshold (svd_{tol}) under which all the eigenvalues are set equal to zero.

This method however does not allow for introducing a priori constraints into the solutions, which could therefore result even negative. Further information on this decomposition can be found in [61].

A.1.4 Analytical method: advantages and drawbacks

The analytical method for the solution of the inverse problem has a lot of advantages with respect to the finite element technique. Among them the assumption of the truncated Fourier and Zernicke series: the spatial resolution is the best attainable with the geometry of the detection system used. Moreover, this method minimizes the electronic noise entering the algorithms, since the unknown a_{ml} coefficients are determined over a minimum square fit.

This method, however, could produce results which could be lacking of physical meaning, being oscillating or negative. Thus the necessity for forcing constraints (e.g the positivity of the SXR emissivity g) which render the solution matrix algorithms more complicated. In addition, null additional chords are needed in

correspondence to the plasma edge to force the emissivity to be equal to zero, thus obtaining a reconstructed SXR emissivity being regular, positive and without oscillations (*regularization process*). This constraint calls for minimizing the gradients of the reconstructed emissivity: high possible oscillations present in the solution are not acceptable because the sampling number of the brightnesses cannot resolve rapid spatial variations in the emissivity distribution. However the regularization method does not completely remove the possible negative values of the emissivity. Usually this is removed by means of the "maximum entropy" technique (for details, see [99]). This technique is however not used for the SXR plasma emissivity distribution reconstructions for the RFX-mod and MST experiments.

A.2 Bessel functions

As asserted above, the analytical solution of the 2-dimensional inverse problem asks for the introduction of regularization methods, among which is to force to zero the SXR emissivity at the plasma edge, introducing fictitious null chords. This avoids the oscillation artifacts entering the SXR emissivity distribution due to the intrinsic behavior of the R_{ml} Zernicke polynomials used for the radial decomposition in proximity of the edge: $R_{ml}(1) = 1$.

An alternative solution has been investigated and developed, consisting in replacing the Zernicke polynomials $R_{ml}(r)$ in Eq.(A.6) with the Bessel functions of the first kind $J_m(x_{ml}(r))$, being x_{ml} the lth zero of the mth order Bessel function $J_m(z)$ [100, 101]. These functions are a complete system for the decomposition of g:

$$g_m^{c,s}(r) = \sum_{l=0}^{\infty} a_{ml}^{c,s} \, J_m(x_{ml} r) \tag{A.16}$$

which presents a better behavior in correspondence to the plasma edge.

Since it is hard to obtain the analytical form of $f_{ml}^{c,s}(p,\phi)$, it is better to obtain it by the numerical integration of

$$f_{ml}(p) = 2 \int_p^1 \frac{J_m(x_{ml} r) \; T_m(p) \; r \; \mathrm{d}r}{\sqrt{r^2 - p^2}}. \tag{A.17}$$

Zeros of the Bessel function are also obtained by the use of numerical calculation. The character that $J_m(x_{ml} r)$ is zero at the boundary is consistent with the the fact that the emissivity goes to zero approaching $r = 1$. Moreover, $J_m(x_{ml} r)$ has l zeros in (0,1), and the density of zeros is almost uniform in (0,1): all these characters render the Bessel function a better orthonormal set of base functions rather than the Zernicke polynomials.

Considering the properties of the Bessel functions, a simplified expression of

Eq.(A.8) is obtained:

$$f_{ml}^{c,s}(p) = -J'_m(x_{ml}) \int_0^{\infty} \mathrm{d}\theta \cos(m\theta) \sin(x_{ml}|\cos\theta - p|) \quad \text{(A.18)}$$

$$= -2J'_{ml}(x_{ml}) \int_0^{\cos^{-1} p} \mathrm{d}\theta \cos(m\theta) \sin[x_{ml}(\cos\theta - p)]. \quad \text{(A.19)}$$

Further simplifying this equation, it is possible to obtain [102]:

$$f_{ml}^{c,s}(p) = -2\sqrt{1-p^2}\, J'_{ml}(x_{ml}) \times \sum_{n=0,m\neq n}^{\infty} \delta_n J_n(x_m l) \sin\left(n\frac{\pi}{2}\right) \left(\frac{U_{m+n-1}(p)}{m+n} \frac{U_{m-n-1}(p)}{m-n}\right), \quad \text{(A.20)}$$

being $\delta_0 = 1/2$ for $n = 0$, and $\delta_n = 1$ for $n \neq 0$; U_m(p) represents the Tchebychev polynomials of the second kind $U_m(p) = \sin[(m+1)\arccos(p)]/\sqrt{1-p^2}$. The advantage of using the Tchebychev polynomials lies in the fact that $U_m(p)$ is obtainable with a recursion relation, $U_{m+1}(p) = 2pU_m(p) - U_{m-1}(p)$, being $U_0(p) = 1$ and $U_1(p) = 2p$.

APPENDIX B

SXR radiation in fusion plasma devices

B.1 Bremsstrahlung radiation

In a plasma with an arbitrary fully stripped ionized atomic species, if recombination contribution is negligible, the emitted radiation is due to the deflection of free electrons in the electrostatic field of the ions. Up to temperature lower than 50keV (above this value, relativistic effect cannot be avoided), mostly all the radiation comes from this kind of electron-ion interactions, called *bremsstrahlung* (in German language, it means "breaking radiation"). As they are heavier than electrons, in practice ions do not move during the interactions, while electrons are accelerated but remaining free (bremsstrahlung is also known as free-free radiation). In a semi-classic theory (we can avoid the quantum approach because it is different from the semi-classic one only for the presence of a multiplicative factor, the so-called *Gaunt factor* [103]), the radiation power of a charge q accelerated is given by the Larmor equation:

$$P = \frac{2}{3}\,\frac{q^2}{4\pi\varepsilon_0 c^3}\,\left(\frac{\mathrm{d}\mathbf{v}}{\mathrm{d}t}\right)^2 \tag{B.1}$$

In a fusion plasma, an electron can be accelerated both from magnetic fields (synchrotron radiation) and from the electrostatic field generated by an ion significantly close to the electron itself (bremsstrahlung). In the former case, the electron is under the influence of the Lorentz force:

$$\mathbf{f} = -e\,(\mathbf{E} + \mathbf{v}\times\mathbf{B}) \tag{B.2}$$

In a fusion plasma, the electric field $\mathbf{E}$ is negligible, so that the previous equation

can be reduced to:

$$\mathbf{f} = -e\,\mathbf{v}\times\mathbf{B} \tag{B.3}$$

By using Eq.(B.1) and integrating among a maxwellian distribution of the velocities, the power equation becomes:

$$P = \frac{e^4}{3\pi\varepsilon_0\, m_e^3\, c^3}\, B^2\, n_e\, T_e \tag{B.4}$$

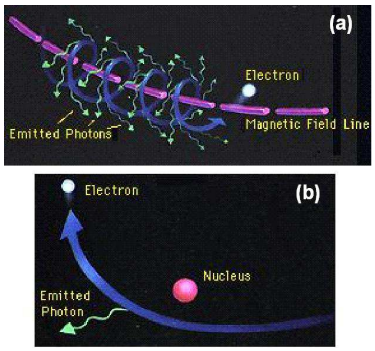

Figure B.1: *Cartoons of the synchrotron (a) and bremsstrahlung (b) radiation.*

The dependence on the magnetic field implies that the emissivity is higher in a Tokamak than in a RFP device. In any case, this is not the power emitted by plasma, since it absorbs radiation at the cyclotron frequency $\omega_c = (e\mathrm{B})/m_e$. This corresponds to a wavelength of the centimeter for magnetic fields of about 1 Tesla, generally from the microwave length range up to far infrared, which is partially re-absorbed by the plasma itself.

Bremsstrahlung radiation, instead, is in the SXR energy range, to which plasma is completely transparent, and so this radiation is lost. If a classic approach is considered, for a $Z\cdot e$ charge ion (not moving, with an endless mass), and an electron e moving at a v velocity with a b impact parameter (see Fig.B.1) we will have:

$$m_e\frac{\mathrm{dv}}{\mathrm{dt}} = \frac{Ze^2}{4\pi\,\varepsilon_0\, b^2} \tag{B.5}$$

Introducing this formula in Eq.(B.1), the power obtained is:

$$P = \frac{2}{3}\left(\frac{e^2}{4\pi\varepsilon_0}\right)^3 \frac{Z^2}{m_e^2 c^3 b^4}. \tag{B.6}$$

The energy emitted in a single collision (if the assumption that the electron remains in proximity of the ion for $t = 2b/\mathrm{v}$ is considered) is $E = P(2b/\mathrm{v})$. The number of collision per unit volume is $n_e\, n_i\, 2\pi\,\mathrm{v}\, b\, \mathrm{d}b$; the power emitted density becomes $\mathrm{d}P = E\; n_e\; n_i\; (\mathrm{v}\; 2\pi\; b\; \mathrm{d}b)$; and the total power per unit volume is obtained by integrating over the impact parameters:

$$P = \left(\frac{e^2}{4\pi\varepsilon_0}\right)^3 \frac{2n_e n_i\, Z^2}{3m_e^2 c^3} \int_{b_{min}}^{\infty} \frac{4\pi}{b^2}\,\mathrm{d}b. \tag{B.7}$$

The estimation for b_{min} derives from the Heisenberg principle, so that $b_{min} \approx \hbar m_e \mathrm{v}$. And if the velocity distribution is a maxwellian function, $(1/2)m_e\mathrm{v}^2 = (3/2)T_e$, the density power becomes:

$$P \;\approx\; \frac{8\pi}{\sqrt{3}}\left(\frac{e^2}{4\pi\varepsilon_0}\right)^3 \frac{n_e n_i\, Z^2 T_e^{1/2}}{m_e^{3/2} c^3 \hbar}. \tag{B.8}$$

In presence of various atomic species, the concept of Z_{eff} has to be introduced:

$$Z_{\text{eff}} = \frac{\sum_i n_i Z_i^2}{n_e}, \tag{B.9}$$

which leads to the following equation for the density power:

$$P \approx \frac{8\pi}{\sqrt{3}} \left(\frac{e^2}{4\pi\varepsilon_0}\right)^3 \frac{n_e^2 Z_{\text{eff}} T_e^{1/2}}{m_e^{3/2} c^3 \hbar}. \tag{B.10}$$

By introducing the quantistic multiplicative constant and expressing the temperature in eV, it becomes:

$$P = 1.689 \cdot 10^{-38} n_e^2 Z_{\text{eff}} T_e^{1/2} \frac{\text{W}}{\text{m}^3}. \tag{B.11}$$

The spectral distribution can be derived by considering the radiation per unite volume (in classical theory), in the range E and E+dE, which is given by the Boltzmann distribution:

$$\text{d}P \propto n_e^2 Z_{\text{eff}} \frac{\text{e}^{-E/T_e}}{T_e^{1/2}}. \tag{B.12}$$

The maximum of this function, obtained in fusion plasmas for T_e of about 1keV, corresponds to the maximum energy in the SXR range, with wavelength of about 0.6 nm. The dependence of P on Z_{eff} implies that at medium-high Z number ions, the emissivity is much higher: it is necessary to maintain at low level the presence of the impurities inside the plasma. In Fig.B.2, the bremsstrahlung emitted power with $Z_{\text{eff}} = 1$ is displayed at various temperatures T_e.

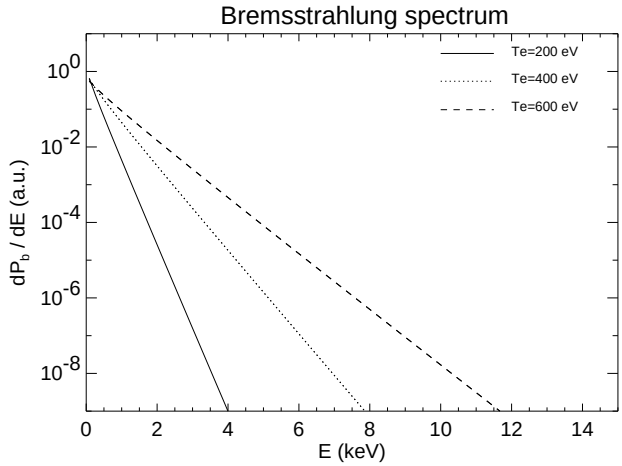

Figure B.2: *Power bremsstrahlung emissivity per unit volume, for different electron temperatures T_e, as in Eq.(B.12) with $Z_{\text{eff}} = 1$.*

B.2 Line radiation

This contribution to plasma radiation is linked to the presence of partially ionized ions inside the plasma, with the fully strip ionization energy higher than the thermal one. These ions come from the internal wall of the experimental devices: they can be metals, like Aluminum coming from the MST internal wall, or Carbon due to the graphite internal wall in RFX-mod.

Other important impurities are Oxygen and Nitrogen, which can bound to the atoms of the wall when the device is "in air" during the shut-down. In this case, focused wall treatments have to be performed to reduce the impurity quantities trapped into the internal wall: the baking procedure (the vacuum vessel is heated to about 100-150°C in order to make the impurities ejected from the wall itself), or the deposition of low Z atoms over the wall like Boron or Beryllium to reduce the presence of Oxygen or Carbon trapping into the wall.

Impurities can be elastically or not elastically bumped from electrons or other high energy particles, so that the kinetic energy can excite one or more electrons bounded to the ion. In the following process of de-excitation, radiation at definite and specific frequencies is emitted, called *line radiation*. The emissivity spectrum of this kind of radiation is very complex, and the electrons do not distribute in a maxwellian function in the various energetic bounded levels. It depends on a large variety of parameters (such as the electron temperature, the impurities transport, the scattering processes of the various atomic species). Analysis of the contribution of this kind of radiation requires a numerical determination of the distributions by

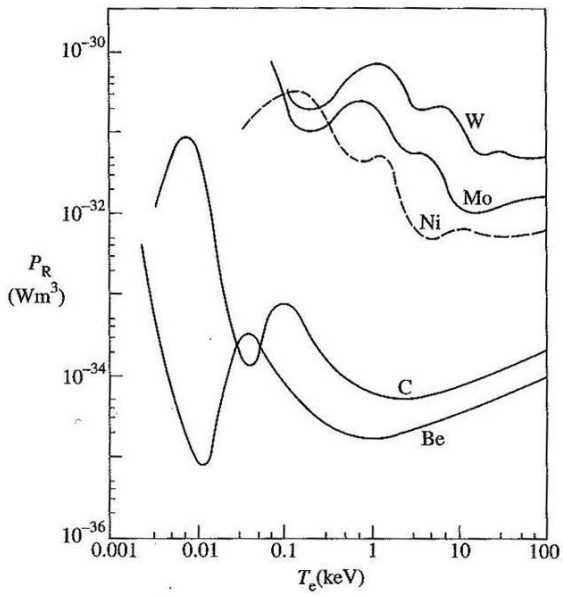

Figure B.3: *The total radiated power function P_R is shown as a function of temperature for various elements.*

means of the atomic physics processes in transport (collisional-radiative model). If the assumption of the negligibility of the impurity transport is done, line radiation depends only on temperature and density:

$$P_{line} = n_i \, n_e \, P_R(T_e) \tag{B.13}$$

where n_e and n_i are the electron and ion density, respectively; and $P_R(T_e)$ is a temperature function. These P_R functions have an absolute maximum but also relative maximum points. At low Z numbers, the absolute maximum is at low temperature, above which line radiation is quite completely reduced. An example of the radiated power is displayed in Fig.B.3 as a function of temperature. At higher temperature, electrons are subsequently removed from impurity; at high Z numbers, the maximum of the P_R functions is at higher temperatures, and impurities are not fully stripped. By these considerations, the quantity of high Z atoms should be reduced as much as possible even in fusion reactors.

B.3 Recombination step contribution

This is a continuum contribution due to the interaction between a free electron and an ion, capturing it, with the resulting emission of the exceeding energy in form of radiation. In an hydrogen plasma, recombination is only a negligible contribution to the bremsstrahlung (if temperature is not so low). However, in presence of partially ionized impurities, there are emissive thresholds, linked to the energetic levels of the ions capturing the electrons. If several impurity species are present, the spectrum dependence becomes very complex, and a formula summarizing all the ionization levels can be used:

$$\zeta(T_e, Z_{\text{eff}}) = Z_{\text{eff}} + \frac{\sum_i n_i Z_i^2 F_i(\chi_i, T_e)}{n_e} \tag{B.14}$$

This ζ factor, called *enhancement factor*, replaces Z in Eq.(B.12), and can have large values (even about several tenths) for low temperatures.

APPENDIX C

Modeling of the SXR plasma emissivity

A model for reproducing the SXR plasma emissivity distribution and the detecting system (Beryllium foil and photodiode) has been developed. The aim of this modeling has been essentially:

- to give an estimation of the power impinging onto the detector for a particular geometrical setting of a detection system. That allowed for the estimation of the SXR signals in various configuration settings;
- to allow for reproducing the SXR plasma emissivity when tomographic reconstructions are not available. In this case, information on the electron temperature and density profiles are given.

This model has also been used in the past to study the optimal geometrical setting of the detection system in the realization of several instruments for SXR measurements for tomographic reconstructions or for T_e estimation.

C.1 SXR model

The photo-current produced by the detectors while impinged by radiation is:

$$\int_0^\infty \mathrm{d}E \int_V \frac{\mathrm{d}P(\mathbf{r})}{\mathrm{d}E} A(E)\, T_{Be}(E,t)\, \frac{\mathrm{d}\Omega}{4\pi}\, \mathrm{d}\mathbf{r} \tag{C.1}$$

where V is the plasma volume observed; $\mathrm{d}P(\mathbf{r})/\mathrm{d}E$ is the spatial distribution (per unit volume) and the energy distribution of the bremsstrahlung radiation; $A(E)$ the absorption coefficient of the silicon diode; T_{Be} the transmission function of the Be foil; $\mathrm{d}\Omega/4\pi$ the fraction on which each element dr looks the detector. In $dP(r)/dE$,

it is necessary to explicit the dependence on density n_e and temperature T_e, and on the effective charge Z_{eff}. If this is considered to be constant along the plasma radius (as it is confirmed in [67]), Z_{eff} can be gathered in multiplicative constant k, so that Eq.(C.1) for the only bremsstrahlung becomes:

$$\frac{\mathrm{d}P}{\mathrm{d}E} = k \cdot n_e^2 \, \frac{\mathrm{e}^{-E/T_e}}{\sqrt{T_e}}. \tag{C.2}$$

A further assumption admits only a radial dependence of the remaining quantities in the poloidal section of the plasma vessel, avoiding a dependence on the poloidal angle θ (that is symmetric emissivity distribution),

$$T_e(r) = T_e(0)\left[1-\left(\frac{r}{a}\right)^{\alpha}\right]^{\beta} \tag{C.3}$$

$$n_e(r) = n_e(0)\left[1-\left(\frac{r}{a}\right)^{\gamma}\right] \tag{C.4}$$

in which α, β and γ are variables to be set. So, the SXR measurement is given by:

$$k \int_V \frac{\mathrm{d}\Omega}{4\pi}\mathrm{d}\mathbf{r} \int_0^{\infty} \mathrm{d}E \, \left(\frac{n_e^2}{\sqrt{T_e}} \, \mathrm{e}^{-E/T_e} \, A(E) \, T_{Be}(E,t) \right). \tag{C.5}$$

The constant k gathers all the constant factors of the previous relations.

The plasma region observed by each detector is defined by the finite dimensions and the positions of the photodiode itself and of the correspondent pinhole: it is a volume (a cone) whose axis is the so-called *line of sight, L*. If this volume is small enough to consider no emissivity distribution variation inside it in the direction perpendicular to the line of sight, the cone can be identified with its axis, and the volume integral in Eq.(C.5) can be reduced to a line integral multiplying a factor f_g, which depends on the geometrical features of the detectors and the pinholes. In this way, Eq.(C.5) becomes:

$$k \int_L \mathrm{d}\mathbf{r} \int_0^{\infty} \mathrm{d}E \, \left(\frac{n_e^2}{\sqrt{T_e}} \, \mathrm{e}^{-E/T_e} \, A(E) \, T_{Be}(E,t) \right), \tag{C.6}$$

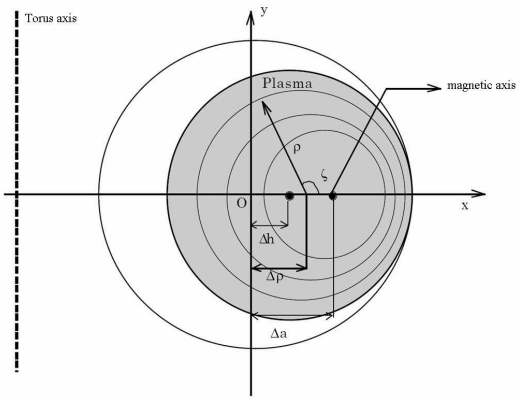

Figure C.1: *Schematic view of the flux-surface coordinate system used in the SXR model.*

where the geometrical factor f_g is gathered into the constant k.

This model is developed in the coordinates of the flux surfaces (see Fig.C.1): they are supposed to be circular and nested, and it is possible to introduce an horizontal shift Δa of the magnetic axis, and Δh of the last closed flux surface. The radius ρ of the flux surfaces, whose center is shifted of $\Delta\rho$ with respect to the center O of the vessel, is in between 0 and $1-\Delta h$. $\Delta\rho$ is supposed to be a quadratic dependence on the radius ρ:

$$\Delta\rho(\rho) = C_0 + C_1\rho + C_2\rho^2. \tag{C.7}$$

The coefficients (C_0, C_1, C_2) are found by using these considerations:

$$\Delta\rho(\rho = 0) = \Delta a \tag{C.8}$$

$$\Delta\rho(\rho = 1-\Delta h) = \Delta h \tag{C.9}$$

$$\frac{d\Delta\rho}{d\rho}(\rho = 0) = 0 \tag{C.10}$$

So, in the integral C.1, each point of the lines of sight L is univocally associated to the point belonging to the flux surface with a radius ρ.

In this thesis, various SXR emissivity distributions have been modeled, for different SXR diagnostic in different RFP devices. For each experiments, the real parameters of the detection system (Be foils and Silicon diode thickness) have been considered, as well as the T_e, n_e and Δa measurements coming from other diagnostics (whenever available). The remaining information for obtaining the SXR emissivity have been determined by fitting the simulated measurements and the experimental SXR brightness profiles (it means to find out the best coefficient α, β, γ and $T_e(0)$ in Eqs.C.3 and C.4). The parameters are selected by computing iteratively and comparing the simulations and the experimental measurements, thus obtaining the best set of fitting parameters.

C.2 Modeling of SXR localized structures

Sometimes, the symmetric T_e profile as in Eq.(C.3) is not enough for matching experimental brightness in case of QSH plasmas. In fact, in this case, the localized SXR structure emerging in the plasma core is associated to a localized thermal island (see §5.2.2 for instance). This T_e island must be introduced into the model. A localized structure can be added to the $T_e(r)$ profile: it is assumed to have a ΔT_e value, centered in $r0$ and with a radial dependence given by a Gaussian function. The poloidal dependence is given by a Gaussian function too. In this way, a bean-like structure in the T_e profile becomes a bean-like island in the SXR emissivity distribution. An example of the temperature profile as computed in the model is displayed in Fig.C.2: the thermal island is given as a ΔT_e structure, radially positioned at r_{Te}, with a FWHM radial width of Δr_{Te} (orange line), and is superimposed to the symmetric profile (black line); similarly, in the poloidal direction, a gaussian

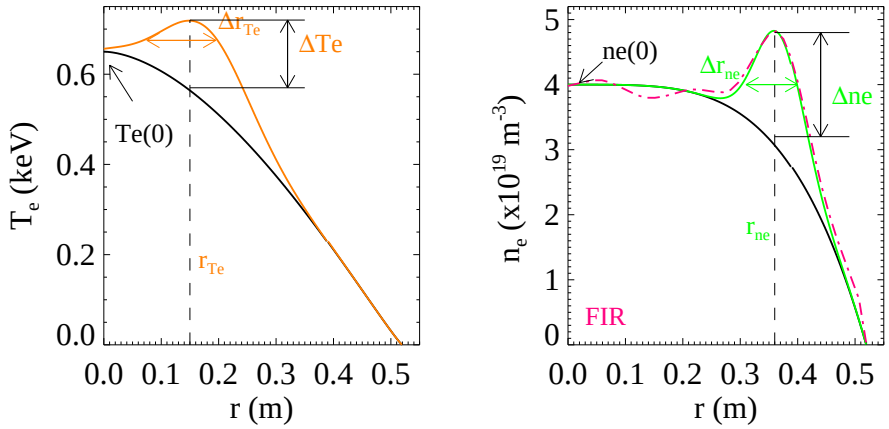

Figure C.2: *(a) Temperature radial profiles implemented in the SXR model, both for a symmetric emissivity distribution (black line) and with a localized thermal structure (orange line). The T_e parameters used in model are reported too. (b) Experimental density profile from FIR data (dashed pink line) and simulations with (green line) and without (black line) a symmetric circular structure, for a pellet-injected plasma in the MST device (#1060523021, $t = 18.0ms$).*

function with $\Delta\theta_{Te}$ is implemented. Sometimes, experimental temperature profiles can be given by the Thomson scattering (TS) diagnostic, and the T_e implemented into the modeled is obtained by fitting the experimental measurements.

In MST plasmas, however, this SXR emissivity model (symmetric + thermal island) fails to reproduce the experimental SXR brightness because the n_e density (as confirmed by FIR data [88]) is often characterized by a slightly hollow profile at high current PPCD discharges. This features can be further accentuated in pellet-injected plasmas, where the density can assume a marked hollow profile. The possibility to take into account these features has been introduced into the model, as a symmetric annular localized density structure added to the symmetric basic profile. This localized symmetric circular n_e increase is radially modeled as a gaussian function, whose height is Δn_e, centered in r_{ne}, and with a radial FWHM of Δr_{ne}. An example of the density profile simulated for a MST high current pellet-injected PPCD plasma with hollow n_e (green line) is illustrated in Fig.C.2(b); the simulated density profile without the structure is displayed with a black line. The computed n_e profile matches very well the experimental data measured with the FIR diagnostic (dashed pink line).

In MST, without the n_e circular structure, the SXR model does not fit the experimental brightness profile at all. Often, it is useful starting from the experimental n_e profiles from FIR data, reproducing them into the model, and then varying and adjusting the temperature profiles in order to reproduce the experimental SXR measurements. In this case, where T_e measurements are available from TS, the

comparison between the T_e simulated and the experimental ones are in good agreement. Similarly, it is possible to start from experimental T_e measurements, and varying the density profile into the model the SXR experimental signals are well reproduced. In this case, the n_e profile computed is in good agreement with the experimental one from FIR.

Bibliography

[1] B. H. Kevles, *Naked to the Bone*, Rutgers Univ. Press, New Brunswick, NY, 1997.

[2] M. Friedman and G. W. Friedland, *Medicine's 10 Greatest Discoveries*, Yale Univ. Press, New Haven, CT, 1998.

[3] Wyndham E.B. Lloyd, *A 100 Years of Medicine*, Gerald Ducworth & Co. Ltd., London, England, 1968.

[4] S. J. Reiser, *Medicine and the Reign of Technology*, Cambridge Univ. Press, Cambridge, MA, 1978.

[5] A. M. Cormack, J. Appl. Phys. **34**, 2722 (1963).

[6] A. M. Cormack, J. Appl. Phys. **35**, 2908 (1964).

[7] A. M. Cormack, Nobel Lecture (8th December 1979).

[8] A. M. Cormack and B. J. Doyle, Phys. Med. Iol. **22**, 994 (1977).

[9] A. L. Boyer, M. Goitein, A. J. Lomax, and E. S. Pedroni, Physics Today **55**, 35 (September 2002).

[10] A. L. Boyer, Physics Today **55**, 38 (September 2002).

[11] G. N. Hounsfield, Nobel Lecture (8th December, 1979).

[12] P. C. Sabatier, *Basic Method of Tomography and Inverse Problems*, Adam Hilger, Bristol, 1987.

[13] R. J. Goldston and P. H. Rutherford, *Introduction to Plasma Physics*, IOP, London, 1995.

[14] I. H. Hutchinson, *Principles of Plasma Diagnostics*, Cambridge Univ. Press, Cambridge, 1987.

[15] S. von Goeler, W. Stodiek, and N. Sauthoff, Phys. Rev. Lett. **33**, 1201 (1974).

[16] M. A. Dubois, D. A. Marty, and A. Pochelon, Nucl. Fusion **20**, 1355 (1980).

[17] N. R. Sauthoff, K. M. McGuire, and S. von Goeler, Rev. Sci. Instrum. **57**, 2139 (1986).

[18] P. Smeulders, Nucl. Fusion **23**, 529 (1983).

[19] Y. Nagayama, S. Tsuji, K. Kawahata, N. Noda, and S. Tanahashi, Jpn. J. Appl. Phys. **20**, L779 (1981).

[20] J. F. Camacho and R. S. Granetz, Bull. Am. Phys. Soc. **29**, 1224 (1984).

[21] P. Smeulders, *A Fast Plasma Tomography Routine with Second-Order Accuracy and Compensation for Spatial Resolution*, Technical Report IPP2252, Max-Planck-Insitut fur Plasmaphysik, Garching, 1983.

[22] R. S. Granetz, *X-ray Tomography in Fusion Research - Diagnostic for Contemporary Fusion Experiments*, P.E. Stott, D.D. Akulina, G. Gorini and E.Sindoni (Eds.), SIF, Bologna, 1991.

[23] R. S. Granetz and J. F. Camacho, *Soft-X ray Tomography on Alcator C*, Plasma Fusion Centre, Massachusetts Institute of Technology, Cambridge, MA 02139, 1985.

[24] P. Franz, L. Marrelli, A. Murari, G. Spizzo, and P. Martin, Nucl. Fusion **41**, 695 (2001).

[25] Y. Nagayama, J. Appl. Phys. **62**, 2702 (1987).

[26] ITER Physics Expert Groups, ITER Physics Expert Group Chairs and Co-Chairs, and TER Joint Central Team and Physics Integration Unit, Nucl. Fusion **39**, 2137 (1999).

[27] D. J. Campbell, Phys. Plasmas **8**, 2041 (2001).

[28] K. Miyamoto, *Plasma physics for nuclear fusion*, MIT press, Cambridge, MA, 1989.

[29] J. D. Lawson, Proc. Phys. Soc. **B70**, 6 (1957).

[30] J. P. Freidberg, *Ideal Magnetohydrodynamics*, Plenum Press, New York, 1987.

[31] T.J.M. Boyd and J.J. Sanderson, *The physics of plasmas*, Cambridge University Press, 2003.

[32] G. Bateman, *MHD instabilities*, MIT Press, Cambridge, MA, 1978.

[33] S. Ortolani and D. D. Schnack, *Magnetohydrodynamics of Plasma Relaxation*, World Scientific, Singapore, 1993.

[34] S. Cappello, F. D'Angelo, D. F. Escande, R. Paccagnella, and D. Bénisti, *Single and multiple helicity states in the Reversed Field Pinch*, volume 23J, page 981, Maastricht, the Netherlands, 1999, 26th EPS Conf. on Contr. Fusion and Plasma Physics, ECA.

[35] B. B. Kadomtsev, *Tokamak plasma: a complex physical system*, Institute of Physics Pub., Bristol, UK, 1992.

[36] D. Biskamp, *Nonlinear magnetohydrodynamics*, Cambridge University Press, Cambridge, UK, 1993.

[37] E. J. Caramana and D. A. Baker, Nucl. Fusion **24**, 423 (1984).

[38] Y. B. Zeldovich, *Magnetic fields in astrophysics*, Gordon & Breach, New York, 1983.

[39] D. Bonfiglio, S. Cappello, and D. F. Escande, Phys. Rev. Lett. **94**, 145001 (2005).

[40] P. Martin et al., Nucl. Fusion **43**, 1855 (2003).

[41] S. Cappello and D. Biskamp, Nucl. Fusion **36**, 571 (1996).

[42] P. Franz et al., Phys. Rev. Lett. **92**, 125001 (2004).

[43] I. Predebon, L. Marrelli, R. B. White, and P. Martin, Phys. Rev. Lett. **93**, 145001 (2004).

[44] R. B. White and M. S. Chance, Phys. Fluids **27**, 2455 (1984).

[45] T. Tamano et al., Phys. Rev. Lett. **59**, 1444 (1987).

[46] G. Rostagni, Fusion Engineering and Design **25**, 301 (1995).

[47] P. Sonato et al., Fusion Engineering and Design **66**, 161 (2003).

[48] L. Marrelli et al., *Experiments of active control of internal resistive MHD modes in RFX-mod*, in *33rd EPS Conference on Plasma Phys.*, pages P–5.092, Rome, 2006, ECA Vol.30I.

[49] S. Martini et al., *High current RFPs in RFX-mod with induced Locked Mode rotation*, in *34th EPS Conference on Plasma Phys.*, pages P–5.134, Warsaw, 2007, ECA Vol.31F.

[50] P. Zanca, L. Marrelli, G. Manduchi, and G. Marchiori, Nucl. Fusion **47**, 1425 (2007).

[51] L. Marrelli et al., Plasma Phys. Contr. Fusion **49**, B359 (2007).

[52] J. S. Sarff, S. A. Hokin, H. Ji, S. C. Prager, and C. R. Sovinec, Phys. Rev. Lett. **72**, 3670 (1994).

[53] B. E. Chapman et al., Phys. Plasmas **9**, 2061 (2002).

[54] R. Bartiromo et al., Phys. Rev. Lett **82**, 1462 (1999).

[55] T. Bolzonella et al., Phys. Rev. Lett. **87**, 195001 (2001).

[56] D. Terranova et al., Phys. Rev. Lett. **99**, 95001 (2007).

[57] P. Zanca, Plasma Phys. Contr. Fusion **49**, 113 (2007).

[58] R. Dexter, D. Kerst, T. Lovell, S. Prager, and J. Sprott, Fusion Technol. **19**, 131 (1991).

[59] T. P. Donaldson, Plasma Physics **20**, 1279 (1978).

[60] R. S. Granetz and P. Smeulders, Nucl. Fusion **28**, 457 (1988).

[61] J. R. L. Branham, *Scientific Data Analysis of Integral Equations,* Claredon Press, Oxford, 1984.

[62] P. Martin et al., Rev. Sci. Instrum. **68**, 1256 (1997).

[63] P. Franz et al., Rev. Sci.Instrum. **75**, 4013 (2004).

[64] J. Kiraly, Nucl. Fusion **27**, 397 (1987).

[65] P. Martin, A. Murari, and L. Marrelli, Plasma Phys. Contr. Fusion **38**, 1023 (1996).

[66] A. Murari et al., Rev. Sci. Instrum. **70**, 581 (1999).

[67] L. Carraro et al., Nucl. Fusion **36**, 1623 (1996).

[68] F. Bonomo et al., Rev. Sci. Instrum. **77**, 10F313 (2006).

[69] P. Franz et al., Phys. Plasmas **13**, 012510 (2006).

[70] P. Martin et al., Plasma Phys. Control. Fusion **49**, A177 (2007).

[71] D. F. Escande et al., Phys. Rev. Lett. **85**, 1662 (2000).

[72] R. Paccagnella et al., Phys. Rev. Lett. **97**, 75001 (2006).

[73] L. Marrelli et al., Phys. Plasmas **9**, 2868 (2002).

[74] A. Alfier and R. Pasqualotto, Rev. Sci. Instrum. **78**, 013505 (2007).

[75] A. Alfier, *Electron temperature measurements by Thomson scattering in plasma fusion devices*, PhD thesis, Universitá degli Studi di Padova, Italy, 2006.

[76] M. Gobbin, L. Marrelli, P. Martin, , and R. B. White, Phys. Plasmas **14**, 072305 (2007).

[77] D. F. Escande, R. Paccagnella, S. Cappello, F. D'Angelo, and C. Marchetto, PHys. Rev. Lett. **85**, 3169 (2000).

[78] P. Franz et al., Europhys. Lett. **59**, 48 (2002).

[79] S. V. Annibaldi et al., Phys. Plasmas **14**, 112515 (2007).

[80] F. Porcelli, E. Rossi, G. Cima, and A. Wootton, Phys. Rev. Lett. **82**, 1458 (1999).

[81] S. V. Annibaldi, P. Buratti, E. Giovannozzi, D. Frigione, and F. Porcelli, Nucl. Fusion **44**, 12 (2004).

[82] A. Intravaia et al., Phys. Rev. Lett. **83**, 5499 (1999).

[83] A. Alfier et al., *Electron temperature measurements and heat transport improvement in the RFX-mod experiment*, Orlando, Florida, November 12-16, 2007, 49th Annual Meeting of the Division of Plasma Physics.

[84] P. Buratti et al., Plasma Phys. Control. Fusion **39**, B383 (1997).

[85] D. Terranova et al., *Enhanced confinement, magnetic topology and diffusion in RFX-mod for poloidal current drive*, Orlando, Florida, November 12-16, 2007, 49th Annual Meeting of the Division of Plasma Physics.

[86] J. K. Anderson, *Measurement of the Electrical Resistivity Profile in the Madison Symmetric Torus*, PhD thesis, University of Wisconsin (Madison), WI, 2001.

[87] R. L. Kelly and L. J. Palumbo, *Atomic and Ionic Emission Lines Below 2000 Angstrom - Hydrogen Through Krypton*, Naval Research Laboratories, Washington, D.C., 1973.

[88] B. H. Deng et al., Rev. Sci. Instrum. **77**, 10F108 (2006).

[89] P. Franz et al., Rev. Sci. Instrum. **77**, 10F318 (2006).

[90] B. E. Chapman et al., *Generation and confinement of hot ions and electrons in MST*, Orlando, Florida, November 12-16, 2007, 49th Annual Meeting of the Division of Plasma Physics.

[91] B. E. Chapman, *Improved confinement MST RFP plasmas with hot ions and high density*, Philadelphia, Pennsylvania, October 30-November 3, 2006, 48th Annual Meeting of the Division of Plasma Physics.

[92] D. Craig, D. J. Den Hartog, D. A. Ennis, S. Gangadhara, and D. Holly, Rev. Sci. Instrum. **78**, 013103 (2007).

[93] D. J. Den Hartog et al., Rev. Sci. Instrum. **77**, 10F122 (2006).

[94] S. Gangadhara, D. Craig, D. A. Ennis, and D. J. Den Hartog, Rev. Sci. Instrum. **77**, 10F109 (2006).

[95] M. Wyman et al., submitted to Phys. Plasmas .

[96] H. Cummings, J. A. Reusch, R. O'Connell, and D. J. Den Hartog, Bull. Am. Phys. Soc. **50**, 37 (2005).

[97] F. Bonomo et al., Phys. Plasmas **12**, 093301 (2005).

[98] W. H. Press, B. P. Flannery, S. A. Teukolsky, and W. T. Wetterlig, Cambridge University Press, first edition, Cambridge, MA, 1987.

[99] S. Gull and G. Danniel, Nature **272**, 686 (1978).

[100] L. Wang and R. Granetz, Rev. Sci. Instrum. **62**, 842 (1991).

[101] L. Wang and R. Granetz, Rev. Sci. Instrum. **62**, 1115 (1991).

[102] G. N. Watson, *A Treatise on the Theory of Bessel Functions*, Cambridge Mathematical Library, second edition, 1958.

[103] C. DeMichelis and M. Mattioli, Nucl. Fusion **21**, 677 (1981).

Acknowledgments

This thesis is much more than what you can find in the previous pages! It corresponds to three wonderful years of my life, during which I grew up, I matured, I become adult. But I have never been alone: a lot of people - friends and colleagues - surrounded me, helped and encouraged me in my walk of life. For these reasons, I would like to thanks the most important ones.

As concern my work at RFX, I would like to thanks my colleague PF, who taught me the competencies I acquired in these years and all the “SXR secrets”. We spent a lot of time with wires and screwdrivers, but also with IDL and my famous “NON funzionaaaa...!!!”. Sometimes I had to hide the hammer...but we also laughed and amused!
Thanks also to Gianluca, the big-little bear, for our long discussions, not always on physics matters....but interesting and formative all the same! Obviously, thanks also to the great amount of chocolate and sweets that PF and Gianluca shared with me...
I would like to thanks also Lionello Marrelli for the numerous and prolific discussions on physics matter, and for his kindness and availability during the realization of this thesis.

A huge thanks to my parents, always present and supporting all my choices. They have been a fundamental support in difficulties, but especially wonderful friends to laugh with in the happiest moments. Thanks for helping me during these three years, but also in all my life, for guiding me when I seemed to have lost the motivations and for letting me living my life without interferences: what I am is all your great worthiness, thanks!!

A special thanks to my sister Michela, the person I laughed with and I cried on during all these months: she has been an unreplaceable friend, a wonderful sister,

a wise guide in all my life! A special thought to my little great nephew Mattia, and my sweet niece Greta: they are two memorable sparkling lights in my life!

A great thanks to my Ph.D. co-workers, "living" all together in the same office: day after day we faced the difficulties of working until late in the evening, of encouraging those who were downhearted, of putting up with jitter and sadness. But more frequently we faced joyful weeks, coffee break and travels: these are the moments I dearly keep in my heart! Fulbiattolo, the small mole, always present to listen, advise and support. The "speedy-foot" Gobbino, beating the time of our thesis writing. Magostini, the sweet-glance fawn. Takkon: an always frontline E.R.! Ritu, with her "hyperactive" sense of life, thinking, living...and speaking! ...thanks to all of you!!

At last, but not at least, a whole-hearted thanks to my great love and best friend, Luca. We met during the Ph.D. course: inch by inch, day by day, we grew up and faced zillion of wonderful moments, sometimes on different continents...but always together!

Luca, for all these reasons, I would like to dedicate this thesis to you....
...and for this and much more than this, thanks!!

Ringraziamenti

Questa tesi é molto piú di quanto viene descritto nelle pagine prcedenti! Sono stati tre meravigliosi anni della mia vita, durante i quali sono cresciuta, maturata e diventata adulta. Ma non sono mai stata da sola: numerose persone - amici e colleghi - mi hanno accompagnato e mi sono stati vicini, mi hanno aiutato e incoraggiata in questo mio percorso di vita. Per queste ragioni vorrei ringraziare le piú importanti.

Per quanto riguarda l'ambito lavorativo, vorrei ringraziare il mio collega PF, che mi ha insegnato tutte le competenze che ho acquisito in questi tre anni, nonché tutti i segreti sugli SXR. Abbiamo trascorso insieme molto tempo con cavi e cacciaviti, ma anche con IDL e il mio famoso "NON funzionaaaa...!!!". A volte ho dovuto nascondergli il martello...ma abbiamo anche riso e ci siamo divertiti!
Un ringraziamento anche a Gianluca, il grande "orsetto", per le nostre lunghe discussioni, non sempre di fisica...ma molto interessanti e formative! Ovviamente un ringraziamento a PF e Gianluca anche per la quantitá industriale di dolcetti e cioccolata che ci siamo sbaffati in tutti questi anni...
Vorrei inoltre ringraziare anche Lionello Marrelli per le numerose e proficue discussioni in ambito di fisica, nonché per la disponibilitá dimostrata durante la stesura e la correzione di questa tesi.

Un ringraziamento speciale ai miei genitori, sempre presenti, che mi hanno supportato in tutte le scelte di questi anni. Sono stati un fondamentale punto di appoggio nelle difficoltá, ma soprattutto degli amici fantastici con cui ridere nei momenti piú sereni e allegri. Grazie per avermi aiutato durante questi tre anni, ma anche nel corso di tutta la mia vita, per avermi guidato quando credevo di aver perso le motivazioni, ma nello stesso tempo per avermi lasciato fare le mie scelte senza interferire troppo: quello che sono lo devo esclusivamente a voi, grazie!!

Un ringraziamento di cuore a mia sorella Michela, la persona con cui ho piú riso e pianto durante questi mesi: é stata un'amica insostituibile, una sorella meravigliosa, una saggia guida in tutta la mia vita! Un pensiero speciale anche ai miei due nipotini, le mie due "piccole pesti", il tenero e sensibile Mattia e la piccola dolce Greta: sono due splendide luci che brillano nella mia vita!!

Un enorme grazie anche ai miei colleghi di dottorato, con cui ho "vissuto" nello stesso ufficio in questi tre anni: giorno dopo giorno abbiamo affrontato le difficoltá di lavorare fino a tardi la sera, di incoraggiarci nel bisogno, di sopportare nervosismi e tristezze. Ma piú frequentemente abbiamo condiviso settimane gioiose e allegre, pause caffé indimenticabili e numerosi viaggi: questi saranno i momenti che custodiró nel cuore! Fulbiattolo, la piccola *talpa*, sempre presente ad ascoltare, consigliare e supportare. Il "pié-veloce" Gobbino, che ha scandito il tempo durante la scrittura della tesi. Magostini, il cerbiatto dal dolce sguardo. Takkon: un E.R., sempre in prima linea! Ritu, con il suo senso "iperattivo" della vita, di pensare, di vivere e di...parlare! ...grazie a tutti voi!!

Infine, un ringraziamento di tutto cuore al mio grande amore e miglior amico Luca. Ci siamo incontrati durante il corso di dottorato: a poco a poco, giorno dopo giorno, siamo cresciuti e abbiamo condiviso un'infinitá di momenti splendidi, anche se a volte su continenti diversi...ma pur sempre insieme!

Luca, per queste ragioni vorrei dedicarti questa tesi...
...e per tutto questo, e molto altro ancora, grazie!!